Department of Precision and Microsystems Engineering

Multi-material Topology Optimization for Passive Vibration Isolators – Analysis & idation

Alessandro Urbani

Report no	: 2026.090
Coach	: Arnoud Delissen
Professor	: Jieun Yang
Specialisation	: Computational Design and Mechanics (CDM)
Type of report	: MSc Thesis
Date	: 8th of September 2026

TU Delft Delft University of Technology

Challenge the future

Multi-material Topology Optimization for Passive Vibration Isolators – Analysis & Validation

Msc Thesis

Alessandro Urbani

Delft University of Technology



TU Delft

TNO innovation for life

Multi-material Topology Optimization for Passive Vibration Isolators – Analysis & Validation

Msc Thesis

by

Alessandro Urbani

Student ID

6193900

TNO Supervisor:	Dr. ir. Arnoud Delissen
TU Delft Supervisor:	Dr. Jieun Yang
Faculty:	Faculty of Mechanical Engineering, Delft

Cover:	Canadarm 2 Robotic Arm Grapples SpaceX Dragon by NASA under CC BY-NC 2.0 (Modified)
Style:	TU Delft Report Style, with modifications by Daan Zwaneveld

TU Delft

Contents

Abstract **1**

1 Introduction **2**
1.1 Scope and assumptions . . . 7
1.2 Thesis structure . . . 7

2 Dynamical system modeling **9**
2.1 Viscoelastic material model . . . 9
2.2 3-degree-of-freedom system formulation . . . 12
2.2.1 Stiffness matrix . . . 13
2.2.2 Mass matrix . . . 15
2.3 Non-linear eigenvalue problem . . . 16
2.4 Frequency response analysis . . . 18
2.5 Stress calculations . . . 20

3 Topology optimization **23**
3.1 Multi-material topology optimization formulation . . . 23
3.2 Stress constraint . . . 25

4 Experimental method **27**
4.1 Case study design . . . 27
4.1.1 3D model design . . . 28
4.2 Multi-material additive manufacturing . . . 29
4.2.1 Interface bonding . . . 30
4.3 Testing procedure . . . 30
4.3.1 Signal processing and model identification . . . 32

5 Results **34**
5.1 Base case . . . 34
5.2 Optimized designs . . . 38
5.2.1 x-mode damping . . . 39
5.2.2 y-mode damping . . . 41
5.2.3 Multi-mode damping . . . 42
5.3 Further exploration of numerical results . . . 44
5.3.1 Influence of frequency-dependent material properties . . . 44
5.3.2 Influence of material selection . . . 46
5.3.3 Upper eigenfrequency constraint . . . 48
5.3.4 Stress evaluation . . . 49

6 Discussion **50**
6.1 Experimental validation and sources of mismatch . . . 50
6.2 Stress constraints and comparison . . . 53
6.3 Manufacturing and practical feasibility . . . 53

7 Conclusions **55**
7.1 Contributions . . . 55
7.2 Findings . . . 55
7.3 Recommendations and future work . . . 56

References **57**

A Mathematical Derivations **60**
A.1 Reduced stiffness matrix derivation . . . 60

A.2 Reduced payload mass matrix derivation . . . 60
A.3 Eigenmodes sorting . . . 61
A.4 Rigid-body transformation to the sensor position . . . 61
A.5 Peak von Mises stress for complex harmonic stresses . . . 62
A.6 Stress field comparison . . . 64
A.7 Strain simulation example . . . 64

B Additional modal deformation of isolator designs **65**
B.1 x-mode damping (alternative materials) . . . 65
B.2 y-mode damping (alternative materials) . . . 66
B.3 Multi-mode damping (alternative materials) . . . 66

C Arduino setup **67**

D Additional plots **72**
D.1 Base case . . . 73
D.2 x-mode damping . . . 76
D.3 y-mode damping . . . 79
D.4 Multi-mode damping . . . 82

E Usage of AI **85**

Abstract

Vibration isolators reduce the transmission of unwanted disturbances to a sensitive payload, thereby protecting mounted instruments and enhancing their operational accuracy. This thesis focuses on improving and validating experimentally a topology optimization framework that aims to design passive vibration isolators using both structurally stiff and viscoelastic materials. The framework models the in-plane system dynamics in three degrees of freedom while accounting for frequency-dependent material properties and stress constraints. The objective is to optimize damping either for individual rigid-body modes or for all modes simultaneously.

The designs are then converted into 3D models, manufactured using multi-material additive manufacturing, and validated through finite-element simulations and experimental shaker testing. The framework shows strong agreement with 2D finite-element models, accurately predicting primary rigid-body modes and damping characteristics. Experimental results confirm the intended dynamic behavior of the optimized designs, although discrepancies in resonance frequencies and damping remain.

Overall, this research demonstrates the potential of multi-material topology optimization for the creation of customized passive vibration isolators, while identifying key modeling and manufacturing refinements required for practical application.

1

Introduction

Modern spacecraft increasingly rely on sensitive payloads, including optical terminals, precision pointing systems and cryogenic detectors. The performance of this equipment depends not only on their own measurement accuracy, but also on the mechanical environment created by the spacecraft and launch vehicle. During launch, high dynamic loads originate from acoustic excitation, engine operation, stage separation and shock events. Once in orbit, vibrations continue to be generated by reaction wheels, control moment gyroscopes, cryocoolers, thrusters and other moving subsystems (Dennehy and Alvarez-Salazar 2018). Because these components are essential for spacecraft operations, their vibration output cannot simply be eliminated at the source, so other means of vibration mitigation are required.

To address this challenge, vibration isolators help to reduce the transmission of motion between a disturbance source and a sensitive payload when placed between them. They improve dynamic stability and ensure high-precision to the payload by attenuating motion within specific frequency ranges.

The performance of these isolators is typically evaluated using a transmissibility curve, as shown in Figure 1.1, which highlights a fundamental design trade-off. At the system's natural frequency, vibrations are sharply amplified, making structural damping necessary to suppress the peak. However, at higher frequencies, the system enters the isolation zone where the mount acts as a protective filter. In this region, excessive damping becomes detrimental, as it degrades isolation efficiency and allows more jitter to reach the payload.

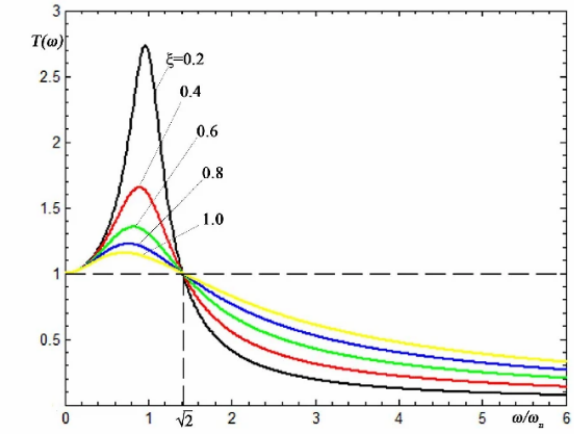


Figure 1.1: Transmissibility curve (Image adapted from Zou et al. (2014)).

Active and semi-active isolators (Karnopp 1995) can adapt their response using sensors, actuators and control logic, which makes them attractive for better damping performances over a broad range of

frequency. However, this adaptability comes at the cost of additional electronics components, mass, control complexity and potential failure modes. On the other hand, passive isolators remain attractive for spacecraft because they operate without external power, they are mechanically simple, and can provide predictable and robust behaviour over long missions (Shi et al. 2024). Their main limitation is that the achievable isolation bandwidth is fixed by the chosen geometry and material properties. In particular, it is difficult to combine heavy load support, low frequency isolation, and multi-directional performance in a single design.

Viscoelastic materials provide an important passive damping mechanism because they combine elastic energy storage with internal energy dissipation. Under cyclic deformation, part of the mechanical energy is converted into heat through molecular friction and delayed stress-strain response (Tanaka and Eijden 2003). In practical damping treatments, the viscoelastic material is arranged in a soft layer so that structural vibration produces significant shear deformation. This principle is used in free-layer and constrained-layer damping treatments (Figure 1.2), where a polymer or rubber layer is bonded to a stiffer structure and forced to deform by shearing (Moreira 2014).

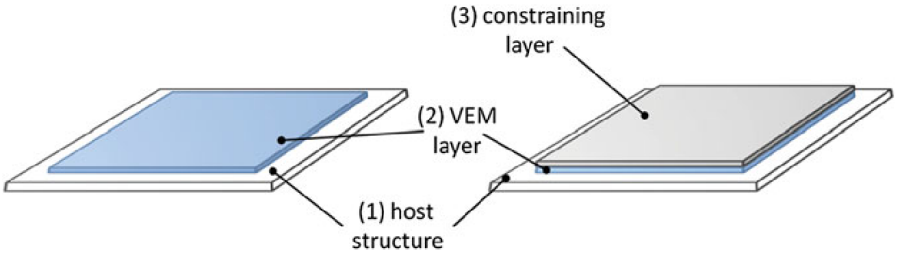


Figure 1.2: The 2 configurations for VE passive damping treatment: **a** Free layer damping , **b** Constrained layer damping (CLD) (Image adapted from Moreira (2014))

We can find various space-related projects that have implemented constrained-layer damping in their designs, such as the Small-CAT (Small Communication Active Terminal) laser communication system engineered by TNO (Doelman et al. 2026), visible in Figure 1.3. The lateral oblique supports were created purposely to prevent transmission of vibration along the axial direction. A rubber layer is injection moulded between an inner and outer shell, increasing the shear deformation and energy dissipation in the rubber. Another example is provided by the damped struts of the James Webb Space Telescope (JWST) that isolate the base of the telescope (Figure 1.5). They help reduce vibrations coming from the compressor and the six reaction wheels (Menzel et al. 2023). At a larger structural scale, the Omniflex isolator (Johal, Christensen, and Doud 2012) helps to attenuate dynamic loads for launch vehicles coming to the top payload. Compliant members carry the load while rubber layers dissipate vibrational energy in three translational directions, the single structure is visible in Figure 1.4.

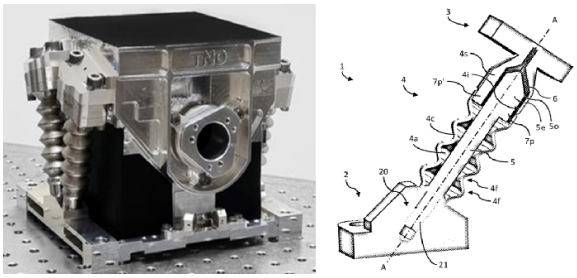


Figure 1.3: TNO smallCAT (Image adapted from Doelman et al. (2026) and Kempen, Vreugd, and Crowcombe (2023))



Figure 1.4: Omniflex isolator (Image adapted from Johal, Christensen, and Doud (2012))

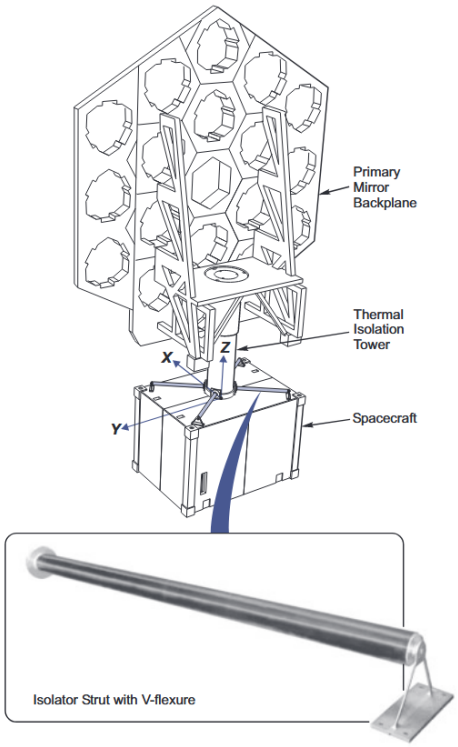


Figure 1.5: James Webb Space Telescope scheme (Image adapted from Menzel et al. (2023))

Although these concepts are well established, conventional passive isolators are usually based on predefined structural layouts. Engineers choose the number, orientation and shape of struts, flexures or damping layers before tuning their dimensions and material properties. This approach is effective when the expected load path is simple, but it restricts the design space. For compact isolators, the best distribution of stiff and dissipative material is not necessarily obvious. Because of the severe environment, for example to handle the high forces and vibrations experienced during launch, it becomes a priority to design the isolator stiff enough so that the natural frequency of the system stays above a certain threshold (Space Exploration Technologies Corp. 2022). The core challenge lies in maintaining this stiffness while providing sufficient damping through soft viscoelastic materials within the structural domain, achieving a balanced trade-off.

Topology optimization offers a systematic way to address this problem. Instead of optimizing only a small number of geometric parameters, it distributes material throughout a prescribed design domain according to a selected objective, constraints, boundary conditions and governing physics. In dynamic structural problems, topology optimization has been used to tailor natural frequencies, frequency response, dynamic compliance and modal damping (Du and Olhoff 2007; Niu et al. 2018; Q. Liu, Ruan, and Huang 2018). A multi-material formulation further expands the design freedom by allowing the optimizer to choose where a stiff structural phase should carry load and where a viscoelastic phase should dissipate energy. In this regard, Kolk et al. (2017) use parametric level-set functions to distinguish with sharp separated regions three material phases: hyperelastic, viscoelastic and void (example visible in Figure 1.6). In this case the objective is to maximize the loss factor, which is linked to energy dissipation, while having a constraint on the volume for each phase and a lower bound for the first fundamental eigenfrequency. Alternatively, G. Zhang and Khandelwal (2019) opt for a density-based framework to analyze the same general problem. It uses the SIMP (Solid Isotropic Material with Penalization) interpolation to make the element densities inside the domain converge into a discrete design (example visible in Figure 1.7). This approach produces less sharply defined boundaries in the final design.

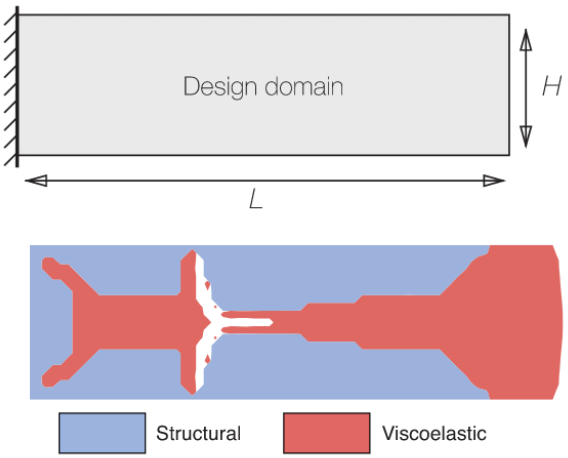


Figure 1.6: Initial domain (top) and result of TO implementation (bottom) (Image adapted from Kolk et al. (2017))

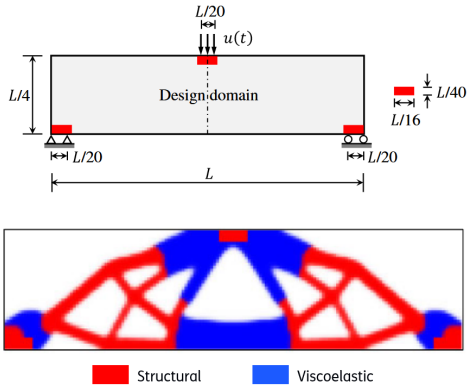


Figure 1.7: Initial domain (top) and result of TO implementation (bottom) (Image adapted from G. Zhang and Khandelwal (2019))

The framework created most recently by Petrulis (2025) also utilizes a density-based approach to formulate a two-material topology optimization involving purely elastic and viscoelastic phases. The dynamic response of the isolator-payload system is modeled via a modal approach, which considers only in-plane rigid body motions (horizontal/vertical translations and rotation), assuming there are no internal flexible modes. This approach enables the analytical formulation of damped resonances across the 2D optimized domain, by calculating the system's eigenmodes and associated quality factor (Q-factor) in the frequency domain. In this case the objective is the maximization of the eigenfrequencies, while maintaining the quality factor below a prescribed value. An example of optimized design can be seen in Figure 1.8.

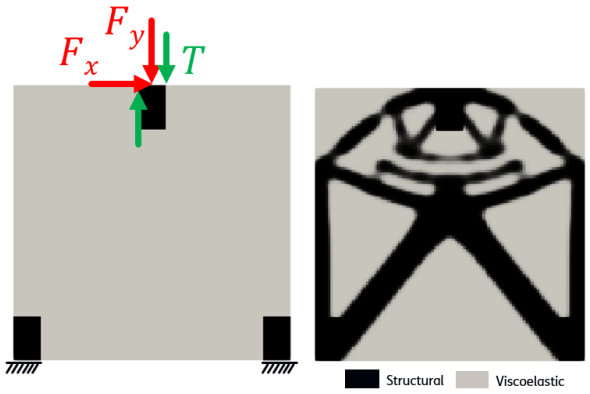


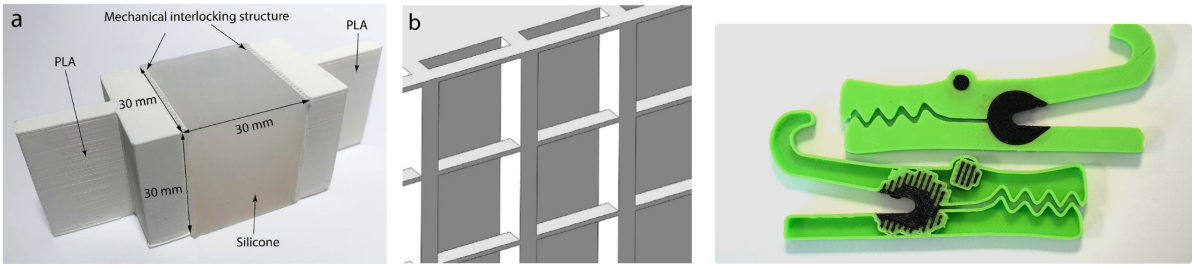
Figure 1.8: Initial domain and boundary conditions (left) and topology optimized design for x-direction (right) (Image adapted from Petrulis (2025))

The use of viscoelastic materials inside topology optimization, however, introduces an additional modeling challenge. Their stiffness and damping are not constant material properties, instead they are highly sensitive to temperature and frequency (Jauregui 2019). By including frequency dependent material properties, the eigenvalue problem solved to find the main resonances is no longer purely linear. Research has been done to find methods to implement frequency and temperature dependence for viscoelastic materials inside the topology optimization algorithm. Notably, D. Zhang et al. (2022) implement an iterative modal analysis procedure within the topology optimization loop to account for the frequency and temperature dependent behavior of the viscoelastic core in constrained layer damped structures. Their formulation is conceptually similar to that of Kolk et al. (2017): both employ a para-

metric level-set method and optimize damping performance by maximizing a modal loss factor. However, no study was found that incorporates this dependence while simultaneously allowing two material phases (hyperelastic and viscoelastic) to be freely distributed throughout the design domain. Accounting for this behaviour is necessary to obtain dynamically consistent predictions, since the stiffness and damping of the viscoelastic phase depend on the frequencies of the resulting modes.

Nonetheless, numerical optimization alone is not sufficient to establish whether these designs are practically effective. The optimized layout must also be manufacturable, also its predicted eigenfrequencies and damping properties must be reproducible in the physical prototype.

Experimental analysis is therefore an essential part of the work. Dynamic Mechanical Analysis (DMA) is used to characterize the viscoelastic material response and provide the relevant frequency dependent material properties needed for the numerical model (Struz et al. 2024; Elkhoury et al. 2025). For prototype creation, additive manufacturing facilitates the creation of complex shapes that result from the optimization. However, particular attention must be paid to the interfaces between rigid and viscoelastic phases as surface adhesion needs to be ensured. Most commonly, solvents and special glues are used to help with bonding, whereas a non-chemical alternative relies on the implementation of interlocking features. Figures 1.9a and 1.9b illustrate two different use cases where custom features help to maintain a tighter connection between the materials.



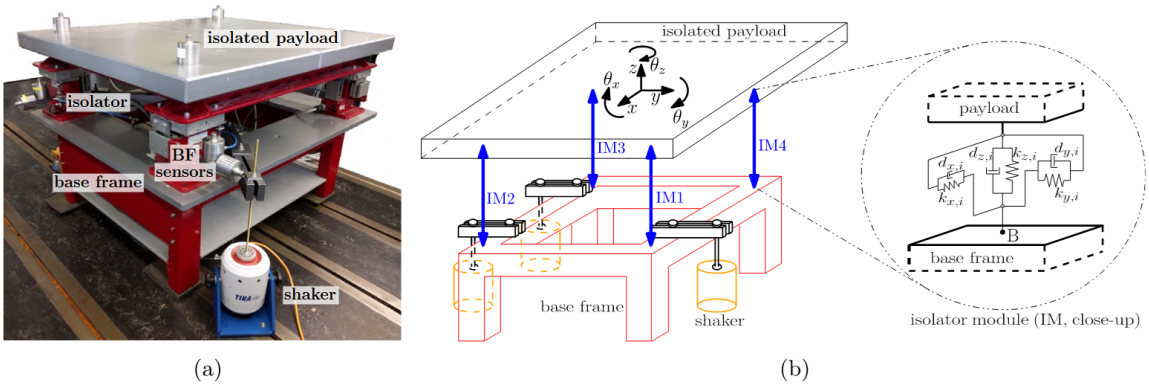
(a) Test sample and a zoom on the interlocking cells at the interfaces between PLA and silicone (Image adapted from Rossing et al. (2020))

(b) Clip with surface enhancing structure automatically generated at the interfaces (Image adapted from UltiMaker (2023))

Figure 1.9: Examples of interlocking features for multi-material interfaces.

The final step is to evaluate the actual dynamic performance of the optimized structure through experimental validation. S.-Y. Kim, Mechefske, and I. Y. Kim (2013) demonstrated this for a topology optimized damping layout applied to a shell structure, comparing the frequency response obtained through both numerical simulation and experimental testing. Such validations remain limited to layered damping shell structures. For structures in which the stiff and viscoelastic phases are freely distributed throughout the structural domain, no evidence was found on how the predicted modal damping and transmissibility compare to real test results. Moreover, the majority of available work using topology optimization remains numerical, and only limited attention has been given to the complete validation required for a functional isolator.

More generally for multi-axis vibration-isolation systems, Beijen et al. (2018) developed an identification method in which the motions of the base frame and payload are measured under shaker excitation (Figure 1.10) to estimate the complete transmissibility matrix of the system. These experimental approaches help establish whether the predicted damping and isolation performance is achieved in practice, revealing any discrepancies between the analytical model and the final manufactured design.



(a) (b)

Figure 1.10: (a) Test setup of the industrial active vibration system; **(b)** schematic representation showing the different parts (Image adapted from Beijen et al. (2018))

The project will focus on extending the novel topology optimization framework already carried out by Petrulis (2025) to achieve feasible and manufacturable structures. Frequency dependent material properties measured through Dynamic Mechanical Analysis are incorporated through a fixed-point iteration method and stress constraints are introduced to improve structural feasibility. Selected 2D designs are then converted into 3D prototypes and produced via additive manufacturing. The designs will then be verified and validated through COMSOL simulations and experimental shaker testing. The objective is not only to obtain optimized layouts numerically, but to assess how well their predicted dynamic performance agrees with the test results under the same prescribed conditions.

1.1. Scope and assumptions

- **Application:** the study considers passive vibration isolators connecting an excited base to a rigid payload. Active and semi-active isolation systems are outside the scope.
- **Structural dynamics:** the system is represented in three degrees of freedom. Out-of-plane motion and internal flexible modes are neglected in the generalized model. Small deformation, linear dynamic behaviour and plane strain are assumed. Finite elements used for simulations are also linear.
- **Geometry:** the studied domain is developed in two dimensions. Selected layouts are extruded into three-dimensional geometries for finite element verification and prototype fabrication.

  It is worth noting that the framework is extendable to full 3D designs. Although, this would require a complete rework of the design domain: mainly the implementation of 3D elements, redefining boundary conditions and adapting the dynamics to 6 degrees of freedom instead of 3. Such an extension inevitably increases the computational cost, which must be accounted for.
- **Temperature:** a constant temperature is assumed in the numerical models and experiments; temperature variations and thermomechanical effects are not considered.
- **Manufacturing:** prototypes are produced using multi-material additive manufacturing. Interlocking interfaces and post-processing operations are introduced manually and are not included in the optimization.

1.2. Thesis structure

Following the introduction, the thesis is structured into six main chapters. Chapter 2 introduces the dynamical model used to describe the whole isolator-payload system. It presents the viscoelastic material formulation, the generalized stiffness and mass matrices utilized in the dynamical system. It then continues with the frequency dependent eigenvalue problem, the transmissibility formulation used for model validation and how stresses are calculated. Building on the modeled framework, Chapter 3 describes the multi-material topology optimization setup. The formulation includes the design variables, objective and constraints, the implementation of frequency dependent viscoelastic properties, and the

inclusion of stress constraints. Chapter 4 describes the experimental validation workflow; it covers the design of the test configuration, multi-material additive manufacturing, interface considerations, the shaker-test setup, data acquisition and signal processing. Chapter 5 applies topology optimization to different objective cases, the layouts and final plots are presented together with additional numerical results. Chapter 6 discusses the numerical and experimental results, with particular attention to the obtained mismatches, modeling uncertainty, manufacturability and possible improvements. Finally, Chapter 7 summarizes the main conclusions and identifies recommendations for future work.

2

Dynamical system modeling

2.1. Viscoelastic material model

Since the damping performance of the isolator is mainly controlled by the viscoelastic phase, the first step is to define a material model that captures both stiffness and energy dissipation in the frequency domain. Elmoghazy et al. (2024) summarize current ways to model the viscoelastic behavior, for example utilizing spring-damper configurations in the case of the Maxwell, Kelvin-Voigt or Zener model. Alternatively, it can be described analytically by its modulus in the complex domain, where the imaginary part represents the dissipative response. The base framework utilizes the latter representation.

The mechanical response is mainly dictated by its stress-strain relationship. Bower (2009) gives a correlation between the strain and stress tensor which separates the volumetric and deviatoric components. The two physical behaviors are captured respectively with the bulk modulus κ and the shear modulus G. The bulk modulus has a smaller contribution to energy dissipation than the shear modulus. This is because elastomers are nearly incompressible and have a Poisson's ratio close to 0.5 (Bower 2009). This means that volumetric deformation is lower compared to shear deformation when the same force is applied, so that it can be considered purely elastic (COMSOL AB 2024a). Therefore, in this work the bulk modulus is simplified and considered real-valued, while the shear modulus is described as follows:

$$G^*(\omega, T) = G'(\omega, T) + iG''(\omega, T) \tag{2.1}$$

where G' is the storage modulus, and G'' is the imaginary part called loss modulus and is responsible for the dissipative behavior, both dependent on frequency ω and temperature T. We can relate storage and loss moduli to the phase angle δ

$$tan(\delta) = \frac{G''(\omega, T)}{G'(\omega, T)} = \eta(\omega, T). \tag{2.2}$$

In this manner we can quantify energy dissipation by looking at the loss factor η.

As indicated in Equations 2.1 and 2.2, the dependence on ω and T is relevant because inside a viscoelastic material the mobility of molecular chains, which control the stiffness as well as damping properties, can significantly depend on the frequency at which the loading is applied, together with temperature (Shu, You, and Zhou 2022). For space applications, a vibration isolation system could be exposed to a very broad temperature range during operation as well as external loads at different frequencies. For example, NASA reports that external ISS hardware without thermal control could experience temperatures ranging approximately from $-150\,^\circ\mathrm{C}$ in full shade to $120\,^\circ\mathrm{C}$ in full sunlight (Davies 2015). Consequently, accounting for these two factors is crucial.

The majority of viscoelastic materials are amorphous polymers (Jauregui 2019) and feature a distinct glass transition temperature T_g. As shown in Figure 2.1, increasing the temperature through this threshold makes the material transition from a rigid region to a high elasticity state, stabilizing into a rubbery plateau characterized by a lower modulus and reduced damping performance. Below T_g, the restricted

molecular mobility results in a high storage modulus G' and low loss factor η. Within the "vitrification transition region" near T_g, the enhanced chain mobility causes a sharp decline in stiffness alongside a peak in the loss factor η, marking the point of maximum energy dissipation (Ferry 1980).

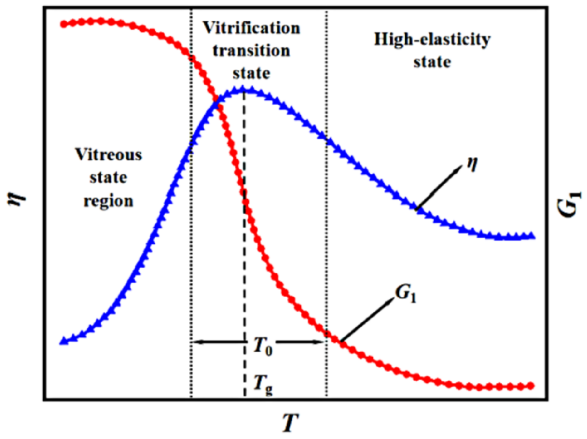


Figure 2.1: Variation curve of parameters G' (elastic shear modulus) and η (loss factor) with temperature (Image adapted from Shu, You, and Zhou 2022).

The effects of frequency can be correlated to temperature through the Time-Temperature Superposition (TTS) principle (Jauregui 2019). It demonstrates how a change in environmental temperature is mathematically equivalent to a proportional shift in the frequency domain. Consequently, the material's mechanical response at high temperatures corresponds directly to its behavior at low frequencies (or long loading times) and vice versa. This principle becomes crucial for predicting material behavior over broad frequency spectra encountered in space applications. In this work, we focus on the frequency dependence of the chosen viscoelastic material while keeping the temperature fixed at a reference value. This choice reflects the testing environment considered in the project, where the isolator is excited over a prescribed frequency range while the laboratory temperature remains approximately constant.

Dynamic Mechanical Analysis (DMA) is performed and isothermal tests at various temperatures are conducted to obtain curves for the storage shear modulus G' and loss shear modulus G''. These isothermal curves are then shifted horizontally along the frequency axis to align with the data at a chosen reference temperature T_r, thus building a single "master curve" where the moduli vary with frequency. A graphical example is visible in Figure 2.2.

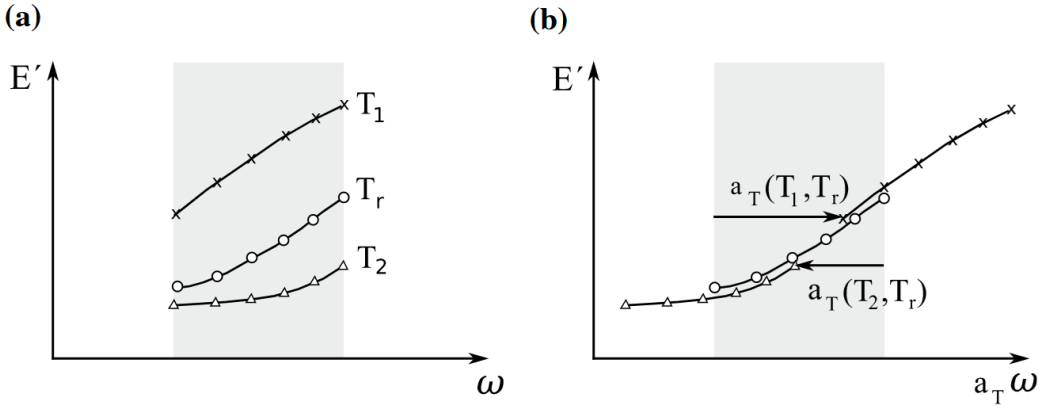


Figure 2.2: Plots representing the time-temperature superposition principle: **(a)** storage modulus curves at temperatures T_1, T_2 and T_r (with $T_1 > T_r > T_2$), **(b)** unique storage modulus curve at reference temperature T_r (Image adapted from Jauregui 2019).

The magnitude of this horizontal shift for each isotherm is defined by a shift factor, a_T. The relationship

between a_T and temperature in this case is modeled using a variation of the Williams-Landel-Ferry equation (K. P. Menard and N. Menard 2020):

$$ln(a_T) = \frac{a(T - T_0)}{b + (T - T_0)} \tag{2.3}$$

where T is the experimental test temperature, T_0 is the chosen reference temperature for the master curve and a, b are empirical constants.

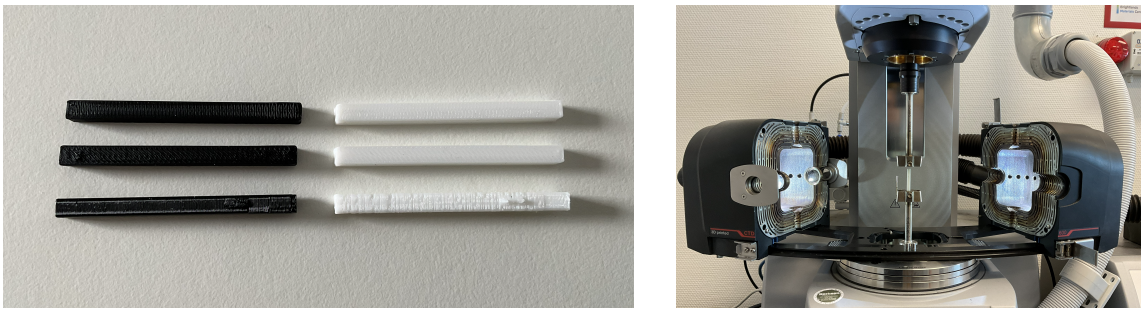
At the TNO Brightlands Materials Center facility, the master curves for PLA and TPU 95A HF from BambuLab were obtained via DMA with a reference temperature of $20°\mathrm{C}$ (Bambu Lab 2026a; Bambu Lab 2026b).

TPU and PLA samples of dimensions $50 \times 4 \times 4\ \mathrm{mm}^3$ were 3D-printed in three different configurations (Figure 2.3a). Torsional testing was performed on four out of six specimens, specifically three TPU samples and one PLA sample, using the MCR 702 rheometer from Anton Paar (setup in Figure 2.3b).

Table 2.1: DMA testing parameters.

Setting	TPU	PLA
Temperature range	$[-20, 20]\,°\mathrm{C}$	$[-15, 20]\,°\mathrm{C}$
Relative strain (ε)	0.1%	0.03%
Sweep range	$[0.1, 10]$ Hz	$[1, 10]$ Hz

Table 2.1 summarizes the main settings used for DMA testing for the two materials. The isothermal frequency sweeps were conducted at $5°$C increments over the total range of temperature at 20 logarithmically spaced points in the selected frequency range. The maximum displacement is controlled by a fixed relative strain applied to the samples, selected to restrict material deformation to the linear domain.



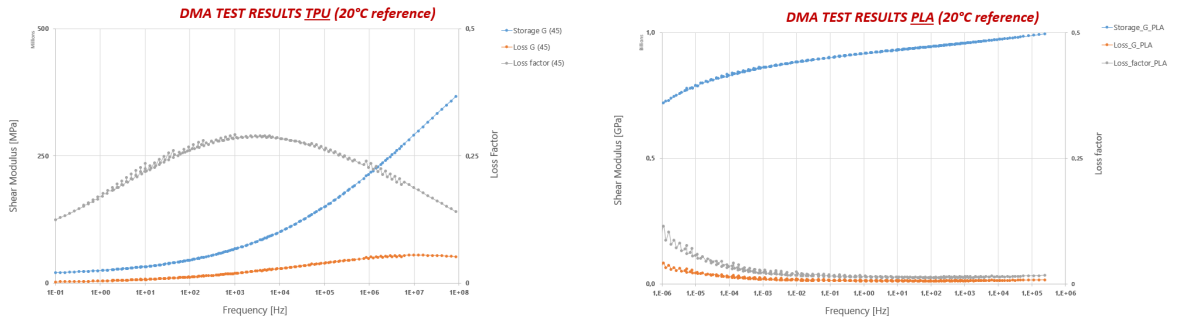
(a) **(b)**

Figure 2.3: Experimental testing overview showing: **(a)** the prepared TPU and PLA specimens (3 cases: $45°$ raster angle, $90°$ raster angle and different printing direction), and **(b)** the physical layout of the DMA testing setup.

The final master curves that characterize shear storage and loss modulus of PLA and TPU can be seen in Figure 2.4. The master curves regarding PLA indicate the creation of a plateau from approximately 10^{-2} Hz onwards. The scope of this project focuses on a narrower frequency range that goes from 1 to 5000 Hz, therefore the storage shear modulus is approximated for simplicity to a mean constant value of $G'_{\mathrm{PLA}} = 950$ MPa with a corresponding loss factor of 0.013. The real-valued bulk modulus is assumed frequency independent for both materials, this is because the available DMA data primarily characterize the shear response and not the volumetric response; therefore the bulk modulus master curve may follow a different trend. Moreover, Tschoegl (1989) shows that κ varies by one decade less than G, over the same relaxation time range. κ_{PLA} and κ_{TPU} are obtained using the isotropic relation for the storage modulus

$$\kappa_{\mathrm{PLA}} = \frac{2G'_{\mathrm{PLA}}(1+\nu)}{3(1-2\nu)}, \qquad \kappa_{\mathrm{TPU}} = \frac{2G'_{\mathrm{TPU}}(300)(1+\nu)}{3(1-2\nu)}. \tag{2.4}$$

The bulk modulus κ_{TPU} is fitted by taking the shear modulus around 300 Hz.



(a) **(b)**

Figure 2.4: Master curves at $20°$ reference temperature of **(a)** TPU 95A sample printed on the long side with $45°$ raster angle and **(b)** PLA sample printed on the long side with $45°$ raster angle

2.2. 3-degree-of-freedom system formulation

The isolator is designed to support a payload while reducing the transmission of base vibrations. The numerical model starts from the full finite-element description of the isolator domain formed by rigid and viscoelastic material. The two-dimensional domain $\mathcal{E}$ is discretized into bilinear quadrilateral finite elements under a plane-strain assumption. For each element e, the material properties are defined by the local material assigned to the element. Let N denote the number of displacement degrees of freedom of the finite-element isolator domain after applying the fixed boundary conditions. The mass matrix of the isolator is assembled from element contributions:

$$\mathbf{M} = \underset{e\in\mathcal{E}}{\mathbb{A}} \rho_e \mathbf{M}_e \in \mathbb{R}^{N\times N}, \tag{2.5}$$

where $\mathbb{A}$ denotes the finite-element assembly operation over all elements $e \in \mathcal{E}$, ρ_e is the corresponding material density and $\mathbf{M}_e$ is the unit mass matrix.

Since the viscoelastic material is represented through bulk and shear moduli, as discussed in Section 2.1, the element stiffness is decomposed into a volumetric and a shear contribution. The full isolator stiffness matrix is therefore assembled as

$$\mathbf{K}^*(\omega) = \underset{e\in\mathcal{E}}{\mathbb{A}} \left(\kappa_e \mathbf{K}_e^{(\kappa)} + G_e^*(\omega)\mathbf{K}_e^{(G)} \right) \in \mathbb{C}^{N\times N}. \tag{2.6}$$

Here, κ_e and $G_e^*(\omega)$ are respectively the SIMP interpolated bulk modulus and complex shear modulus of element e. The matrices $\mathbf{K}_e^{(\kappa)}$ and $\mathbf{K}_e^{(G)}$ are precomputed unit element stiffness matrices obtained by setting the two unit moduli $\kappa = 1$ and $G = 0$ and vice versa. This separation in the finite-element formulation is already implemented and discussed by Petrulis (2025), where the volumetric and shear stiffness contributions are assembled independently and then added together. Notably, in Equation 2.5 the mass matrix remains real-valued and frequency independent, while the stiffness matrix becomes complex and frequency-dependent as the shear modulus of the viscoelastic material is involved.

The full finite-element matrices describe the deformation of all nodal degrees of freedom in the isolator. However, the model in this work focuses on the rigid-body dominated motion of the payload-isolator system. Neglecting internal deformation modes, the dominant motions in 2D can be represented by three rigid-body coordinates: horizontal translation, vertical translation and in-plane rotation. The deformation of the total structure is therefore approximately ”reduced” to a coupled three-degree-of-freedom spring-mass system in $\mathbb{R}^3$. As shown in Figure 2.5, the total mass includes both the payload contribution and the effective mass contribution of the isolator, while the stiffness is provided only by the isolator. Let O denote the payload reference point located at the isolator interface and G the payload centre of mass. The payload has total mass m_G and mass moment of inertia I_G about the out-of-plane z-axis through G. These quantities are later used in Section 2.2.2 to derive the generalized payload mass matrix.

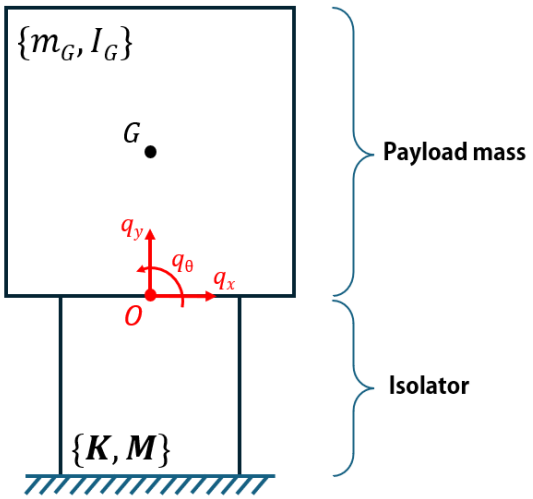


Figure 2.5: Isolator and payload system

In the selected coordinate space $\mathbb{R}^3$, we start by defining the generalized coordinate vector as

$$\mathbf{q} = \begin{bmatrix} q_x \\ q_y \\ q_\theta \end{bmatrix}, \tag{2.7}$$

where q_x and q_y are the translational displacements of the payload reference point (in $[\mathrm{m}]$), and q_θ is the in-plane rotation about the same point (in $[\mathrm{rad}]$). Figure 2.5 shows the reference frame scheme of the system. The corresponding canonical basis vectors are

$$\mathbf{e}_x = \begin{bmatrix} 1 \\ 0 \\ 0 \end{bmatrix}, \qquad \mathbf{e}_y = \begin{bmatrix} 0 \\ 1 \\ 0 \end{bmatrix}, \qquad \mathbf{e}_\theta = \begin{bmatrix} 0 \\ 0 \\ 1 \end{bmatrix}. \tag{2.8}$$

Consequently, any generalized displacement state can then be written as

$$\mathbf{q} = q_x \mathbf{e}_x + q_y \mathbf{e}_y + q_\theta \mathbf{e}_\theta. \tag{2.9}$$

The next step is to derive the stiffness and mass matrices in the new coordinate space.

2.2.1. Stiffness matrix

To obtain the generalized stiffness matrix $\tilde{\mathbf{K}}^*(\omega) \in \mathbb{C}^{3\times3}$, three independent displacement states are prescribed at the isolator domain top interface (visible in Figure 2.6). The two symmetric boundaries (highlighted in green in Figure 2.6) will represent the attachment points for the top payload and the fixed points at the base. The aim is to excite the isolator domain to obtain the deformations in the new three degrees of freedom. These prescribed vectors correspond to a unit displacement in x, a unit displacement in y, and a unit rotation θ about the chosen reference point.

For the rotational basis state defined as $\mathbf{u}_\theta$, the prescribed interface displacement follows the linearized rigid-body kinematics. For a node located at $\mathbf{v} = [x, y]^T$ in the 2D domain relative to the reference point, the horizontal and vertical displacement components associated with a generalized rotation q_θ are

$$\begin{bmatrix} u_{\theta,x} \\ u_{\theta,y} \end{bmatrix} = q_\theta \begin{bmatrix} -y \\ x \end{bmatrix}. \tag{2.10}$$

Since the reference point lies on the top interface, $y = 0$ for the prescribed nodes and we obtain

$$u_{\theta,x} = 0, \qquad u_{\theta,y} = q_\theta x. \tag{2.11}$$

The rotational basis is constructed using the unit generalized rotation $q_\theta = 1$. The prescribed displacement is therefore purely vertical along the top interface and varies linearly with the distance x.

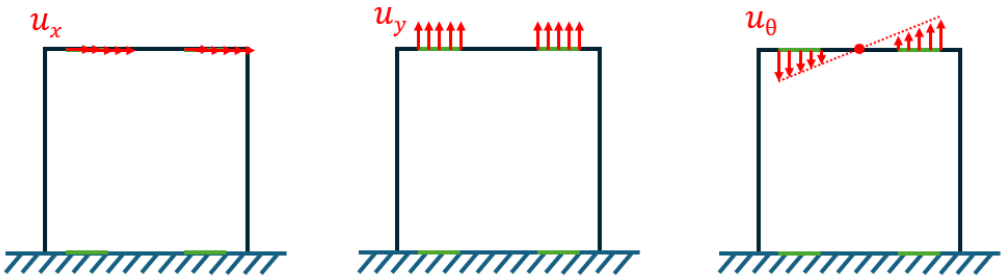


Figure 2.6: Prescribed displacements to three in-plane rigid-body modes. The green boundaries at the bottom defined fixed nodes, while the ones at the top define nodes subject to prescribed displacements. There two surfaces will represent the attachment points for the top payload.

The remaining degrees of freedom are solved from static equilibrium. For each prescribed generalized displacement $j \in \{x, y, \theta\}$, the full finite-element system in $\mathbb{C}^N$ can be partitioned into free and prescribed degrees of freedom as

$$\begin{bmatrix} \mathbf{K}^*_{ff}(\omega) & \mathbf{K}^*_{fp}(\omega) \\ \mathbf{K}^*_{pf}(\omega) & \mathbf{K}^*_{pp}(\omega) \end{bmatrix} \begin{bmatrix} \mathbf{u}_{j,f}(\omega) \\ \mathbf{u}_{j,p} \end{bmatrix} = \begin{bmatrix} \mathbf{0} \\ \mathbf{r}_{j,p}(\omega) \end{bmatrix}, \qquad j \in \{x, y, \theta\}. \tag{2.12}$$

Here, $\mathbf{u}_{j,p}$ is the prescribed boundary displacement pattern for the j-th generalized coordinate, $\mathbf{u}_{j,f}$ is the resulting displacement field in the free degrees of freedom, and $\mathbf{r}_{j,p}$ contains the reaction forces at the prescribed degrees of freedom.

$$\mathbf{u}_j(\omega) = \begin{bmatrix} \mathbf{u}_{j,f}(\omega) \\ \mathbf{u}_{j,p} \end{bmatrix}, \qquad \mathbf{f}_j(\omega) = \begin{bmatrix} \mathbf{0} \\ \mathbf{r}_{j,p}(\omega) \end{bmatrix}. \tag{2.13}$$

The complete displacement and force fields derived from the system of equations in 2.12, associated with all three degrees of freedom, are then collected as columns in the state matrices

$$\mathbf{U}(\omega) = \begin{bmatrix} | & | & | \\ \mathbf{u}_x\ (\omega) & \mathbf{u}_y\ (\omega) & \mathbf{u}_\theta\ (\omega) \\ | & | & | \end{bmatrix}, \qquad \mathbf{F}(\omega) = \begin{bmatrix} | & | & | \\ \mathbf{f}_x\ (\omega) & \mathbf{f}_y\ (\omega) & \mathbf{f}_\theta\ (\omega) \\ | & | & | \end{bmatrix} \tag{2.14}$$

where $\mathbf{U}(\omega), \mathbf{F}(\omega) \in \mathbb{C}^{N\times 3}$, the imaginary component represents the phase lag part of the fields. From here, the generalized stiffness matrix is obtained by projecting $\mathbf{U}(\omega)$ onto the reaction force matrix $\mathbf{F}(\omega)$:

$$\tilde{\mathbf{K}}^*(\omega) = \mathbf{U}^T(\omega)\mathbf{F}(\omega) \in \mathbb{C}^{3\times 3}. \tag{2.15}$$

This formula can be derived based on the strain-energy equivalence and virtual work (see Appendix A.1). The linear elastic equilibrium can now be described component-wise in this fashion:

$$\begin{bmatrix} F_x \\ F_y \\ M_z \end{bmatrix} = \underbrace{\begin{bmatrix} \widetilde{k}^*_{xx} & \widetilde{k}^*_{xy} & \widetilde{k}^*_{x\theta} \\ \widetilde{k}^*_{yx} & \widetilde{k}^*_{yy} & \widetilde{k}^*_{y\theta} \\ \widetilde{k}^*_{\theta x} & \widetilde{k}^*_{\theta y} & \widetilde{k}^*_{\theta\theta} \end{bmatrix}}_{\tilde{\mathbf{K}}^*(\omega)} \begin{bmatrix} q_x \\ q_y \\ q_\theta \end{bmatrix}. \tag{2.16}$$

The diagonal terms describe the direct stiffness associated with each generalized coordinate. The off-diagonal terms describe the coupling between the rigid-body motions. These coupling terms are important as during vibrations the base excitation in one direction can also excite rotation or motion in another direction.

2.2.2. Mass matrix

As previously established, the payload is represented analytically by an equivalent point mass m_{G} with inertia I_{G}. In the coupled system we can no longer use a diagonal mass matrix to represent the model. This is because the reference point of our rotational mode doesn't lie in the center of mass of the payload, as represented by the current system layout in Figure 2.7.

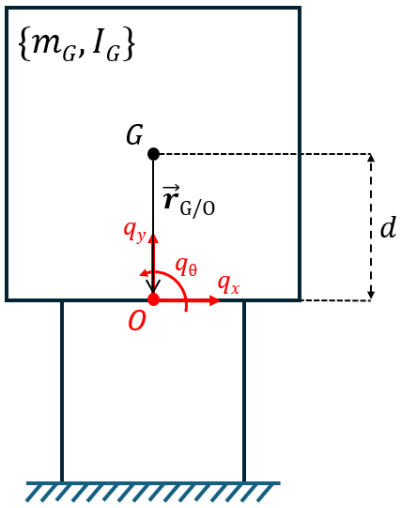


Figure 2.7: Payload geometry

We can derive the mass matrix related to the payload $\mathbf{M}_p$ following the calculations available at Appendix A.2, involving the kinematics and corresponding kinetic energy. The final coupled matrix is

$$\mathbf{M}_p = \begin{bmatrix} m_{\mathrm{G}} & 0 & -m_{\mathrm{G}}d \\ 0 & m_{\mathrm{G}} & 0 \\ -m_{\mathrm{G}}d & 0 & I_G + m_{\mathrm{G}}d^2 \end{bmatrix}. \tag{2.17}$$

Isolator mass contribution

Starting from the full mass matrix of the elements in the isolator domain (Equation 2.5), we can now project it onto the displacement state matrix $\mathbf{U}(\omega)$. By doing so, the generalized mass matrix related to the isolator is calculated:

$$\mathbf{M}_{\mathrm{iso}}(\omega) = \mathbf{U}_R^T(\omega)\mathbf{M}\mathbf{U}_R(\omega) \in \mathbb{R}^{3\times 3}. \tag{2.18}$$

In the present implementation, the real part $\mathbf{U}_R(\omega) = \Re\{\mathbf{U}(\omega)\}$ is used to project the real finite-element mass matrix, so that the final generalized matrix remains real-valued. This allows us to approximately

track the effective mass of the isolator that is contributing to each rigid body mode. Notably, here is where the frequency dependence gets captured in the mass matrix as it is now projected in $\mathbb{R}^3$ using $\mathbf{U}(\omega)$.

We can now sum together both the mass matrix of the payload and isolator to get the total generalized mass matrix:

$$\tilde{\mathbf{M}}(\omega) = \mathbf{M}_{\mathrm{p}} + \mathbf{M}_{\mathrm{iso}}(\omega) \in \mathbb{R}^{3\times 3}. \tag{2.19}$$

2.3. Non-linear eigenvalue problem

Now that both stiffness and mass matrices are derived, the dynamics of a linear mechanical system can first be expressed in the time domain as

$$\tilde{\mathbf{M}}\ddot{\mathbf{q}}(t) + \tilde{\mathbf{C}}\dot{\mathbf{q}}(t) + \tilde{\mathbf{K}}\mathbf{q}(t) = \mathbf{0}, \tag{2.20}$$

Here, $\tilde{\mathbf{C}}$ represents the conventional viscous contribution. In the present formulation, however, damping is not modeled explicitly using a damping matrix. Applying the Laplace transform gives

$$\left[s^2\widetilde{\mathbf{M}} + s\widetilde{\mathbf{C}} + \widetilde{\mathbf{K}}\right]\hat{\mathbf{q}}(s) = 0, \qquad s = \sigma + i\omega. \tag{2.21}$$

The real part σ of the Laplace variable describes exponential growth or decay, while the imaginary part ω represents the oscillation frequency. In this case, no exponential growth or decay is considered (steady-state), so $\sigma = 0$ and the system is evaluated on the imaginary axis ($s = i\omega$). The corresponding harmonic generalized displacement in Equation 2.20 can be written as

$$\mathbf{q}(t) = \Re\left\{\hat{\mathbf{q}}(\omega)e^{i\omega t}\right\}, \tag{2.22}$$

where $\hat{\mathbf{q}}(\omega)$ is the complex displacement phasor. Its magnitude represents the vibration amplitude, while its argument represents the phase relative to the chosen reference. In the model, the explicit damping term is incorporated already by the frequency-dependent complex stiffness

$$\tilde{\mathbf{K}}^*(\omega) = \tilde{\mathbf{K}}'(\omega) + i\tilde{\mathbf{K}}''(\omega) \in \mathbb{C}^{3\times 3}, \tag{2.23}$$

where $\tilde{\mathbf{K}}'(\omega)$ and $\tilde{\mathbf{K}}''(\omega)$ are respectively the storage and loss stiffness contributions. This formulation maintains physical consistency with the equation of motion by establishing the equivalence

$$\tilde{\mathbf{C}}_{\mathrm{eq}}(\omega) = \frac{\tilde{\mathbf{K}}''(\omega)}{\omega} \tag{2.24}$$

In the end, the steady-state harmonic equilibrium becomes

$$\left[\tilde{\mathbf{K}}^*(\omega) - \omega^2\tilde{\mathbf{M}}(\omega)\right]\hat{\mathbf{q}}(\omega) = 0. \tag{2.25}$$

For a free vibration problem, the frequency is no longer prescribed but becomes an unknown eigenvalue. Since the complex stiffness depends on frequency, the resulting eigenvalue problem to solve is nonlinear and can be written as:

$$\left[\tilde{\mathbf{K}}^*(\Omega_i) - \Omega_i^2\tilde{\mathbf{M}}(\Omega_i)\right]\boldsymbol{\phi}_i = \mathbf{0}, \qquad i \in \{x, y, \theta\}. \tag{2.26}$$

Here, Ω_i is the complex angular eigenfrequency and $\boldsymbol{\phi}_i \in \mathbb{C}^3$ is the corresponding generalized mode shape for the i^{th} rigid-body dominated mode. The real part of Ω_i describes the oscillation frequency (in $[\mathrm{rad/s}]$), while its imaginary part contains the damping information introduced by the complex stiffness.

The problem becomes nonlinear because the unknown eigenfrequency also determines the frequency-dependent shear modulus and therefore the generalized stiffness and mass matrices. If the shear modulus were frequency independent, a single pair of generalized matrices would be sufficient to calculate all three modes. However, this is not the case. Since the rigid body modes generally occur at different resonance frequencies, the material exhibits a different complex shear modulus at each resonance. Each mode must therefore be evaluated using its own mode-specific stiffness matrices $\tilde{\mathbf{K}}_x^*, \tilde{\mathbf{K}}_y^*, \tilde{\mathbf{K}}_\theta^*$ and the corresponding mass matrices. This results in three separate eigenvalue problems, each evaluated at the i^{th} mode. The three eigenvalue problems are coupled only through the common structural design, but their material properties and reduced matrices are evaluated separately.

A fixed-point iteration algorithm (Kelley 2018) is used to obtain a consistent frequency and complex shear modulus for each mode. At iteration k, the complex shear modulus of mode i is evaluated using the current frequency estimate (in Hz):

$$G_i^{(k)} = G^*\left(f_i^{(k)}\right), \qquad f_i = \frac{\Re\{\Omega_i\}}{2\pi} \quad [\mathrm{Hz}]. \tag{2.27}$$

Note:

The method requires an initial estimate of the three modal frequencies set by the user. The initial complex shear modulus for each mode is then obtained directly from the fitted material master curve:

$$G_i^{(0)} = G^*\left(f_i^{(0)}\right). \tag{2.28}$$

The corresponding global stiffness and mass matrices are then assembled and reduced in $\mathbb{R}^3$ as previously discussed. Next, the generalized eigenvalue problem is solved using the matrices evaluated at iteration k:

$$\left[\tilde{\mathbf{K}}_i^{*(k)} - \left(\Omega_i^{(k+1)}\right)^2 \tilde{\mathbf{M}}_i^{(k)}\right] \boldsymbol{\phi}_i^{(k+1)} = \mathbf{0}, \qquad i \in \{x, y, \theta\}. \tag{2.29}$$

After sorting the eigenpairs according to their effective modal mass (see Appendix A.3), the eigenfrequency associated with the targeted rigid-body motion is retained. To improve numerical stability in the algorithm, the frequency is ”relaxed” and updated according to

$$\hat{f}_i^{(k+1)} = (1-\alpha)\hat{f}_i^{(k)} + \alpha f_i^{(k+1)}, \tag{2.30}$$

where $\alpha = 0.9$ is the relaxation factor used in our case. The three mode-specific iterations are considered converged when the largest relative change among their frequencies satisfies

$$\varepsilon^{(k+1)} = \max_{i\in\{x,y,\theta\}} \left| \frac{\hat{f}_i^{(k+1)} - \hat{f}_i^{(k)}}{\hat{f}_i^{(k)}} \right| < \varepsilon_{\mathrm{tol}}. \tag{2.31}$$

In the implementation, $\varepsilon_{\mathrm{tol}} = 10^{-2}$ and at most five fixed-point iterations are performed. The full algorithm scheme is summarized in Figure 2.8 here below.

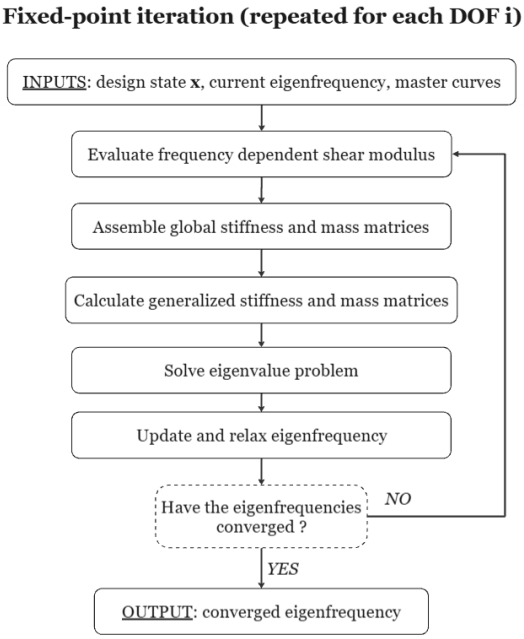


Figure 2.8: Fixed-point algorithm loop scheme

Once convergence is reached, the procedure provides the three final structural eigenfrequencies

$$\boldsymbol{\Omega} = \begin{bmatrix} \Omega_x & \Omega_y & \Omega_\theta \end{bmatrix}^T, \tag{2.32}$$

together with the corresponding complex shear moduli, evaluated at the corresponding frequencies in Hz

$$G_i^* = G^*(f_i), \qquad i \in \{x, y, \theta\}. \tag{2.33}$$

The final material moduli are used to evaluate the associated mode-specific matrices, eigenfrequencies and mode shapes. Since the converged eigenfrequencies are complex, their imaginary components also provide the modal damping information. For each mode, the damping ratio (Casiano 2016) and corresponding quality factor are evaluated as

$$\zeta_i = \frac{\mathrm{Im}\{\Omega_i\}}{\sqrt{\mathrm{Re}\{\Omega_i\}^2 + \mathrm{Im}\{\Omega_i\}^2}}, \qquad Q_i = \frac{1}{2\zeta_i}. \tag{2.34}$$

A lower Q_i therefore corresponds to a more strongly damped rigid-body mode.

2.4. Frequency response analysis

The nonlinear eigenvalue analysis determines the resonance frequencies and damping characteristics of the three rigid-body dominated modes. To now evaluate the isolation performance over a continuous frequency range, the response of the payload to a prescribed harmonic base motion is considered.

Let $\mathbf{q}(t)$ denote the absolute generalized displacement of the payload and let $\mathbf{q}_b(t)$ denote the corresponding generalized displacement of the base. Both vectors are described in the three generalized system coordinates (horizontal translation, vertical translation and in-plane rotation) and are represented in Figure 2.9.

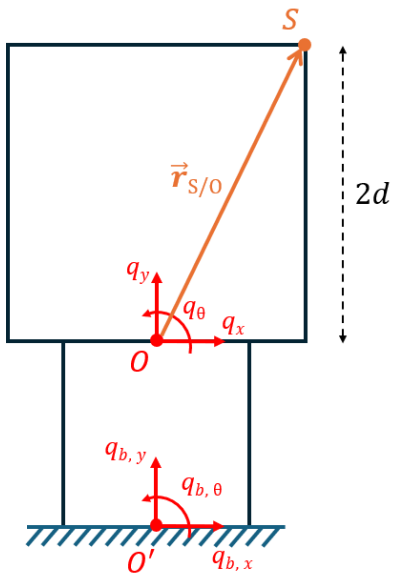


Figure 2.9: Base and payload reference frames

The equation of motion in the time-domain can be written as follows:

$$\tilde{\mathbf{M}}(\omega)\ddot{\mathbf{q}} + \tilde{\mathbf{K}}^*(\omega)\left(\mathbf{q} - \mathbf{q}_b\right) = \mathbf{0}. \tag{2.35}$$

The inertia depends on the absolute payload motion, while the isolator stiffness acts on the relative displacement. We can formulate the relative deformation experienced by the isolator with

$$\mathbf{q}_{\mathrm{rel}}(t) = \mathbf{q}(t) - \mathbf{q}_b(t). \tag{2.36}$$

In the Laplace domain, the new equilibrium is therefore

$$-\omega^2\tilde{\mathbf{M}}(\omega)\hat{\mathbf{q}}(\omega) + \tilde{\mathbf{K}}^*(\omega)\hat{\mathbf{q}}_{rel}(\omega) = \mathbf{0}. \tag{2.37}$$

Using Equation 2.36 we rewrite the equilibrium as

$$\left[\tilde{\mathbf{K}}^*(\omega) - \omega^2\tilde{\mathbf{M}}(\omega)\right]\hat{\mathbf{q}}_{\mathrm{rel}}(\omega) = \omega^2\tilde{\mathbf{M}}(\omega)\hat{\mathbf{q}}_b(\omega). \tag{2.38}$$

The compliance frequency-response matrix is defined as

$$\mathbf{H}(\omega) = \left[\tilde{\mathbf{K}}^*(\omega) - \omega^2\tilde{\mathbf{M}}(\omega)\right]^{-1} \in \mathbb{C}^{3\times 3}, \tag{2.39}$$

and the relative response is consequently

$$\hat{\mathbf{q}}_{\mathrm{rel}}(\omega) = \omega^2\mathbf{H}(\omega)\tilde{\mathbf{M}}(\omega)\hat{\mathbf{q}}_b(\omega). \tag{2.40}$$

The absolute payload displacement is the sum of the relative and base motions. Therefore,

$$\hat{\mathbf{q}}(\omega) = \left[\mathbf{I}_3 + \omega^2\mathbf{H}(\omega)\tilde{\mathbf{M}}(\omega)\right]\hat{\mathbf{q}}_b(\omega). \tag{2.41}$$

The transmissibility matrix is defined through the input-output relationship of the system, it follows that

$$\mathbf{T}(\omega) = \frac{\hat{\mathbf{q}}(\omega)}{\hat{\mathbf{q}}_b(\omega)} = \mathbf{I}_3 + \omega^2 \mathbf{H}(\omega)\tilde{\mathbf{M}}(\omega). \tag{2.42}$$

This matrix maps the generalized base motion to the absolute payload motion. The diagonal entries describe direct transmission in the corresponding direction, while the off-diagonal entries describe coupling between the different directions. For one independently imposed base component j, an individual transmissibility entry can be written in terms of either displacement or acceleration as

$$T_{ij}(\omega) = \frac{\hat{q}_i(\omega)}{\hat{q}_{b,j}(\omega)}, \qquad T_{ij}(\omega) = \frac{\hat{a}_i(\omega)}{\hat{a}_{b,j}(\omega)}, \qquad i, j \in \{x, y, \theta\}. \tag{2.43}$$

Because harmonic displacement and acceleration are related by the same factor ω^2, the two expressions are equivalent and the same transmissibility matrix relates both payload and base motion.

For comparison with the experimental measurements, the payload response is evaluated at the position of the output accelerometer rather than at the bottom center of the payload. Since the payload is assumed rigid and rotations are small, the displacement of the final point S (visible in Figure 2.9) located at (r_x, r_y) from the reference point O is obtained through the linear rigid-body transformation

$$\hat{\mathbf{q}}_{\mathrm{S}}(\omega) = \mathbf{R}_{\mathrm{S}}\hat{\mathbf{q}}(\omega), \qquad \mathbf{R}_{\mathrm{S}} = \begin{bmatrix} 1 & 0 & -r_y \\ 0 & 1 & r_x \\ 0 & 0 & 1 \end{bmatrix}, \tag{2.44}$$

where r_x and r_y are the horizontal and vertical offsets of the sensor from the payload reference point O. For the full derivation, see Appendix A.4. For the sensor located at the top right corner of the payload, the coordinates become $r_x = d$ and $r_y = 2d$, where $2d$ is the side of the square payload. The updated transmissibility evaluated at the sensor position therefore becomes

$$\bar{\mathbf{T}}(\omega) = \mathbf{R}_{\mathrm{S}}\mathbf{T}(\omega). \tag{2.45}$$

Unlike the nonlinear eigenvalue problem, the excitation frequency is prescribed during the frequency response analysis and doesn't vary, so no fixed-point iteration is required. At every frequency point, the complex shear modulus $G^*(\omega)$ is evaluated directly, the reduced stiffness and mass matrices are updated and the corresponding value of $\bar{\mathbf{T}}(\omega)$ is calculated. Repeating this procedure sweeping over the selected frequency range produces the complete transmissibility curve.

In this case, a conventional modal superposition method is not used to compute the frequency response, because the shear modulus varies with frequency and so do associated reduced matrices and mode shapes. A solution based on mode superposition is traditionally evaluated for one material state and this would effectively freeze part of this dependence.

2.5. Stress calculations

The reduced eigenvalue and frequency-response models describe the global motion of the payload–isolator system. To assess whether the resulting deformation is structurally admissible, the corresponding local stress field in the isolator must also be evaluated. This calculation is introduced here independently of the topology-optimization formulation. The resulting stress measure will later be used to formulate the stress constraints described in Chapter 3.

A prescribed base acceleration amplitude is defined in the generalized coordinate space as

$$\mathbf{a}_b = \begin{bmatrix} a_x \\ a_y \\ 0 \end{bmatrix}, \tag{2.46}$$

where the rotational component is zero because only horizontal and vertical base accelerations are imposed. The associated inertial load applied by the payload is

$$\mathbf{f}_{\text{ext}} = \mathbf{M}_{\text{p}}\mathbf{a}_b, \tag{2.47}$$

where $\mathbf{M}_{\text{p}}$ is the derived payload mass matrix. Inertial loading that can arise from the isolator itself is not included in this case, so $\mathbf{M}_{\text{p}}$ is used instead of $\tilde{\mathbf{M}}(\omega)$.

The stress response is evaluated separately at the three converged rigid-body resonance frequencies, where the largest dynamic stresses are generally expected. For mode case $i \in \{x, y, \theta\}$, the real angular frequency used in the harmonic response is

$$\omega_i = 2\pi f_i = \Re\{\Omega_i\}. \tag{2.48}$$

The corresponding complex generalized displacement amplitude is obtained from

$$\hat{\mathbf{q}}_i = \left[\tilde{\mathbf{K}}_i^*(\omega_i) - \omega_i^2\tilde{\mathbf{M}}_i(\omega_i)\right]^{-1}\hat{\mathbf{f}}_{\text{ext}}. \tag{2.49}$$

Here, $\tilde{\mathbf{K}}^*$ and $\tilde{\mathbf{M}}_i$ are the converged matrices obtained from the iterative process described in Section 2.3. The same prescribed acceleration is evaluated at each resonance; therefore, the index i identifies the resonance under consideration, not the direction of the imposed acceleration. Since the FEM formulation and constitutive model are linear, it is worth noting that strain and stress amplitudes scale linearly with the prescribed acceleration $\mathbf{a}_b$ specified as input.

The generalized displacement is subsequently mapped back to the finite-element domain using the corresponding displacement basis,

$$\hat{\mathbf{u}}_i \approx \mathbf{U}_i\hat{\mathbf{q}}_i \in \mathbb{C}^N. \tag{2.50}$$

This reconstruction retains the dynamic amplification and coupling of the generalized system. It is an approximation because the displacement field is restricted to the three prescribed interface deformation states contained in $\mathbf{U}_i$; internal deformation modes outside this reduced basis are neglected.

For each element e, the complex strain amplitude is calculated from the strain-displacement relation,

$$\hat{\boldsymbol{\varepsilon}}_{e,i} = \mathbf{B}_e\hat{\mathbf{u}}_{e,i}, \tag{2.51}$$

where $\mathbf{B}_e$ is the element strain-displacement matrix. The same element strain is also used to evaluate the strain energy distribution, with particular attention to the shear strain energy as an indicator of where the viscoelastic material contributes most strongly to deformation and damping. The corresponding in-plane complex stress is then

$$\hat{\boldsymbol{\sigma}}_{e,i} = \mathbf{D}_{e,i}\hat{\boldsymbol{\varepsilon}}_{e,i}, \tag{2.52}$$

with the constitutive matrix $\mathbf{D}_{e,i}$ decomposed into volumetric and shear contributions. Note that $\mathbf{D}_{e,i}$ depends on which vibration mode i we are evaluating, while $\mathbf{B}_e$ is only dependent on the element geometry. The energy expressions and the decomposition of the constitutive matrix follow Petrulis (2025).

The finite-element model is formulated under plane strain conditions. Therefore,

$$\hat{\varepsilon}_{zz,e,i} = 0, \tag{2.53}$$

but the out-of-plane normal stress is generally non-zero. It is calculated using the standard constitutive model formulas (Bower 2009):

$$\hat{\sigma}_{zz,e,i} = \lambda_{e,i}\left(\hat{\varepsilon}_{xx,e,i} + \hat{\varepsilon}_{yy,e,i}\right), \qquad \lambda_{e,i} = \kappa_e - \frac{2}{3}G^*_{e,i}. \tag{2.54}$$

The complete stress phasor used for the equivalent-stress calculation is therefore

$$\hat{\boldsymbol{\sigma}}_{e,i} = \begin{bmatrix} \hat{\sigma}_{xx,e,i} \\ \hat{\sigma}_{yy,e,i} \\ \hat{\sigma}_{zz,e,i} \\ \hat{\tau}_{xy,e,i} \end{bmatrix} \in \mathbb{C}^4. \tag{2.55}$$

Because the calculation is performed in the frequency domain, this complex vector is not the instantaneous physical stress. For any real instantaneous plane-strain stress state, the von Mises stress (Bower 2009) would be calculated as

$$\sigma_{\mathrm{vm}} = \sqrt{\frac{1}{2}\left[(\sigma_{xx} - \sigma_{yy})^2 + (\sigma_{yy} - \sigma_{zz})^2 + (\sigma_{zz} - \sigma_{xx})^2\right] + 3\tau_{xy}^2}. \tag{2.56}$$

Since this expression is nonlinear in the stress components, the maximum stress over the cycle cannot be obtained by taking only the real part or the magnitude of the complex stress components. Instead, the stress phasor is decomposed as

$$\hat{\boldsymbol{\sigma}}_{e,i} = \boldsymbol{\sigma}_{R,e,i} + i\boldsymbol{\sigma}_{I,e,i}, \tag{2.57}$$

and quadratic von Mises terms are defined as

$$\begin{aligned} X_{e,i} &= \boldsymbol{\sigma}_{R,e,i}^T \mathbf{V} \boldsymbol{\sigma}_{R,e,i}, \\ Y_{e,i} &= \boldsymbol{\sigma}_{I,e,i}^T \mathbf{V} \boldsymbol{\sigma}_{I,e,i}, \\ Z_{e,i} &= \boldsymbol{\sigma}_{R,e,i}^T \mathbf{V} \boldsymbol{\sigma}_{I,e,i}, \end{aligned} \tag{2.58}$$

where $\mathbf{V}$ is the quadratic matrix associated with the plane-strain von Mises expression. The peak equivalent stress reached during one harmonic cycle is then

$$\sigma_{\mathrm{vm,peak},e,i} = \sqrt{\frac{1}{2}\left[X_{e,i} + Y_{e,i} + \sqrt{\left(X_{e,i} - Y_{e,i}\right)^2 + 4Z_{e,i}^2}\right]}. \tag{2.59}$$

The complete derivation of Equation (2.59) is provided in Appendix A.5.

For verification, the calculated peak stresses are compared with the respective COMSOL Multiphysics simulation results. Moreover, to check numerically the stress distributions between the FEM model in Python and COMSOL more robustly, the total element stresses in the domain are aggregated using the mean P-norm formula

$$\sigma_P = \left(\frac{1}{N}\sum_{e=1}^{N} \sigma_{\mathrm{vm,peak},e}^P\right)^{1/P}. \tag{2.60}$$

where $P = 10$.

3

Topology optimization

3.1. Multi-material topology optimization formulation

Chapter 2 established the relation between the material distribution in the isolator and its generalized stiffness, mass, eigenfrequencies, damping and stress response. The same model is now embedded in the density-based topology optimization framework built by Petrulis (2025) to determine the spatial distribution of the rigid and viscoelastic phases.

The design domain contains N_e finite elements. Each element is assigned a continuous design variable x_e, collected in

$$\mathbf{x} = \begin{bmatrix} x_1 & x_2 & \cdots & x_{N_e} \end{bmatrix}^T, \qquad 0 \leq x_e \leq 1. \tag{3.1}$$

The limiting values $x_e = 0$ and $x_e = 1$ represent the viscoelastic and rigid material phases, respectively. Before the material properties are evaluated, the design variables are passed through a density filter. This suppresses mesh-scale oscillations and imposes a minimum spatial length scale. The filtered variable $\widetilde{x}_e$ is subsequently transformed using a smooth Heaviside projection,

$$\overline{x}_e = \frac{\tanh(\beta\eta) + \tanh[\beta(\widetilde{x}_e - \eta)]}{\tanh(\beta\eta) + \tanh[\beta(1-\eta)]}, \tag{3.2}$$

where η is the projection threshold and β controls the sharpness of the transition. The value of β is gradually increased during the optimization so that intermediate densities are initially allowed, while the final design is driven towards a more discrete distribution. Prescribed rigid and void regions are imposed after this projection and are therefore excluded from the design update, this will be better clarified in the specific design case study in Section 4.1.

The projected design variable $\overline{x}_e$ is then used to interpolate the element properties between the two material phases. Following the SIMP formulation, the bulk modulus, complex shear modulus and density are evaluated as

$$\begin{aligned} \kappa_e(\overline{x}_e) &= \kappa_{\mathrm{TPU}} + (\kappa_{\mathrm{PLA}} - \kappa_{\mathrm{TPU}})\, \overline{x}_e^{\,p}, \\ G^*_{e,i}(\overline{x}_e) &= G^*_{\mathrm{TPU},i} + \left(G^*_{\mathrm{PLA},i} - G^*_{\mathrm{TPU},i}\right) \overline{x}_e^{\,p}, \\ \rho_e(\overline{x}_e) &= \rho_{\mathrm{TPU}}(1 - \overline{x}_e) + \rho_{\mathrm{PLA}}\overline{x}_e, \qquad\qquad i \in \{x, y, \theta\}, \end{aligned} \tag{3.3}$$

where p is the penalization exponent. The material densities used in the interpolation are $\rho_{\mathrm{TPU}} = 1220\ \mathrm{kg/m^3}$ and $\rho_{\mathrm{PLA}} = 1240\ \mathrm{kg/m^3}$, taken from the manufacturer technical data sheets (Bambu Lab 2026b; Bambu Lab 2026a). It is important to note that the shear modulus of the viscoelastic phase is evaluated separately at the frequency of each rigid-body mode because of its frequency dependence, while the bulk modulus is assumed frequency independent as already assessed in Section 2.1.

The objective is to increase damping while retaining sufficient stiffness in all three rigid-body directions. Instead of maximizing an eigenfrequency directly, the quality factor is minimized. A lower quality factor corresponds to greater modal damping, whereas lower bounds on the eigenfrequencies prevent the optimizer from obtaining damping merely by producing an excessively compliant isolator.

In the multi-mode formulation used in this work, the objective is the P-mean of the three quality factors,

$$J_Q(\mathbf{x}) = \left[\frac{Q_x^P(\mathbf{x}) + Q_y^P(\mathbf{x}) + Q_\theta^P(\mathbf{x})}{3}\right]^{1/P}, \qquad P = 4. \tag{3.4}$$

This formulation gives greater weight to the least-damped mode while remaining differentiable. The implementation can alternatively minimize a single selected quality factor Q_i.

The optimization problem is consequently written as

$$\begin{aligned} \underset{\mathbf{x}}{\text{minimize}} \quad & Q_i(\mathbf{x}) \ \vee \ J_Q(\mathbf{x}) \\ \text{subject to} \quad & f_i(\mathbf{x}) \geq f_{\min,i}, \qquad i \in \{x, y, \theta\}, \\ & 0 \leq x_e \leq 1, \qquad e = 1, \ldots, N_e. \end{aligned} \tag{3.5}$$

No volume constraint is imposed in the present implementation. The amount of each material is instead determined by the damping objective, the eigenfrequency limits, the prescribed non-design regions and, when enabled, the stress constraint introduced in Section 3.2.

The problem is solved using the Method of Moving Asymptotes (MMA) (Svanberg 1987). At every outer iteration, the current responses and their sensitivities with respect to the common design vector are evaluated, after which MMA generates a new material distribution. A move limit of 0.1 restricts the change of each design variable between consecutive iterations. The optimization terminates when the relative change of the design vector falls below 10^{-4} or when the maximum number of iterations is reached.

The objective and constraint design sensitivities are evaluated using PyMOTO's differentiation framework (Delissen 2023). Within this framework, each module computes its local derivatives. PyMOTO then uses backpropagation, applying the chain rule to combine these local derivatives into the final gradients required by the MMA algorithm.

The material interpolation cannot be evaluated only once during an MMA iteration because the viscoelastic shear modulus depends on the unknown modal frequencies, which themselves depend on the current material distribution. The fixed-point algorithm introduced in Section 2.3 is therefore embedded as an inner loop within every outer MMA iteration. Figure 3.1 summarizes the resulting nested procedure: the outer loop updates the material distribution, while the inner loop makes the frequency-dependent shear modulus consistent for the current design before the objective and constraints are passed back to MMA.

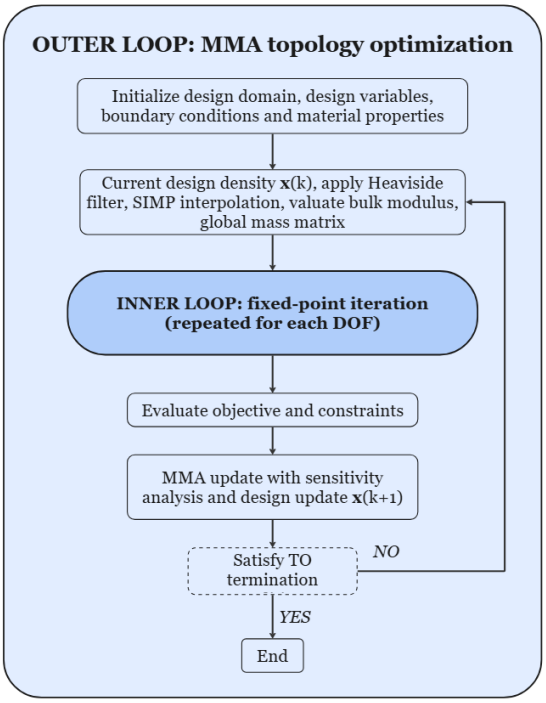


Figure 3.1: Nested topology optimization and fixed-point iteration procedure.

The frequency-dependent topology optimization formulation introduces additional computational cost compared with topology optimization using constant material properties. For a frequency-independent material, the structural matrices need to be assembled and reduced only once per MMA iteration. Here, this procedure is repeated within the fixed-point iteration for each of the three rigid-body modes. With a maximum of five fixed-point iterations, so up to 15 matrix evaluations can be required during one MMA iteration. For reference, during the creation of the tested designs later analyzed in Chapter 5, the fixed-point algorithm required three iterations on average to converge, with convergence generally becoming faster during the later stages of the topology optimization. The main computational cost comes from the repeated full finite-element assemblies, solving the system described in Equation 2.12 and sensitivity evaluation, whereas solving the eigenvalue problem is comparatively inexpensive.

3.2. Stress constraint

The optimization objective and eigenfrequency constraints control the global dynamic response, but they do not by themselves prevent local overstressing of the isolator. The elementwise peak von Mises stress derived in Section 2.5 is therefore introduced as an additional structural constraint.

For each element e and resonance case i, the peak von Mises stress is converted into a normalized local constraint,

$$g_{e,i} = \frac{\sigma_{\mathrm{vm,peak},e,i}}{\sigma_{\mathrm{lim},e}} - 1. \tag{3.6}$$

A value $g_{e,i} \leq 0$ indicates that the element stress does not exceed its interpolated allowable value. Because intermediate material states may occur during the optimization, the allowable material strength $\sigma_{\mathrm{lim},e}$ must also be extended and defined throughout the whole interval $0 \leq \overline{x}_e \leq 1$ via linear interpolation:

$$\sigma_{\mathrm{lim},e} = (1 - \overline{x}_e)\sigma_{\mathrm{lim,TPU}} + \overline{x}_e \sigma_{\mathrm{lim,PLA}}. \tag{3.7}$$

Here, $\sigma_{\mathrm{lim,TPU}}$ and $\sigma_{\mathrm{lim,PLA}}$ are the allowable stresses of the viscoelastic and stiff phases, respectively. In the present model, values of $\sigma_{\mathrm{lim,TPU}} = 27\ \mathrm{MPa}$ and $\sigma_{\mathrm{lim,PLA}} = 25\ \mathrm{MPa}$ are adopted based on experimental strength data for 3D-printed TPU 95A (Sardinha et al. 2025) and PLA (Wang et al. 2023), respectively. No separate interfacial strength or failure criterion is included, so material interfaces are represented through the same continuous interpolation used by the finite-element model.

Imposing one constraint for every element and every resonance case would result in a very large optimization problem. The normalized local constraints are therefore combined for each resonance using the differentiable P-mean aggregation proposed by Verbart, Langelaar, and Keulen (2017):

$$G_{\sigma,i} = \left[\frac{1}{N_e} \sum_{e=1}^{N_e} \left(g_{e,i} + 1 \right)^{P_\sigma} \right]^{1/P_\sigma} - 1, \qquad P_\sigma = 10. \tag{3.8}$$

A larger aggregation exponent gives greater weight to highly stressed elements and approaches the maximum local constraint more closely. The selected value $P_\sigma = 10$ provides a compromise between localization and numerical smoothness. The three aggregates, calculated at each resonance mode i, are subsequently combined through a Kreisselmeier–Steinhauser smooth maximum,

$$G_\sigma = \mathrm{KS}_{\rho_{\mathrm{KS}}} \left(G_{\sigma,x}, G_{\sigma,y}, G_{\sigma,\theta} \right), \qquad \rho_{\mathrm{KS}} = 30, \tag{3.9}$$

and the global stress requirement is

$$G_\sigma \leq 0. \tag{3.10}$$

This formulation produces one differentiable stress constraint for MMA while accounting for the complete element field and all three resonance cases, where usually stresses are higher. It is important to note that the aggregation is an approximation and does not enforce exactly every local stress constraint. It reduces the influence of one isolated numerical peak, but it does not remove stress singularities or mesh dependence.

4

Experimental method

4.1. Case study design

With the dynamical model and topology optimization algorithm set, the isolator design domain must now be adapted to be compatible with the experimental setup.

Two lower and two upper attachments are added for connection to the base and payload, respectively. They are modeled as stiff rectangles and placed at the four corners. The respective design variables x'_e assigned to the elements used for these fixtures are equally set to 1 to create the attachments with the stiffer material. This effectively creates a mask that overwrites the elements set by the topology optimization algorithm at each iteration.

The same strategy is used to create two lateral empty areas between the rigid attachments. These are added to create space for the bolts that later fix the isolator. In this case, the respective design variables x''_e are set to 0 together with their density value. To make the material behave similarly to void, the associated unit element stiffness matrices $\mathbf{K}_e^{(\kappa)}$ and $\mathbf{K}_e^{(G)}$ are computed using an infinitesimal value of 10^{-4} for the moduli $G^*(\omega)$ and κ. The elements therefore remain in the fixed numerical mesh but contribute negligibly to its stiffness and mass.

Using the same settings, two very thin empty areas are left at the top and bottom of the domain. This is done to let the isolator structure deform vertically while vibrating without touching the base nor the payload. The remaining middle area is left free to change by the topology optimization, with the corresponding design variables x_e assigned to 0.5 at the initial MMA iteration.

The nodes located symmetrically on the two bottom attachments are fixed, which means any displacement is set to zero. At the corresponding positions on the top interface, prescribed displacements are applied to the top nodes to excite the structure in the three degrees of freedom, as already illustrated in Section 2.2.1. Figure 4.1 shows the final customized initial domain set in the optimization together with the relevant assigned dimensions, sub-domains and boundary conditions (in green) at the top and bottom attachments. The mesh forming the total 2D domain is divided into 150×150 linear quadrilateral elements.

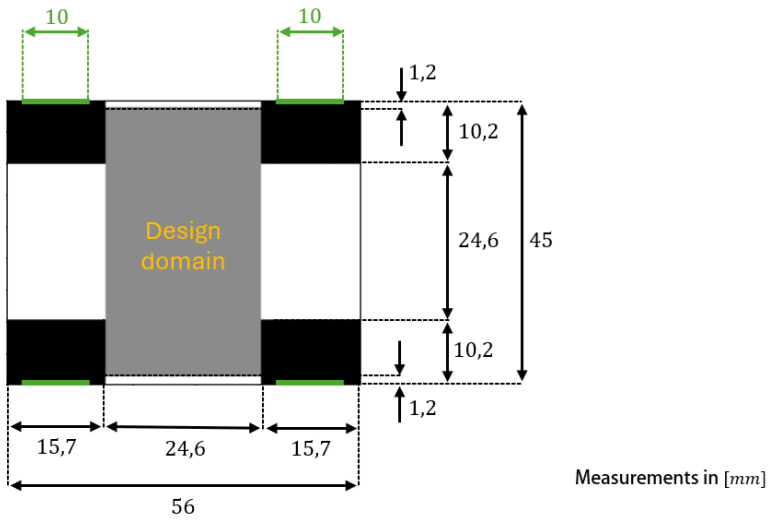


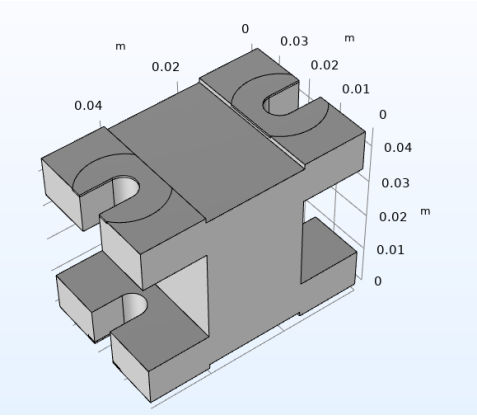
Figure 4.1: Initial topology optimization domain with relevant dimensions (in mm).

4.1.1. 3D model design

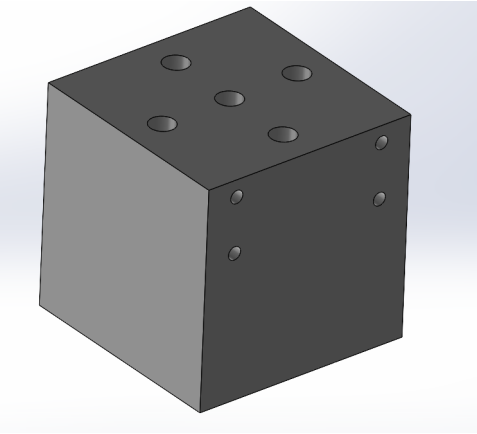
The next step is to convert the optimized two-dimensional geometry into a three-dimensional model. Since the topology optimization result is defined on a discrete grid, the material interfaces initially present a stepped boundary. The interface contours are therefore extracted and interpolated with smooth curves before generating the CAD geometry. This removes irregularities and provides continuous boundaries suitable for COMSOL simulations and additive manufacturing.

The final design is extruded by $35\,\mathrm{mm}$ along the z-direction. Holes are then cut through at the mid-plane of the extrusion in the attachment regions to accommodate connecting $\mathrm{M6}$ bolts. The non-optimized base isolator model can be seen in Figure 4.2a.

The payload is modeled as a cube with dimensions $60 \times 60 \times 60\ \mathrm{mm}^3$ and is shown in Figure 4.2b. Five through-holes of the same diameter are created in the central and lateral regions of the payload to enable the bolted connections between the payload and the isolator structure. Additional smaller holes at the side are added to screw in Arduino accelerometers used for an alternative experimental setup.



(a) 3D base isolator CAD model used in COMSOL.



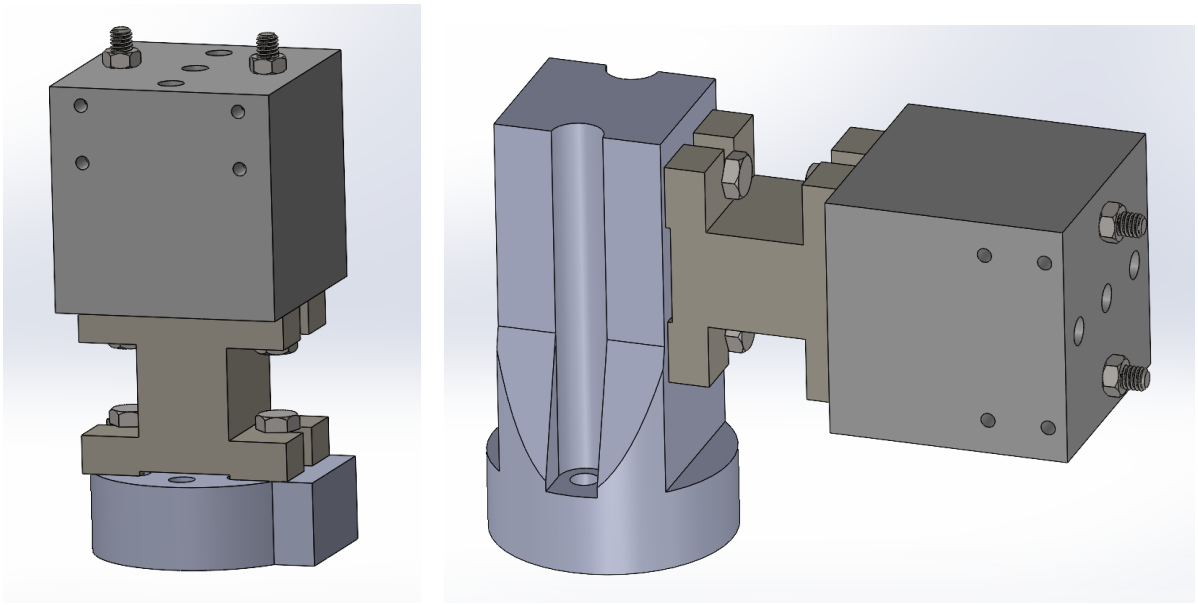
(b) Payload 3D model.

Figure 4.2: 3D CAD models of the base isolator and payload.

The prescribed boundary conditions at the base and payload are also modified. In the 3D isolator, boundary surfaces on the attachments are modeled based on a simplified pressure-cone method (Budynas and Nisbett 2015), which predicts the pressure distribution created by a bolted joint. The pressure

areas are shown on the attachment surfaces in Figure 4.2a and define the corresponding boundary conditions (both at the top and bottom) in the 3D simulations.

A custom plate is also made to accommodate the sensor used to measure the acceleration at the base coming from the shaker. Two setup versions were modeled so that the isolator can be tested both with vertical and horizontal shaker excitations using the available equipment. The two full assemblies are visible in Figure 4.3.



(a) Vertical setup assembly **(b)** Horizontal setup assembly

Figure 4.3: CAD assemblies for vertical and horizontal shaker excitation.

Until now, the system studied in two dimensions had the plane-strain hypothesis, and accounted for a perfect extrusion in the z-direction of prescribed length. The introduction of holes for the bolts changes the isolator geometry, deviating the design from the output result in the framework.

4.2. Multi-material additive manufacturing

All models are made utilizing Fused Deposition Modeling (FDM) technology. In particular, the 3D isolator models are manufactured using the Bambu Lab H2D with dual nozzle, which makes multi-material printing possible; Table 4.1 shows the 3D printing settings.

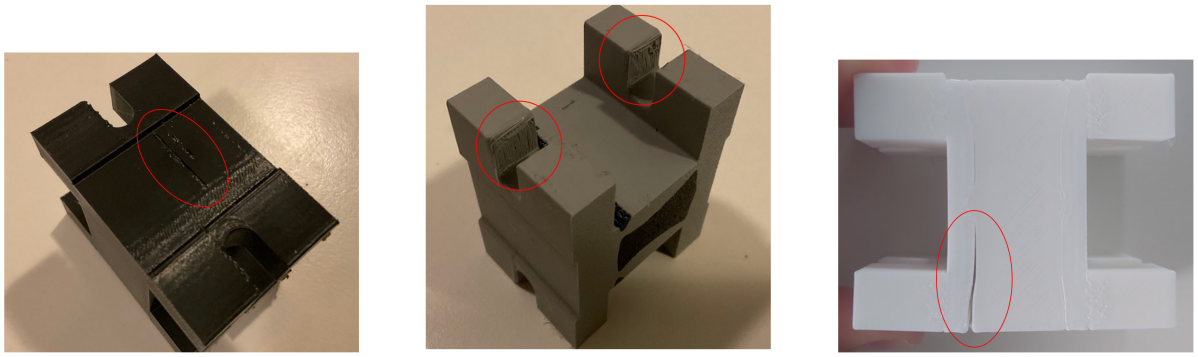
3D-printed structures can exhibit anisotropic material behaviour as layers are created to print the final product, depending on the printing direction. Experimental DMA results demonstrated this as the sample printed along the z-axis showed a drop in shear modulus compared to the other two tested samples, decreasing by up to 10% at higher frequencies. Instead, TPU samples printed at $45°$ and $90°$ nozzle direction exhibited nearly identical material properties.

Table 4.1: 3D Printing Settings

Parameter	Value
Infill	100%
Nozzle size	0.4 mm
Layer height	0.15 mm

Defects can be identified on the printed structures, specifically:

- Layer shifting in the extruded direction (Figure 4.4a);
- Drooping of surfaces under weak supports (Figure 4.4b);
- Delamination caused by weak adhesion between TPU and PLA extruded filament (Figure 4.4c).



(a) Layer shifting. **(b)** Drooping. **(c)** Delamination.

Figure 4.4: Examples of manufacturing defects observed in the printed isolators.

4.2.1. Interface bonding

Two ways have been considered to prevent delamination and separation between surfaces: the application of instant superglue (Loctite 406) and the use of interlocking features.

The interface between the rigid attachment region and the optimized domain can be particularly sensitive when TPU is present, as the connection in itself is already thin and has to bear the majority of the load of the payload. Interlocking features are implemented specifically at these interfaces and are custom modeled using SOLIDWORKS during post-processing. An example of these features can be seen in Figure 4.5.

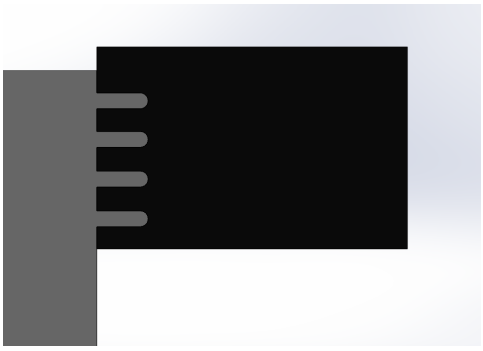


Figure 4.5: Interlocking feature implementation.

While the final tested designs rely solely on interlocking features, in earlier 3D-printed models superglue (Loctite® 406) was applied in some areas.

4.3. Testing procedure

The experimental setup used to characterize the isolator is shown in Figure 4.6. The input signal is generated using a Siglent SDG1032X Plus function generator. The electrical signal is then sent to a BAA 120 power amplifier before driving the TIRA TV 51110 electrodynamic shaker. The signal amplitude is adjusted a second time in the amplifier using the gain to change the voltage, together with a set current limit.

The tested assembly is rigidly connected to the base of the shaker. During the test, the shaker excites the structure over a prescribed frequency range; the resulting motion is measured simultaneously at the base (input acceleration) and at the top corner of the payload (output acceleration). Two B&K Type 4506 accelerometers are used for this purpose, with the relevant in-plane acceleration channels recorded through the cDAQ acquisition system and transferred to the computer for post-processing. During data acquisition, accelerometer sensitivities are registered so that the final signals are stored in units of g. Data are then sampled continuously at a predefined rate.

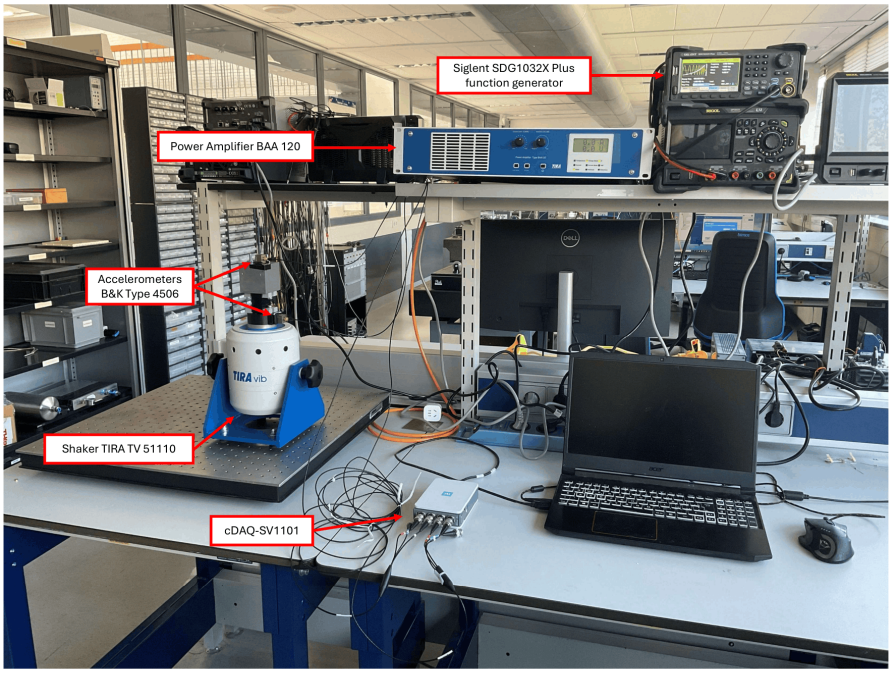


Figure 4.6: Experimental setup used in the laboratory.

Horizontal setup In Section 4.1.1 we discussed the modeling of two different setups: vertical and horizontal. In the vertical configuration, the shaker motion is aligned with the vertical direction of the isolator. For the horizontal configuration, the assembly is rotated so that the same shaker excites the horizontal direction. Because this arrangement places the payload away from the shaker symmetry axis, a counterweight is mounted on the opposite side of the fixture to approximately balance the total mass and reduce parasitic moments that could ruin the shaker, as shown in Figure 4.7. Because of gravity, the static moment created by the payload on the isolator remains during testing, although this force is simplified in the frequency domain and not taken into account in numerical models.

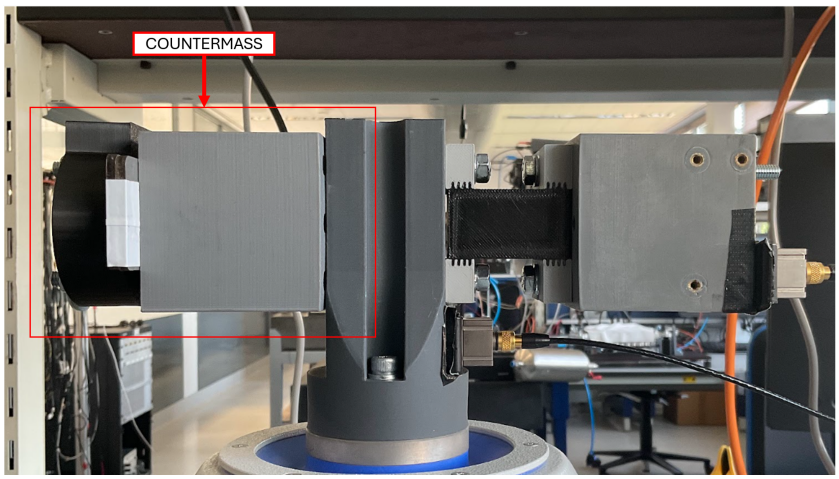


Figure 4.7: Counterweight in horizontal setup.

As an additional comparison, a lower-cost acquisition system based on two ADXL345 accelerometers and a Raspberry Pi Pico H was tested. Since this setup was used only as a supplementary measurement system, its implementation and plot results are provided in Appendix C.

4.3.1. Signal processing and model identification

To characterize the isolator over the complete frequency range of interest, the shaker is driven using a logarithmic sinusoidal frequency sweep. Compared with broadband random excitation, a sweep was chosen because it provided a better and clearer response over the targeted frequency range.

The excitation frequency increases from f_0 to f_1 over a sweep duration T_{sw}. For a logarithmic sweep, the instantaneous frequency and phase are

$$f(\tau) = f_0 e^{\beta\tau}, \qquad \phi(\tau) = 2\pi \frac{f_0}{\beta}\left(e^{\beta\tau} - 1\right), \qquad \beta = \frac{\ln(f_1/f_0)}{T_{\mathrm{sw}}}, \tag{4.1}$$

where τ is the elapsed time from the start of the sweep. The exponential frequency law assigns approximately equal measurement time to equal logarithmic frequency intervals.

During post-processing the frequency range is divided into equal logarithmically spaced evaluation points. For each frequency f_k, the logarithmic sweep law is inverted to determine the corresponding time at which that frequency was applied. A local time window is then placed around this point. Its duration is selected adaptively so that enough oscillation cycles are included while the frequency variation inside the window remains limited. For the nature of a logarithmic sweep, more cycles are retained at low frequencies, while shorter windows are used at high frequencies. Windows containing fewer than three complete cycles are rejected.

Within each local window, the mean value is removed and a Hann window is applied to reduce discontinuities at the edges of the segment (Harris 1978). The Hann window has no fixed length, but spans the complete local segment selected for each frequency. In the present implementation, this segment is chosen to contain approximately 20 oscillation cycles at the low frequency end, gradually decreasing to 8 cycles at the highest frequency. Its duration is also limited so that the excitation frequency does not vary by more than $3\ \mathrm{Hz}$ within the segment. Windows containing fewer than three complete cycles are discarded.

The local complex acceleration amplitude is then estimated by comparing the measured signal with the phase of the logarithmic sweep (Müller and Massarani 2001). This operation isolates the signal response at each frequency and provides the corresponding amplitude and phase. The procedure is applied identically to the two input and output accelerometers. For an excited direction j, the experimentally identified transmissibility is

$$|T_{ij}(f_k)| = \frac{|\hat{a}_i(f_k)|}{|\hat{a}_{b,j}(f_k)|}, \qquad \varphi_{ij}(f_k) = \arg[T_{ij}(f_k)]\,, \tag{4.2}$$

for each frequency f_k. In this work, only horizontal and vertical in-plane translations are applied at the base and measured at the payload. Therefore, we consider relevant only the second order principal submatrix

$$\mathbf{T}(\omega) = \begin{bmatrix} T_{\mathrm{xx}}(\omega) & T_{\mathrm{xy}}(\omega) \\ T_{\mathrm{yx}}(\omega) & T_{\mathrm{yy}}(\omega) \end{bmatrix}. \tag{4.3}$$

The vertical configuration therefore provides the direct transmissibility T_{yy} and the cross-coupled response T_{xy}, whereas the horizontal configuration provides T_{xx} and T_{yx}. The cross-transmissibility plots will be of less importance for the identification of the main resonances and related damping. The accelerometer channels and their signs are reassigned during post-processing according to the orientation of each sensor in the two test configurations.

The quality of each input-output estimate is evaluated using the coherence

$$\gamma_{ij}^2(f) = \frac{\left|S_{a_{b,j}a_i}(f)\right|^2}{S_{a_{b,j}a_{b,j}}(f)S_{a_ia_i}(f)}, \qquad 0 \leq \gamma_{ij}^2 \leq 1, \tag{4.4}$$

where $S_{a_{b,j}a_i}$ is the cross-power spectral density and the denominator contains the corresponding auto-power spectral densities. The coherence is calculated locally using Welch averaging (Welch 1967) over the same part of the sweep. Values close to one indicate that the payload response is strongly related to the measured base excitation, whereas low values can indicate noise, insufficient excitation or unmeasured disturbances.

5

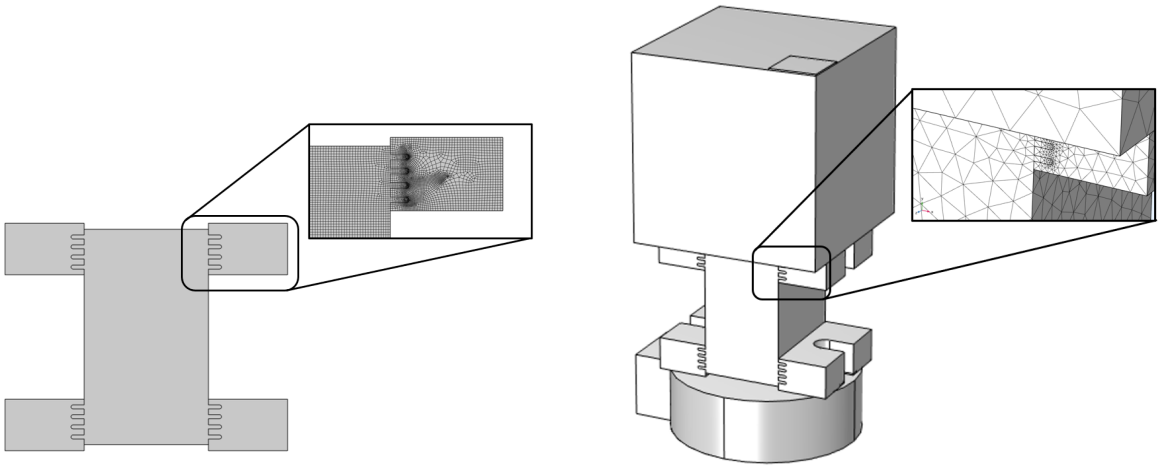
Results

This chapter presents the numerical and experimental results for the developed vibration isolator framework in terms of eigenfrequencies, relative Q factors and transmissibility. First, a TPU-only base case is used to compare the Python model with COMSOL 2D, COMSOL 3D and experimental measurements. Three optimized cases with different damping objectives are then evaluated using the same procedure. The main goal here is to assess the accuracy of the predictions obtained with the improved analytical framework. Additionally, numerical examples are explored to investigate the influence of frequency dependence in material properties, an alternative material combination and its effect on designs, the addition of an upper eigenfrequency constraint and finally stress results.

5.1. Base case

A preliminary base case is defined where the whole domain consists of viscoelastic material, in our case characterized as TPU. Interlocking features are present on all the boundaries where TPU connects with PLA and added in post-process in the COMSOL 2D and 3D simulated systems (visible in Figure 5.1 with a view of their corresponding meshes). All the components are represented utilizing the same material properties of TPU and PLA defined in the framework. The 2D COMSOL model follows the same dimensions shown in Figure 4.1 and represents the payload through the corresponding rigid connector formulation, using boundary conditions consistent with the Python framework. The COMSOL 3D model instead includes the extruded isolator and the relevant assembly geometry. The same approach will be used to compare the results of the topology optimized designs in subsequent results.

The mesh utilized for the 2D model is composed of linear quadrilateral elements with the same maximum size of the framework domain, though smaller elements form near inner boundaries and small features. For the 3D model, a physics-controlled mesh composed of triangular and tetrahedral elements is defined, with element size set to ”normal” in COMSOL. This difference introduces an additional discretization difference between the models as different sizes and shapes are adopted, with the advantage of faster simulations.

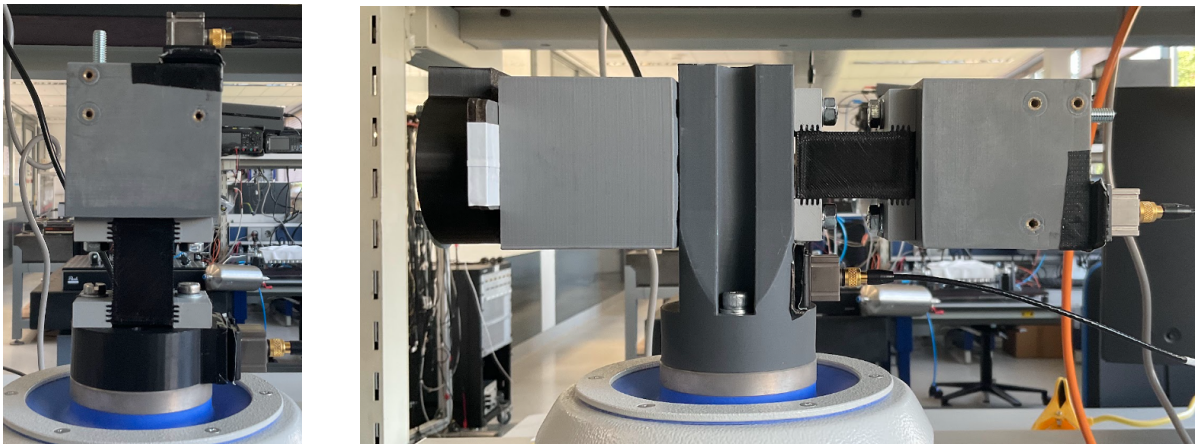


(a) 2D CAD model used in COMSOL

(b) 3D CAD model used in COMSOL

Figure 5.1: COMSOL 2D and 3D models of the base-case assembly.

Both vertical and horizontal setups built in the laboratory can be seen in Figure 5.2, attached to the shaker. The same configurations will be used for all the subsequent tested isolator designs and all tests are conducted at around $25°C$.



(a) Vertical experimental setup

(b) Horizontal experimental setup

Figure 5.2: Experimental setups for vertical and horizontal shaker excitation.

To visualize the deformation mechanisms associated with the three rigid-body-dominated modes, Figure 5.3 shows the deformed isolator together with the corresponding imaginary part of shear strain energy distribution. The latter field indicates qualitatively where the dissipative energy that creates damping is located in the domain.

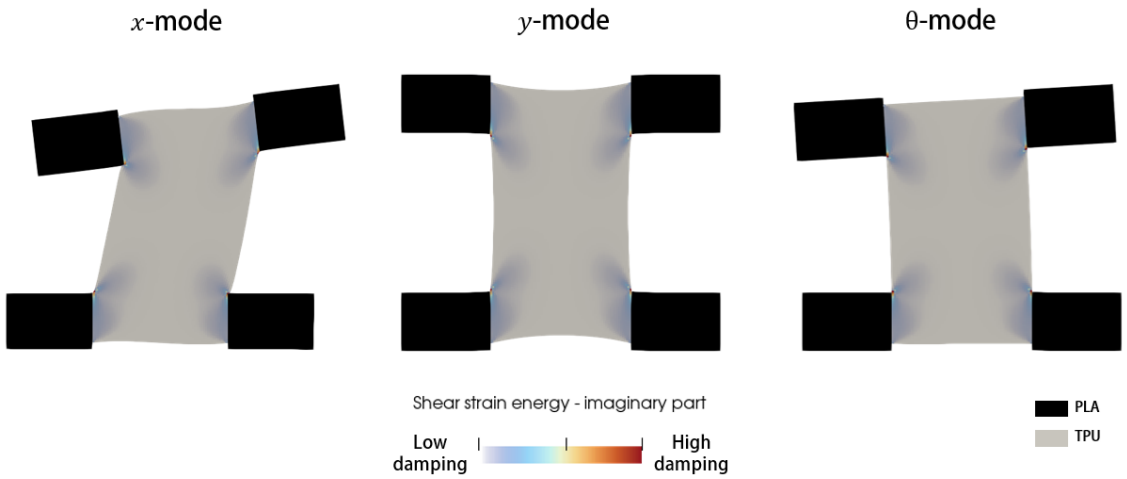
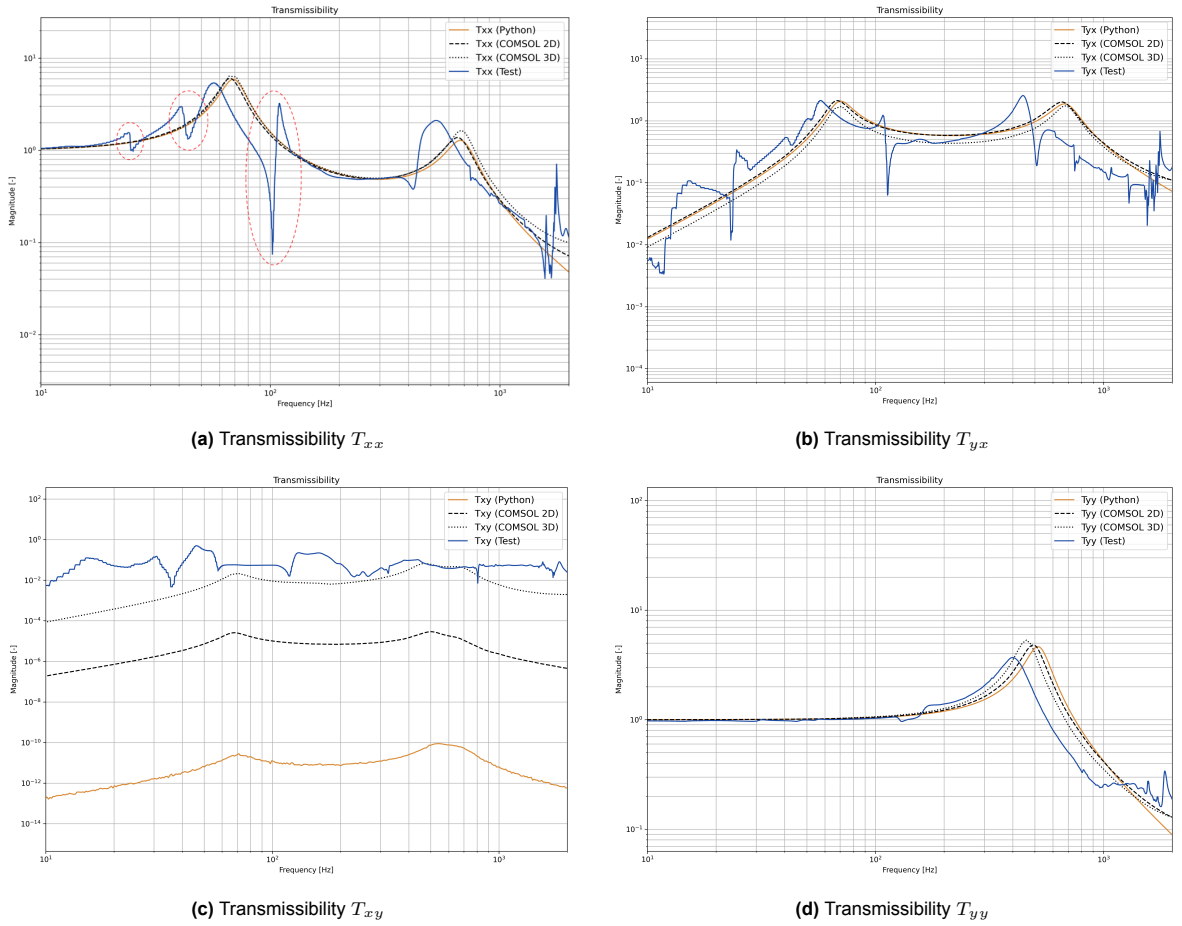


Figure 5.3: Deformed shapes and shear strain energy distributions (imaginary part) for the base case isolator in the x-, y- and θ-modes.

Direct-transmissibilities T_{xx},T_{yy} and cross-transmissibilities T_{yx},T_{xy} are calculated in the framework, calculated in COMSOL for both the 2D and 3D configuration and lastly obtained from the accelerometer signals through model identification. All four cases are then compared and the resulting plots can be seen here below in Figure 5.4.

The relevant frequency range goes from 10 Hz to 2000 Hz, although various spikes and noisy data can be identified from 1 Hz to 10 Hz and at higher frequencies for the test results. The full extended plots are visible in Appendix D for all the cases discussed in this chapter, together with the associated phase and coherence.



(a) Transmissibility T_{xx}

(b) Transmissibility T_{yx}

(c) Transmissibility T_{xy}

(d) Transmissibility T_{yy}

Figure 5.4: Transmissibility comparisons for in-plane directions x and y

The y-mode resonance can be clearly identified in T_{yy}, while first the θ-mode and later the x-mode resonances are visible in the T_{xx} plot. In the latter, additional resonances (highlighted in Figure 5.4a) can be recognized: at 24 Hz and 42 Hz a pole-zero pair is present, while at around 105 Hz there is a zero-pole pair of higher magnitude. These additional features are likely associated with extra coupled dynamics of the complete experimental assembly that are not represented by the reduced 3-DOF model. The finite stiffness of the shaker and fixtures, bolt and interface compliance, the counterweight assembly, and local deformation of the payload and isolator can introduce additional modes. Their interaction at the selected excitation and measurement locations can also generate anti-resonances through modal cancellation.

In T_{yy}, the mass line of the test curve broadly decays with the same slope as the analytical and COMSOL simulated models. While looking at T_{xx}, the experimental test decays slower.

In general, the experimentally measured cross-transmissibilities contain more noise as the cross-axis response is smaller than the direct response. For T_{xy}, large differences in magnitude are observed between the four analyzed cases. For a symmetric 2D geometry like in this case, vertical base excitation should produce almost no horizontal payload motion. Consequently, T_{xy} becomes highly sensitive to any asymmetry perturbation. In the 2D COMSOL model, this difference is caused mainly by finite precision arithmetic artifacts that introduce tiny non-zero values into off-diagonal terms. In the 3D COMSOL model, the additional jump in magnitude is attributable to the probe pad placed off-center on top of the payload (visible in Figure 5.1b) to emulate sensor placement. In the experiment, added couplings may be caused by misalignment while assembling the setup onto the shaker.

T_{yx} instead has a better match also across the numerical cases, as there is a more prominent coupling happening with an horizontal base excitation that is captured also numerically by the output position

of the payload. Most notably, an extra pole-zero pair here can be identified around 110 Hz during experimental testing.

Step-like segments are visible mainly in the cross-transmissibilities in the experimental curves at low frequency. This is most probably attributed to the frequency sweep identification method rather than to additional structural modes. In post-processing, the response assumes an ideal logarithmic sweep with a prescribed start time and analytical phase, whereas the signal generator and NI-DAQ are not hardware synchronized. Small differences between the actual and assumed sweep progression therefore appear, particularly at low frequencies where longer analysis windows are required.

Since T_{yx} and T_{xy} present less relevant data, only the direct transmissibilities will be analyzed for topology optimized designs, while the complete results are reported in Appendix D.

Using the half-power bandwidth method (Papagiannopoulos and Hatzigeorgiou 2011), we can approximately measure and extract from the test plots the Q factor associated with each rigid-body mode. In the COMSOL simulated models, the Q factor is measured with the same analytical formula used in the framework, knowing the respective complex eigenfrequency. This allows us to compare overall the obtained eigenfrequencies and Q factor numerically across the four cases. Figure 5.5 presents these data, where COMSOL and test results are compared individually to the initial framework predictions.

Eigenfrequency comparison

	Python	COMSOL 2D	Error %	COMSOL 3D	Error %	Test	Error %
Mode x	680,66	658,60	3,35%	681,63	0,14%	525,00	29,65%
Mode y	519,26	494,18	5,08%	461,63	12,48%	400,00	29,82%
Mode θ	69,00	66,76	3,36%	68,71	0,42%	56,00	23,21%

Damping comparison (Q factor)

	Python	COMSOL 2D	Error %	COMSOL 3D	Error %	Test	Error %
Mode x	4,07	4,13	1,24%	4,80	15,04%	3,85	5,94%
Mode y	4,62	4,64	0,56%	5,03	8,24%	3,47	33,14%
Mode θ	4,52	4,59	1,60%	5,45	17,07%	4,78	5,52%

Figure 5.5: Table comparing eigenfrequencies and associated Q factor of Python framework with COMSOL 2D, COMSOL 3D and tested results.

The best match happens between the framework and the COMSOL 2D model, as expected. Moving to 3D, COMSOL captures the horizontal and rotational modes relatively well, while showing larger deviations for the vertical mode and its associated Q factor. In the worst case, test results deviate by around 30% from framework predictions. Since this base case consists of a homogeneous TPU isolator with a simpler geometry, it provides a reference for the following optimized designs. In those cases, more complex geometries are expected to introduce additional sources of discrepancy.

5.2. Optimized designs

Topology optimization is performed for three different objective cases depending on the imposed objective: x-mode damping (minimize Q_{x}), y-mode damping (minimize Q_{y}) and lastly multi-mode damping (minimize J_{Q}). The topology optimization settings utilized in all three cases can be seen in Table 5.1. Additionally, the prescribed base acceleration used for stress evaluation was selected according to each optimization case: $a_x = 5g$ for the x-mode design, $a_y = 5g$ for the y-mode design, and both $a_x = a_y = 5g$ for the multi-mode design.

Table 5.1: Topology optimization settings.

Parameter	Value
Filter radius	7
SIMP penalization factor p	3.5
Maximum iterations	100
Heaviside threshold η	0.7
Heaviside parameter β	$[1; 30]$

Different variations were created by sweeping the active constraint parameter related to the minimum eigenfrequency, starting from 50 Hz all the way to 230 Hz. Plotting the resulting Q factor objective against the minimum eigenfrequency constraint produces a Pareto front that shows the trade-off between stiffness and damping .

The isolator must provide high damping while maintaining sufficient stiffness. To identify the best compromise between these conflicting criteria, the eigenfrequency and Q factor ranges considered (50 Hz to 230 Hz and 4 to 20, respectively) are first normalized between 0 and 1. The Euclidean distance of each design from the ideal (or Utopia) point is then calculated, and the design with the smallest distance is selected as the optimal solution. Figure 5.6 shows the optimal design obtained for each analyzed case, which will be then selected to be tested in the laboratory and analyzed across the different numerical models.

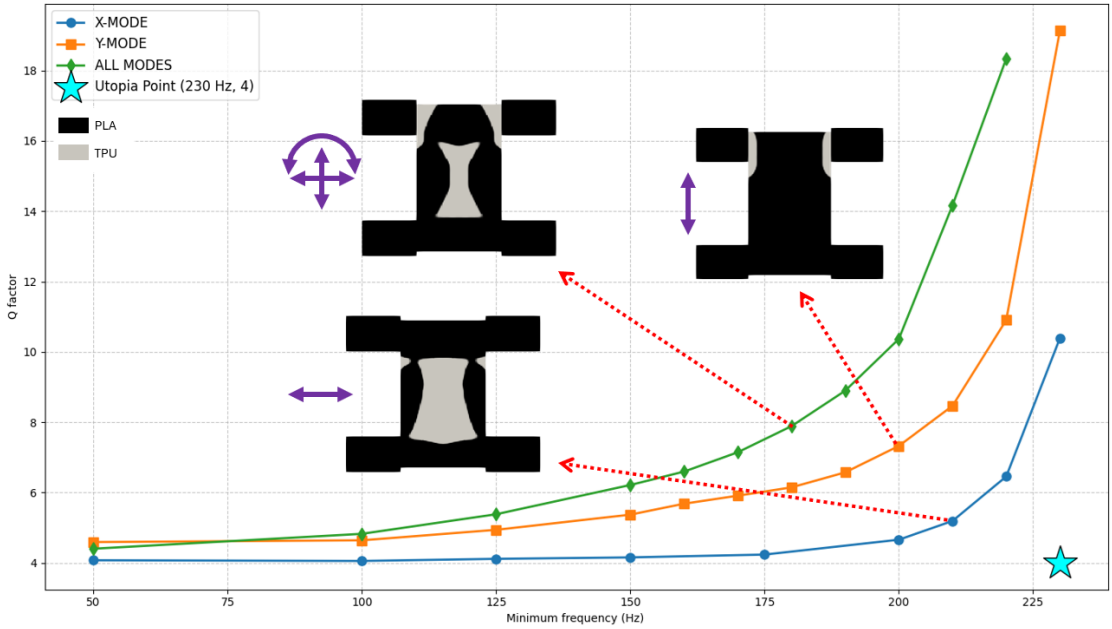


Figure 5.6: Pareto fronts and selected trade-off designs for the x-, y- and multi-mode optimization cases.

5.2.1. x-mode damping

Starting from the optimized isolator design for x-mode damping, the same approach as the base case presented in Section 5.1 was used to analyze the results. Figure 5.7 shows the excited isolator deformed at its three rigid-body modes together with the corresponding imaginary part of shear strain energy distribution.

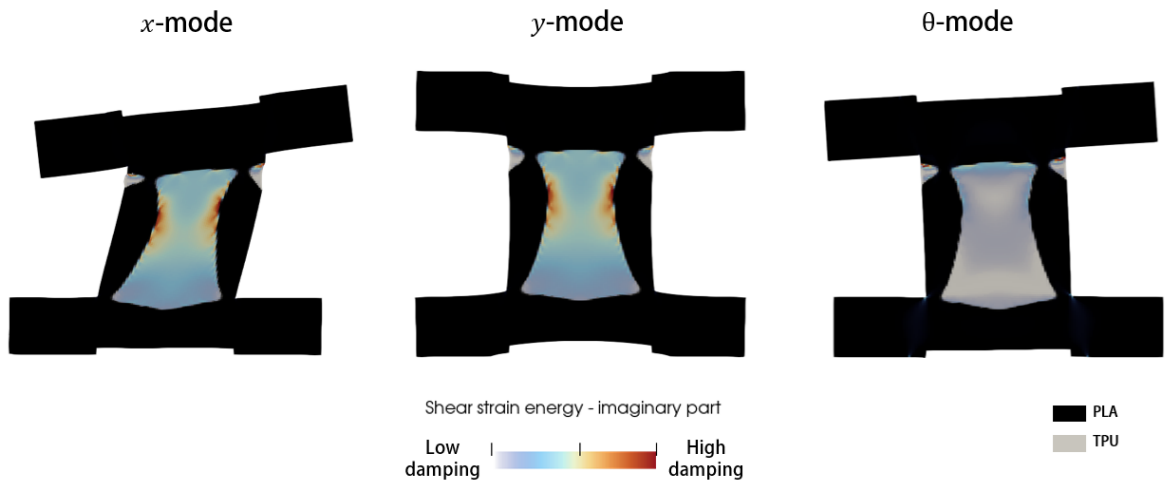
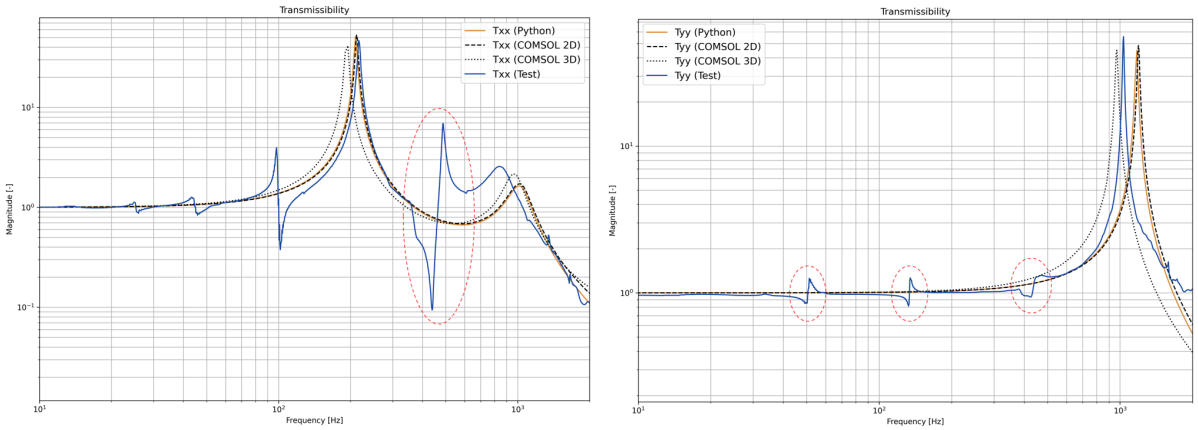


Figure 5.7: Deformed shapes and shear strain energy distributions (imaginary part) for the x-mode damped isolator in the x-, y- and θ-modes.

The obtained direct transmissibilities T_{xx} and T_{yy} of the optimized design can be seen in Figures 5.8a and 5.8b, respectively.



(a) Transmissibility T_{xx}

(b) Transmissibility T_{yy}

Figure 5.8: Direct transmissibility comparison for the x-mode damped isolator.

As highlighted in the plots, the experimental vibration measurements reveal additional extra resonances not captured by the numerical models. T_{xx} obtained through testing presents the same extra resonances observed in the base case design (Section 5.1), with an extra zero-pole pair present at around 460 Hz. The T_{yy} measured presents instead three minor zero-pole pairs at around 40 Hz, 140 Hz and 460 Hz; it is uncelar if the latter derives from the same parasitic dynamics that create the extra resonance in T_{xx}.

Eigenfrequencies and Q factors are similarly compared in Figure 5.9.

Eigenfrequency comparison							
	Python	**COMSOL 2D**	Error %	**COMSOL 3D**	Error %	**Test**	Error %
Mode x	1021,87	1025,60	0,36%	973,80	4,94%	840,00	21,65%
Mode y	1171,45	1192,50	1,77%	968,32	20,98%	1030,00	13,73%
Mode θ	210,00	212,38	1,12%	192,88	8,88%	217,00	3,23%

Damping comparison (Q factor)							
	Python	**COMSOL 2D**	Error %	**COMSOL 3D**	Error %	**Test**	Error %
Mode x	5,19	5,10	1,77%	6,01	13,60%	4,00	29,80%
Mode y	45,30	46,69	2,98%	42,62	6,29%	61,08	25,83%
Mode θ	38,75	40,69	4,77%	43,25	10,41%	38,38	0,96%

Figure 5.9: Table comparing eigenfrequencies and associated Q factor of Python framework with COMSOL 2D, COMSOL 3D and tested results.

The rotational mode demonstrates high accuracy throughout the transmissibility curve and numerical values. The horizontal mode appears to have the highest discrepancy, overestimating both the resonance frequency by 21% and Q factor by 30%.

Both the y- and rotational modes are weakly damped and are expected to store a larger fraction of their strain energy in the stiff PLA phase. Their response may therefore be less sensitive to uncertainties in the frequency-dependent TPU properties. In the vibration test a higher peak is registered in the y-mode, while the rotational mode is well captured. The 3D COMSOL simulated model seems to underestimate the eigenfrequency in the y-mode by 20%, which relates to the effective vertical stiffness calculated.

Despite the deviations, the intended modal damping selectivity is reproduced experimentally ($Q_x \approx 4$ in the test result), confirming that the topology introduces damping into the targeted mode.

5.2.2. y-mode damping

The same approach is used for the y-mode damped isolator. Like before, Figure 5.10 shows the excited isolator deformed at its three rigid-body modes together with the corresponding imaginary part of shear strain energy distribution.

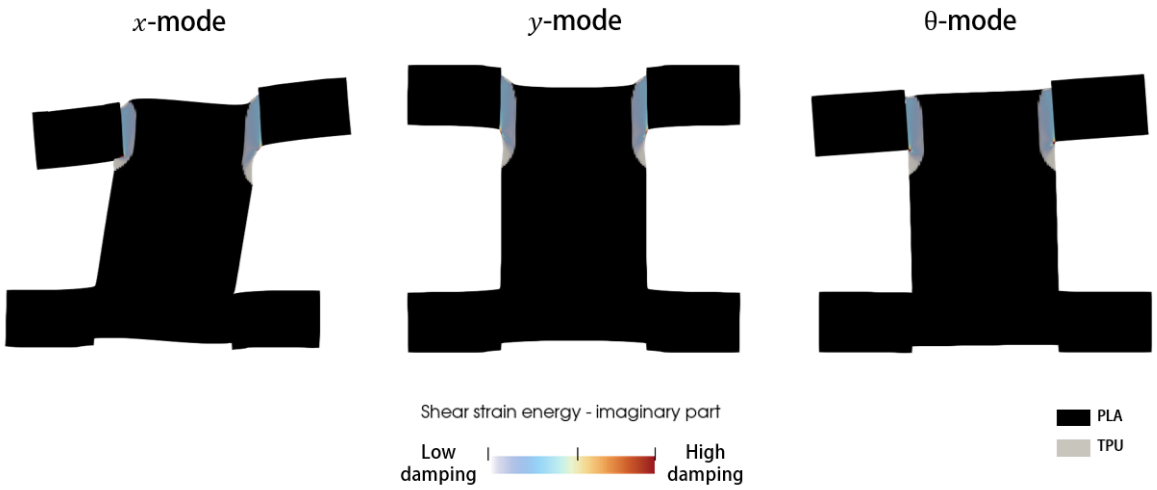
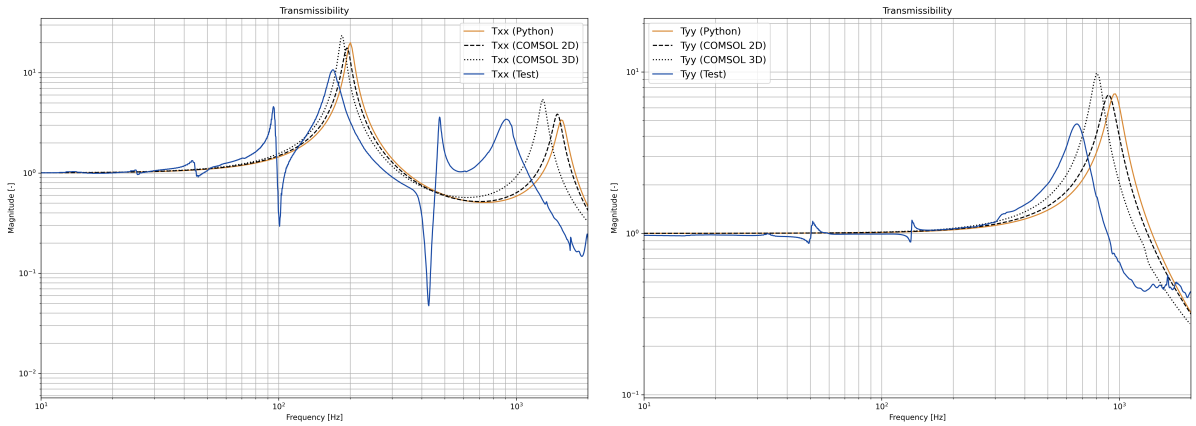


Figure 5.10: Deformed shapes and shear strain energy distributions (imaginary part) for the y-mode damped isolator in the x-, y- and θ-modes.

The obtained direct transmissibilities T_{xx} and T_{yy} of the optimized design can be seen in Figures 5.11a and 5.11b, respectively.



(a) Transmissibility T_{xx}

(b) Transmissibility T_{yy}

Figure 5.11: Direct transmissibility comparison for the y-mode damped isolator.

Eigenfrequencies and Q factors are compared in Figure 5.12.

Eigenfrequency comparison							
	Python	**COMSOL 2D**	Error %	**COMSOL 3D**	Error %	**Test**	Error %
Mode x	1554,54	1489,50	4,37%	1293,40	20,19%	910,00	70,83%
Mode y	958,19	902,75	6,14%	807,37	18,68%	662,00	44,74%
Mode θ	200,00	193,91	3,14%	185,72	7,69%	169,00	18,34%

Damping comparison (Q factor)							
	Python	**COMSOL 2D**	Error %	**COMSOL 3D**	Error %	**Test**	Error %
Mode x	11,07	11,80	6,21%	14,86	25,54%	6,67	65,98%
Mode y	7,33	6,98	4,93%	9,45	22,44%	5,28	38,64%
Mode θ	15,35	13,51	13,56%	19,60	21,69%	9,03	69,88%

Figure 5.12: Table comparing eigenfrequencies and associated Q factor of Python framework with COMSOL 2D, COMSOL 3D and tested results.

Experimental results for this configuration exhibit the largest discrepancies among all tested isolators, with resonant peaks appearing up to 70% more damped than predicted. Additionally, rigid-body modes shift to lower frequencies than anticipated, reaching a maximum relative error of 70% in the horizontal mode.

A possible contributor to the large discrepancy in x-mode could be the additional compliance at the PLA-TPU interfaces. Imperfect bonding, local gaps or manufacturing defects could have reduced the effective stiffness of these regions, although this mechanism was not isolated experimentally. In contrast, the effect of interlocking features remains secondary, as their inclusion in the 2D COMSOL model maintains strong agreement with the analytical framework.

The COMSOL 3D model generally underestimates damping, resulting in higher Q factors than both framework and test data. This may result from deformations redistributing a smaller fraction of the total modal strain energy into the dissipative shear deformation of TPU. However, the COMSOL 3D predictions are closer to the experimentally measured eigenfrequencies.

Notably, the intended damping objective set by the topology optimization framework remains present experimentally, with the y-mode retaining the lowest measured Q factor.

5.2.3. Multi-mode damping

Lastly, the multi-mode damped isolator is analyzed. Figure 5.13 shows the excited isolator deformed at its three rigid-body modes together with the corresponding imaginary part of shear strain energy

distribution.

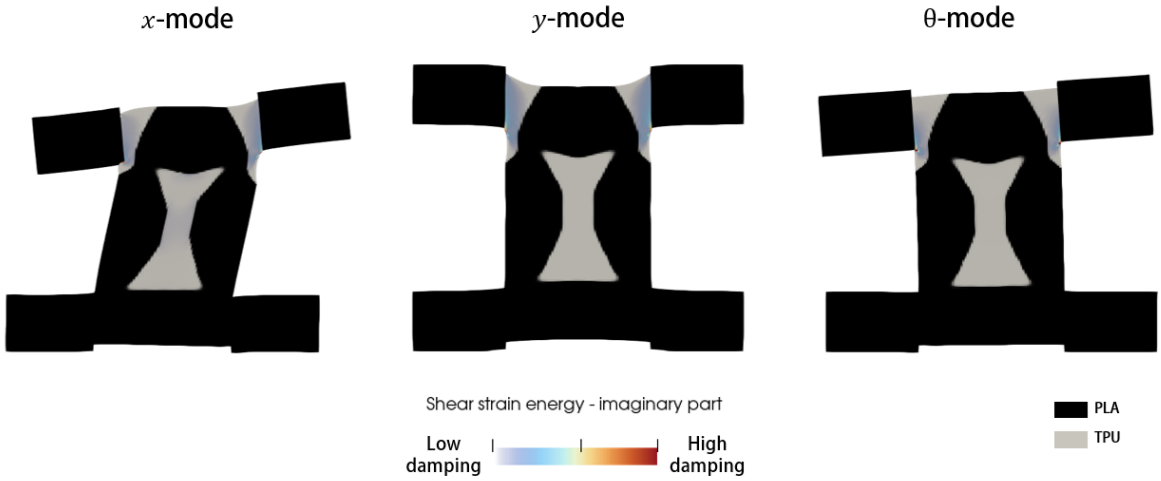
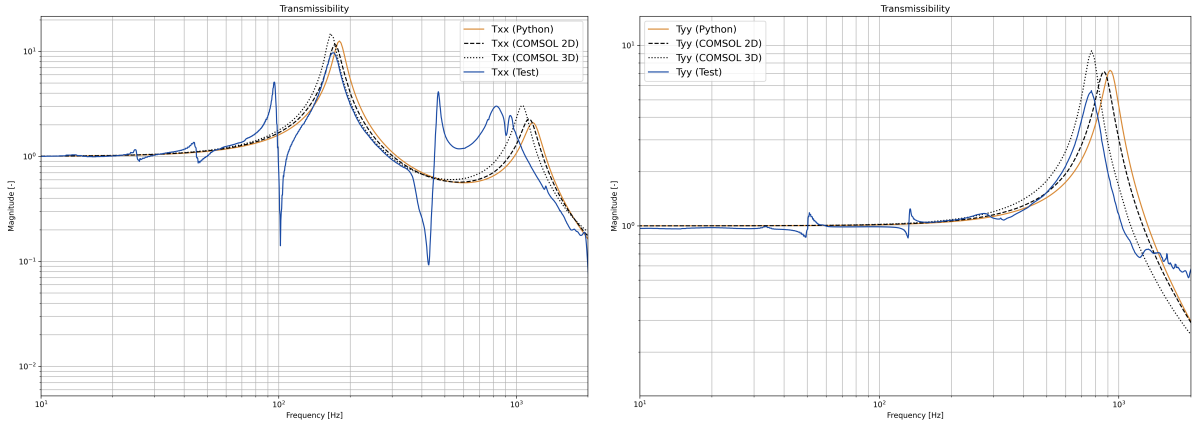


Figure 5.13: Deformed shapes and shear strain energy distributions (imaginary part) for the multi-mode damped isolator in the x-, y- and θ-modes.

The obtained direct transmissibilities T_{xx} and T_{yy} of the optimized design can be seen in Figures 5.14a and 5.14b, respectively.



(a) Transmissibility T_{xx}

(b) Transmissibility T_{yy}

Figure 5.14: Direct transmissibility comparison for the multi-mode damped isolator.

Right at the x-mode resonance in T_{xx}, a small anti-resonance is visible around 900 Hz. Eigenfrequencies and Q factors are compared in Figure 5.15.

Eigenfrequency comparison							
	Python	**COMSOL 2D**	Error %	**COMSOL 3D**	Error %	**Test**	Error %
Mode x	1173,33	1133,70	3,50%	1054,50	11,27%	850,00	38,04%
Mode y	923,72	867,78	6,45%	768,92	20,13%	765,00	20,75%
Mode θ	180,00	172,67	4,25%	165,58	8,71%	170,00	5,88%

Damping comparison (Q factor)							
	Python	**COMSOL 2D**	Error %	**COMSOL 3D**	Error %	**Test**	Error %
Mode x	6,77	6,93	2,40%	8,43	19,70%	5,72	18,32%
Mode y	7,28	6,94	4,77%	8,86	17,89%	6,40	13,68%
Mode θ	9,63	8,86	8,67%	11,31	14,84%	8,15	18,14%

Figure 5.15: Table comparing eigenfrequencies and associated Q factor of Python framework with COMSOL 2D, COMSOL 3D and tested results.

Damping here shows the best agreement, with an observed Q factor in the experiments differing by at most 18% compared to the initial framework calculations. Damping also remains balanced across all three modes, as the Q factor in the test never exceeds 10, consistently with the P-mean objective used during optimization. COMSOL 3D again predicts generally higher Q factors and less damped resonances than the framework. The rotational mode demonstrates again a good accuracy throughout the transmissibility curve and numerical values.

Importantly, the modal ordering and relative damping behavior remained consistent across all three optimized designs. This provides additional evidence that the framework accurately captures the primary structural dynamics of rigid-body modes in the isolators.

5.3. Further exploration of numerical results

The following studies investigate how topology optimization settings and assumptions influence the numerical solutions independently of the experimental comparison. In particular, the effects of frequency-dependent material properties, the use of alternative material properties, the addition of an upper eigenfrequency constraint and the stress formulation are examined.

5.3.1. Influence of frequency-dependent material properties

Frequency dependence is important to capture in a viscoelastic material, although it is interesting to evaluate how strongly this assumption influences the optimized response compared to a topology optimization algorithm where the shear modulus is set as a constant value.

A constant shear modulus is selected from the master curve at 500 Hz, the topology optimization algorithm is then carried out without any inner loop, but with the same settings. Figure 5.16 shows the difference in the designs and Figure 5.17 presents the resulting complex eigenfrequencies from each case, comparing the new results with previous frequency-dependent results.

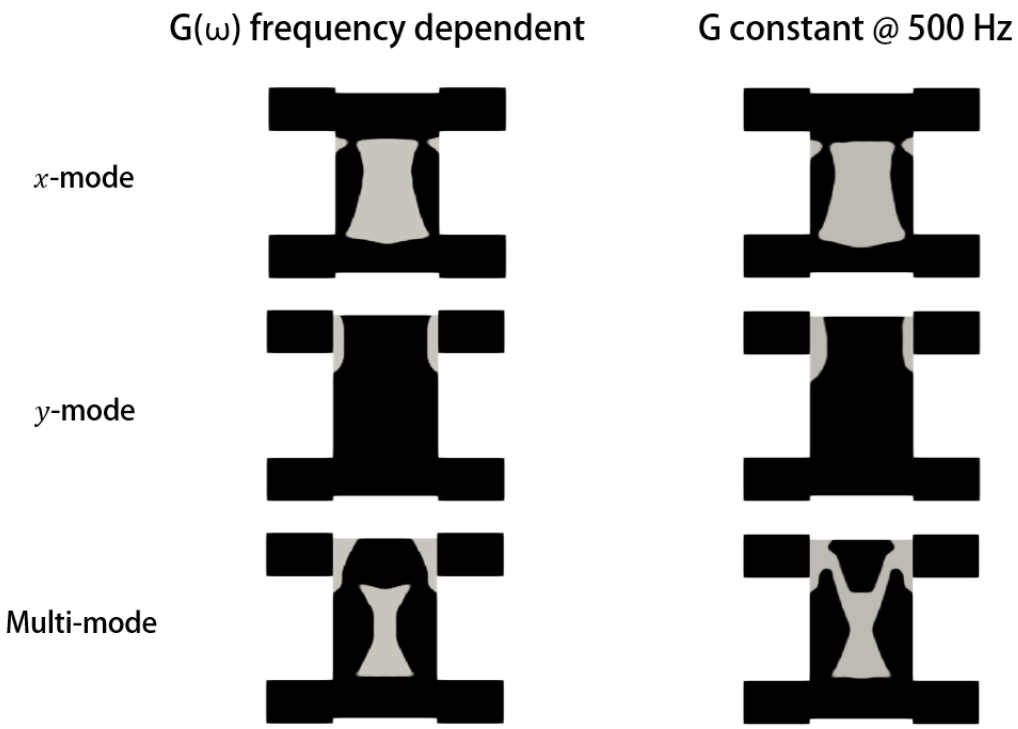


Figure 5.16: Design comparison between the topology optimization with and without frequency dependence.

X-mode (eigenfrequencies)			
	G frequency-dependent	G constant	Error %
Mode x	1021,87	930,21	9,85%
Mode y	1171,45	1164,03	0,64%
Mode θ	210,00	210,00	0,00%

X-mode (Q factors)			
	G frequency-dependent	G constant	Error %
Mode x	5,19	4,81	7,94%
Mode y	45,30	39,14	15,73%
Mode θ	38,75	33,55	15,49%

Y-mode (eigenfrequencies)			
	G frequency-dependent	G constant	Error %
Mode x	1554,54	1502,93	3,43%
Mode y	958,19	906,96	5,65%
Mode θ	200,00	200,01	0,00%

Y-mode (Q factors)			
	G frequency-dependent	G constant	Error %
Mode x	11,07	10,38	6,61%
Mode y	7,33	6,48	13,05%
Mode θ	15,35	12,86	19,29%

Multi-mode (eigenfrequencies)			
	G frequency-dependent	G constant	Error %
Mode x	1173,33	1081,69	8,47%
Mode y	923,72	897,03	2,98%
Mode θ	180,00	180,01	0,01%

Multi-mode (Q factors)			
	G frequency-dependent	G constant	Error %
Mode x	6,77	5,92	14,28%
Mode y	7,28	6,87	5,95%
Mode θ	9,63	8,65	11,28%

Figure 5.17: Comparison of eigenfrequencies and Q factors obtained with frequency-dependent and constant shear modulus.

The inclusion of frequency-dependent material properties is proven to be relevant and valuable as using a constant shear modulus changes eigenfrequencies and Q factor values up to 10% and 20% variations, respectively. Nevertheless, if reducing computation time is the priority and this deviation is considered acceptable, omitting frequency-dependent properties remains a viable approach. It is important to note that the farther the eigenfrequencies are from the reference conditions, the higher the mismatch, depending also on the shape of the master curve.

In Figure 5.16, change in the final topologies can be observed: x- and y-mode damped cases interestingly produce more asymmetric features while the multi-mode case changes the viscoelastic path

inside the domain. Because a constant shear modulus is being used, the framework now assigns the same material state to all eigenfrequencies. This changes both the modal damping and stiffness sensitivities and therefore it could modify the preferred location of the two materials. This effect altered the optimization convergence most noticeably in the multi-mode case.

5.3.2. Influence of material selection

Another interesting case can be studied by substituting the current analyzed materials used for testing with alternative engineering materials instead. For example we can utilize aluminium as stiff material, while the viscoelastic material can be represented by SCVBR® elastomer supplied by ERIKS, with the related master curves. Limit stresses are updated accordingly, in this case to $230\ \mathrm{MPa}$ yield stress for aluminium and $5\ \mathrm{MPa}$ allowable stress for the elastomer.

The larger stiffness contrast between the two materials can make the optimization more sensitive to changes in the material distribution. More ”relaxed” settings for topology optimization are therefore used (visible in Table 5.2). This helps improve the robustness and the numerical stability during the topology optimization.

Table 5.2: Topology optimization settings.

Parameter	Value
Filter radius	5
SIMP penalization factor p	3
Maximum iterations	150
Heaviside threshold η	0.5
Heaviside parameter β	$[1; 10]$

By applying both a_x and a_y, a diagonal base excitation is created rather than two independent loading directions. The horizontal acceleration a_x also introduces a rotational moment through the offset payload centre of mass (see Equation 2.47) and this combined loading can disrupt the symmetry of the problem. This effect can become more pronounced in this case due to contrast between limit stresses of the materials, causing the stress constraint to have a stronger influence on the material distribution and promoting asymmetric and less stable designs. Therefore, for the multi-mode case, the stress evaluation was restricted to vertical loading only $a_y = 5g$, while $a_x = 0$.

By analyzing the same cases studied for the experiments, we can obtain a similar Pareto front (visible in Figure 5.18), where again we can select the designs offering the best trade-off. Higher frequency limits are reached with a total range that goes from $27\ \mathrm{Hz}$ to $1200\ \mathrm{Hz}$, depending on the quantity of viscoelastic material present in the designs. The Q factor range used to find the best trade-off results remains 1 to 20.

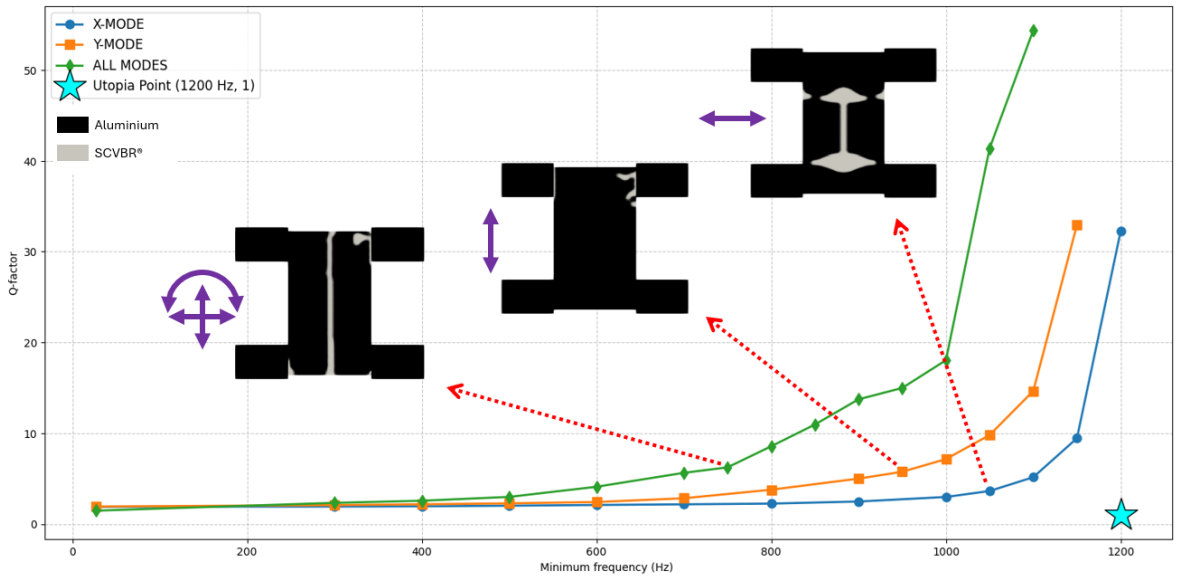


Figure 5.18: Pareto fronts for the x-, y- and multi-mode cases using aluminium and SCVBR®.

To see the isolator designs visible in Figure 5.18 deformed at all three resonances, with associated strain energy dissipation, see Appendix B.

More asymmetric designs are generated at higher eigenfrequency limits, particularly for the y-mode and multi-mode cases. Under these conditions, the optimizer tends to create very narrow and irregular features, which reduce the practical manufacturability of the layouts. As the minimum eigenfrequency constraint is relaxed, the designs can become more symmetric and structurally simpler, as shown in Figure 5.19. For the two alternative designs presented here, the lower eigenfrequency limit was reduced by 50 Hz compared with the previously selected solutions in the trade-off. However, some narrow features remain and they could still be difficult to reproduce accurately in practice.

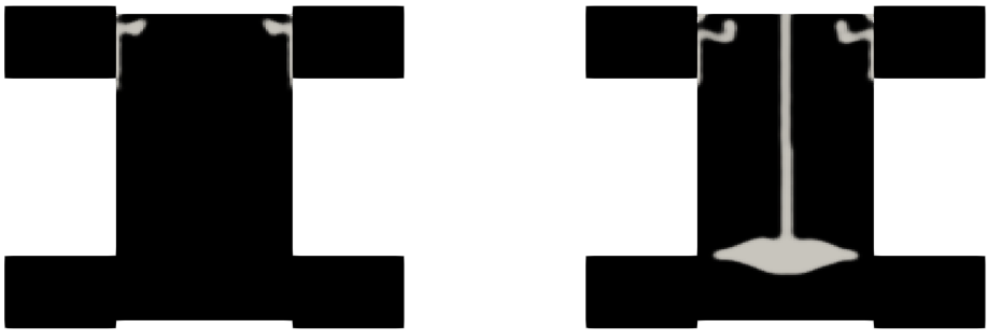


Figure 5.19: Alternative y-mode and multi-mode damped designs obtained with alternative minimum eigenfrequency constraints.

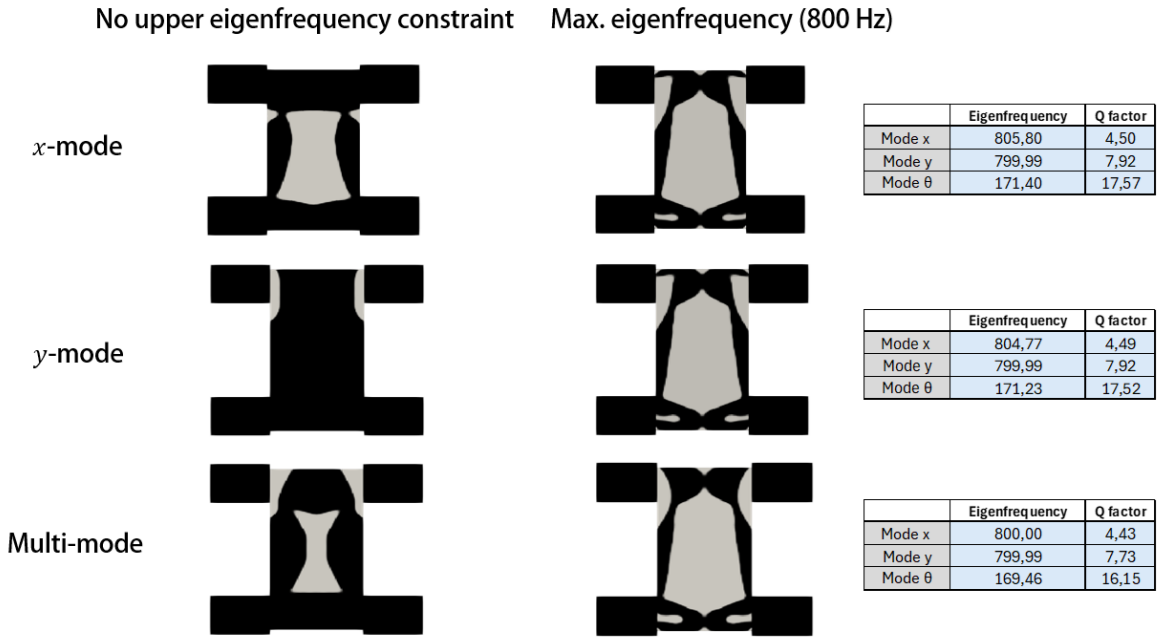
The additional study using aluminium and SCVBR® rubber shows that more effective materials increase achievable stiffness while maintaining high damping performance. The topology optimization algorithm creates thinner and more localized viscoelastic regions (see x-mode and multi-mode damped designs),

in some cases comparable to constrained-layer damping features present in aerospace structures and described in Chapter 1.

Since symmetry is not explicitly imposed in the optimization, small differences in the design can develop into asymmetric local optima. The coupling between the generalized translational and rotational motions, represented by the off-diagonal terms of the stiffness and mass matrices, may further enhance the creation of asymmetric features. In addition, some optimized designs concentrate deformation within single narrow viscoelastic regions to better satisfy the minimum eigenfrequency constraint, especially when it requires high stiffness.

5.3.3. Upper eigenfrequency constraint

To further control and optimize the dynamic response of the isolator, an upper eigenfrequency constraint of 800 Hz was introduced and compared with the previous formulation, containing only a lower frequency bound. According to the analytical framework, the base case in Section 5.1 had the highest eigenfrequency at around 680 Hz; so to leave freedom during topology optimization a slightly higher upper limit at 800 Hz was chosen in this particular case. Figure 5.20 shows the resulting designs for the x-mode, y-mode and multi-mode cases together with the corresponding obtained eigenfrequencies.



	Eigenfrequency	Q factor
Mode x	805,80	4,50
Mode y	799,99	7,92
Mode θ	171,40	17,57

	Eigenfrequency	Q factor
Mode x	804,77	4,49
Mode y	799,99	7,92
Mode θ	171,23	17,52

	Eigenfrequency	Q factor
Mode x	800,00	4,43
Mode y	799,99	7,73
Mode θ	169,46	16,15

Figure 5.20: Design comparison between test designs and updated designs when an upper limit frequency constraint is applied.

With the additional constraint, the x- and y-mode eigenfrequencies converge close to the prescribed upper limit, while the rotational mode now struggles to satisfy the lower eigenfrequency limit. Because the eigenmodes converge to similar results across the three different objective cases, the final topologies also become more similar. Small deviations from the 800 Hz limit remain in some cases due to the numerical convergence of the optimization.

When we introduce an upper eigenfrequency constraint, the feasible design space becomes more restricted. As the allowable frequency range for the rigid-body modes becomes narrower, satisfying all requirements simultaneously becomes more restrictive and the frequency constraints can increasingly dominate the final topology. This is reflected by the greater similarity between the constrained designs obtained from different objectives. The achievable damping performance can therefore also become more limited. However, only one upper frequency limit is investigated in this work, using TPU and PLA material properties. Using instead more effective materials with larger stiffness and better damping properties may provide additional design freedom, but this would require a dedicated parametric study.

5.3.4. Stress evaluation

To have an idea of how well stresses are calculated across the domain in the framework, a comparison is conducted between the analytically derived stresses and the ones simulated in COMSOL 2D for the same design. This is done for both peak stresses and aggregated stresses using the P-mean formula.

Figures 5.21 and 5.22 present the results for the x-mode and y-mode damped isolators, analyzed and presented before in this chapter.

Peak Stresses (in MPa)			
	Python	COMSOL 2D	Error %
Mode x	0,271	0,579	53,17%
Mode y	0,175	0,322	45,73%
Mode θ	42,769	55,656	23,15%

Aggregated Stresses (in MPa)			
	Python	COMSOL 2D	Error %
Mode x	0,116	0,181	35,93%
Mode y	0,073	0,098	25,83%
Mode θ	17,952	17,081	5,10%

Figure 5.21: Stress comparison for peak and aggregated stress in the x-mode optimized case

Peak Stresses (in MPa)			
	Python	COMSOL 2D	Error %
Mode x	0,181	0,268	32,37%
Mode y	2,029	2,906	30,16%
Mode θ	0,291	0,435	33,20%

Aggregated Stresses (in MPa)			
	Python	COMSOL 2D	Error %
Mode x	0,076	0,075	1,61%
Mode y	0,859	0,826	3,93%
Mode θ	0,122	0,126	2,57%

Figure 5.22: Stress comparison for peak and aggregated stress in the y-mode optimized case

The stress distributions show a dependence on the excited resonance. For the x-mode optimized design where horizontal base acceleration is applied, the rotational resonance produces by far the largest stress levels, linked with the rotational moment produced by the payload. For the y-mode optimized design, the largest stresses instead occur at the vertical resonance under vertical excitation, as expected.

Stresses obtained for the y-mode damped isolator show closer agreement, even if interlocking features are present in the COMSOL 2D model. Peak stresses differ more significantly between the Python framework and COMSOL in both cases compared to aggregated stresses.

6

Discussion

This chapter discusses the findings obtained from Chapter 5, with particular attention given to the agreement between framework, COMSOL and experimental measurements. Sources of error that could cause discrepancies are analyzed together with general trends. The influence of the optimization material properties and stress constraints is then discussed, together with the practical limitations introduced by manufacturing and the experimental setup.

6.1. Experimental validation and sources of mismatch

In general, the agreement decreases as the model becomes more representative of the physical system. The closest results are obtained between the Python framework and COMSOL 2D, while larger differences generally appear in COMSOL 3D and in the experimental measurements. This trend is visible in both the eigenfrequencies and Q factors, although error magnitudes vary between the different optimized designs. The close agreement between the two 2D models mainly suggests the numerical formulation is mathematically consistent. However, it should not be interpreted as a complete validation of the physical model, since discrepancies can originate from several sources of modeling and experimental uncertainty which may either increase or decrease the predicted eigenfrequencies and damping. The main factors that can contribute to these discrepancies are grouped and discussed below.

Material and constitutive model effects.

- Numerical models assume an homogeneous and isotropic material, whereas this is not the case for 3D printed components. However, DMA measurements indicated a maximum discrepancy of only 10% (see Section 4.2), and the modeled shear modulus aligns well with the tested TPU in the planes where the modes occur. Therefore, material anisotropy is expected to be a secondary contributor compared with the larger discrepancies observed experimentally.
- The viscoelastic material model assumes linear behaviour and uses DMA properties measured at a fixed strain amplitude of 0.1%. During shaker vibration testing, larger local shear strains (see Appendix A.7 for an example) could appear at resonances and particularly in narrow TPU regions where the optimized geometry concentrates deformation. Material properties could therefore follow a non-linear behaviour in these cases, affecting the predicted eigenfrequencies and Q factors. Since no strain amplitude measurements were performed, the magnitude and direction of this effect are difficult to quantify.
- The theoretical model treats the bulk modulus as purely real (see Section 2.1), whereas it also possesses an imaginary component. This effectively provides additional damping although to a lesser extent than the shear modulus. This is because viscoelastic materials are nearly incompressible and they undergo very little volumetric deformation. It is difficult to quantify the effect on the Q factor, as dedicated DMA measurements would be necessary to clearly define the extra loss factor associated with the bulk modulus for TPU. Nevertheless, this effect is expected to be secondary and cannot fully account for the mismatch in the Q factor throughout the results.

Geometry and manufacturing modifications.

- The design obtained by the topology optimization has limited resolution and is modified to create clear and smoother curves suited for CAD modeling. This can slightly modify the distribution of the viscoelastic regions, consequently changing both modal stiffness and energy dissipation. The effect can become more relevant on narrow features, where small geometric changes produce larger variations in local deformation. Nevertheless, the generally close agreement between the framework and COMSOL 2D suggests that this post-processing step has only a limited effect on the global eigenfrequencies.
- The addition of interlocking features and its effect is best described by the base model results in Figure 5.5, where we can observe a small discrepancy added in the 2D model. When comparing the same 3D assembly with and without interlocking features (Figure 6.1) an 8% difference is observed in the eigenfrequencies, while the Q factor seems to be less dependent. Thus, while these features soften the isolator and introduce a frequency offset, they remain a secondary contributor rather than the main driver of the overall mismatch.

Eigenfrequency			
	COMSOL 3D (interlocking)	COMSOL 3D (no interlocking)	Error %
Mode x	681,63	740,68	7,97%
Mode y	461,63	506,65	8,89%
Mode θ	68,71	75,34	8,80%

Q factor			
	COMSOL 3D (interlocking)	COMSOL 3D (no interlocking)	Error %
Mode x	4,80	4,76	0,83%
Mode y	5,03	5,14	2,12%
Mode θ	5,45	5,16	5,70%

Figure 6.1: Eigenfrequency and Q factor comparison for the base case in COMSOL 3D with and without interlocking features.

3D assembly and additional dynamics.

- Alignment errors and geometric asymmetries can modify the magnitude of resonances and structural behaviour. This is likely the main cause for the discrepancy in magnitude observed in the cross-transmissibility T_{xy}, as rationalized in Section 5.1. This is observable only for topology optimized symmetric structures. The x-mode damped isolator presented in Section 5.2.1 is not completely symmetric; as a result, we can see already a better agreement between COMSOL 2D and 3D in T_{xy} looking at Figure D.4c in Appendix D.2.
- Internal flexible modes together with the payload deformation are not taken into account in the framework, while they are present in the experimental assembly. This is visible from around 1500 Hz onwards in the transmissibility plots presented in Sections 5.1 and 5.2. These flexible dynamics primarily affect the response at high frequency, although they may also interact with the rigid-body modes when their resonance frequencies are sufficiently close.

Connections and interface dissipation.

- Bolted connections to the payload can modify the system's structural dynamics and are not taken into account in the numerical models. The influence becomes larger for the stiffer optimized designs, since the compliance becomes more comparable to that of the isolator when treating the assembly as springs in series. Depending on the isolator stiffness, the axial compliance of the two M6 bolts is estimated to reduce the effective vertical stiffness by approximately 2 to 12% in the tested models, which corresponds to around 1 to 6% reduction in the eigenfrequencies (since $\Omega \propto \sqrt{\tilde{\mathbf{K}}^*}$). Additionally, stiffnesses in series derived also from the bolted connections to the shaker and the shaker itself could amplify these errors.
- Related to the previous point, bolted and contacting interfaces could also introduce damping through frictional microslip (Chen and Deng 2005). During cyclic loading, a small relative motion can occur over parts of the clamped surfaces, dissipating energy through frictional hysteresis. This mechanism is not represented by the boundary conditions and could reduce the experimental Q factor. However, the magnitude of this contribution cannot be quantified from the present experiments.

Temperature mismatch.

- Temperature in the laboratory was around $5°C$ higher than the reference temperature at which material properties are set, thus creating a deviation in the experimental data. Using the DMA master curve for TPU and a derived shift factor $a_{25°} = 0.25$, we can observe a reduction of approximately 25% in G' and 30% in G''. This corresponds to roughly a 15% decrease in eigenfrequency. Regarding damping, the $tan(\delta)$ decreases so Q factor increases by about 9%. It is important to note that this applies only for modes with a high percentage of their strain energy stored in the TPU phase, as PLA is captured differently and is less frequency dependent.

  To better understand this effect, Figure 6.2 shows the updated base case results (presented in Section 5.1) using TPU master curves referenced to $25°\mathrm{C}$. The framework's predicted eigenfrequencies align more closely with the test results, halving the initial mismatch, despite a slight increase in Q factor deviation. This indicates that temperature difference is also a plausible contributor in the optimized designs and can contribute to the eigenfrequency shift, whereas the Q factor discrepancy comes mainly from other sources.

Eigenfrequency comparison

	Python	COMSOL 2D	Error %	COMSOL 3D	Error %	Test	Error %
Mode x	601,92	583,70	3,12%	614,01	1,97%	525,00	14,65%
Mode y	462,63	440,30	5,07%	416,31	11,13%	400,00	15,66%
Mode θ	62,04	60,12	3,18%	62,15	0,19%	56,00	10,78%

Damping comparison (Q factor)

	Python	COMSOL 2D	Error %	COMSOL 3D	Error %	Test	Error %
Mode x	4,24	4,29	1,11%	4,73	10,36%	3,85	10,29%
Mode y	4,79	4,92	2,66%	5,34	10,36%	3,47	38,06%
Mode θ	4,99	5,04	0,89%	5,55	10,00%	4,78	4,40%

Figure 6.2: Comparison of predicted and measured eigenfrequencies and associated Q factors for the base case model, using TPU master curves evaluated at $25°\mathrm{C}$.

Looking at general trends, COMSOL 3D models predict higher Q factors (so taller resonance peaks) than the framework. Moving from the plane-strain model to a 3D structure could change the strain energy distribution. A smaller fraction of the total kinetic energy may therefore be dissipated through shear deformation of the TPU, while additional energy is stored elastically in the isolator. This provides a possible explanation for the lower damping predicted by COMSOL 3D, although additional studies on the shear strain energy distribution needs to be performed to decisively prove this.

A further general tendency when comparing framework results to final tested designs is that the rotational mode at the lowest frequency is predicted more accurately than the higher frequency translational mode. The discrepancy therefore tends to increase for the stiffer modes, although the trend does not strictly apply monotonically. One possible reason is that the compliance of the additional connections becomes increasingly important as the isolator stiffness increases. Therefore, the trend may be associated with modelling limitations.

Systematic additional pairs of resonances and anti-resonances appear in the transmissibilities obtained with 3D printed isolators with the shaker. Most occur at similar frequencies across the tested designs, supporting the fact that additional parasitic dynamics are present in the final assembly and is represented in the numerical models. Most noticeably, the horizontal setup used to extract T_{xx} creates the highest peaks and dips, probably caused by the additional components added to balance the system with the counter-mass.

Overall, no single source explains the complete mismatch across the results. The temperature difference and additional compliance from the connections appear to account for a substantial part of the eigenfrequency offset. The generally lower experimental Q factors in several of the relevant modes are likely related to additional dissipative mechanisms that are absent from the numerical models, in particular the frictional losses at mechanical interfaces and potentially non-linear strain deformation in

the viscoelastic material. Moreover, uncertainties associated with the experimental Q factor identification using the half-power bandwidth method may further contribute to this difference. Other effects, including geometric post-processing, anisotropy and interlocking features, appear to have a smaller influence based on the performed comparisons.

These sources of mismatch can be isolated more systematically in future validation steps. First, experimental testing should match more closely the reference temperature specified in the numerical models. Moreover, repeating the tests at lower excitation amplitudes would help determine whether the material response remains within the linear viscoelastic regime, although lower amplitudes may imply lower signal-to-noise ratio for the output data. Finally, the base and payload connections should be characterized more accurately and incorporated into the numerical models. These additional steps would help distinguish the encountered errors before further increasing the complexity of the topology optimization framework.

6.2. Stress constraints and comparison

The present stress formulation remains an approximation and cannot be considered yet a complete failure model. The allowable stresses are interpolated between the two materials, interfaces are assumed perfectly bonded and local failure mechanisms specific to the printed polymers are not represented. In the manufactured structures, failure may instead occur through local separation or delamination between PLA and TPU, as also observed occasionally during preliminary printing tests. A more realistic formulation could introduce a separate interface criterion based on the normal and tangential tractions acting across the material boundaries. Furthermore, the manufactured structure introduces bolt contact, preload and interlocking interfaces which can generate 3D stress concentrations that are absent from the optimization model.

The stress evaluation also shows limitations. Aggregated stresses agree generally better than individual peak values. This happens mainly because the use of linear finite elements can produce very high local stresses near sharp corners, where the results are particularly sensitive to mesh discretization and numerical uncertainty. An example of this phenomenon can be seen in Figure A.1 in Appendix A.6. Finite elements of higher order could additionally improve the accuracy of the strain and stress fields, particularly around curved interfaces and narrow features.

Peak stresses calculated in this manner do not reflect the actual physical stresses experienced during testing, as only the 2D models are used for comparison. As evidence, the rotational mode in Figure 5.21 exceeds the shear strength limit of PLA. However, no structural failure occurred during the physical test.

Interestingly, the y-mode damped isolator design (Section 5.2.2) shows considerably better agreement in the aggregated stresses despite the additional interlocking features in the COMSOL geometry. This suggests that the discrepancy is governed more by local peak stress concentration and mesh sensitivity than by the presence of the interlocks themselves.

The prescribed acceleration used for the stress constraint was found to influence the robustness of the optimization. In the multi-mode case with aluminium and SCVBR®, applying high acceleration simultaneously in multiple directions caused the stress constraint to become strongly active and led to irregular, poorly converged layouts. For future implementations, horizontal and vertical acceleration conditions could be evaluated as independent load cases and subsequently aggregated into a single stress constraint. Different combinations and magnitudes of horizontal and vertical acceleration can lead to different stress distributions and, consequently, different optimized designs, making the choice of load case important. It is important to note that only one set of acceleration conditions was investigated; therefore, the effect of the stress constraint on the final topology was not explored systematically.

6.3. Manufacturing and practical feasibility

The FDM process and materials used in this study intrinsically limits the achievable stiffness and damping performance compared with many industrial vibration isolators. Material filaments have limited loss factors and stiffness properties. The approach used for the experiments should therefore be interpreted primarily as a validation procedure for the proposed design methodology. Interlocking features were introduced as a necessity to maintain the connection between the two printed materials. These fea-

tures, together with known limitations and uncertainties derived from 3D printing, can be avoided if other manufacturing methods are used.

Once the numerical predictions can be reproduced more reliably, more representative materials and manufacturing processes, such as vulcanization, injection moulding or compression moulding, could be investigated to achieve performance closer to industry standards.

A further practical limitation concerns the optimization being performed only in 2D, with the material distribution extruded through the thickness. A full topology optimization in a 3D domain would provide additional design freedom, allowing also the damping material to be placed more selectively. However, this additional freedom would considerably increase the number of design variables and computational cost, and could also generate more complex features that are more difficult to manufacture. Additional steps would then be required inside the framework, for example the inclusion of connectivity constraints via Virtual Temperature Method (S. Liu et al. 2015) and overhang constraints (Langelaar 2016).

7

Conclusions

This thesis investigated the experimental validation of passive vibration isolators in which a stiff and a viscoelastic material can be freely distributed through topology optimization. We extended the existing numerical framework to improve the prediction of the 2D coupled dynamics in frequency domain. To achieve this, we incorporated into the framework a frequency-dependent viscoelastic behaviour, together with stress constraints.

7.1. Contributions

The original topology optimization framework (Petrulis 2025) was extended to provide a more realistic and complete description of the system which includes the isolator and the relative payload. The generalized numerical model now includes the coupling between horizontal translation, vertical translation and in-plane rotation, also accounting for the effective isolator mass contribution.

Frequency-dependent material properties for PLA and TPU were obtained from DMA measurements, to better describe the viscoelastic material that was later used for testing. To incorporate these properties in the topology optimization, a fixed-point iteration method was implemented, allowing each rigid body resonance to be evaluated correctly.

The framework was further extended with dynamic stress evaluation and an aggregated stress constraint, to provide an important criterion for assessing structural feasibility.

Finally and most importantly, the numerical model was connected to a complete experimental validation process. For three different optimization objectives, the 2D topology optimized designs that better balanced stiffness and damping were converted into 3D geometries. They were then printed using multi-material additive manufacturing and tested under horizontal and vertical shaker excitation, adapting the setup accordingly. Their transmissibility and modal properties were compared with the Python framework and with 2D and 3D COMSOL models.

7.2. Findings

The optimization results using TPU and PLA confirm the expected trade-off between high stiffness and high damping. Allowing more viscoelastic material generally increases energy dissipation and reduces the Q factor, but also lowers the system eigenfrequencies. No single design maximizes both properties, and an appropriate compromise must be selected depending on the required application. The minimum eigenfrequency constraint plays an important role in controlling this compromise.

Changing the optimization objective, together with its settings, strongly influences the final material distribution and load path. The frequency dependence was found to be relevant for a more accurate prediction of the isolator performance along the targeted frequency range.

Regarding experimental validation, the simplified framework model successfully reproduced the principal rigid-body resonances and the overall transmissibility behaviour of the manufactured isolators.

More importantly, the intended damping characteristics of the optimized designs were preserved experimentally: the structures optimized for x- and y-mode damping proved to have their highest damping in the targeted mode, while the multi-mode design maintained relatively balanced damping across all three rigid-body modes. The close agreement between the framework and COMSOL 2D further supports the numerical consistency of the reduced formulation. These results indicate that the 2D model implemented in the framework can provide a useful design tool for 3D extruded isolators, although post-processing corrections and additional FEM simulations remain necessary for a more accurate final prediction.

The numerical study using aluminium and SCVBR® demonstrated that the achievable performance strongly depends on the material properties used inside the topology optimization. This alternative combination allowed substantially higher eigenfrequency limits while maintaining favourable damping, and produced narrower viscoelastic regions resembling the conventional constrained-layer damping mechanisms. It is still unclear how challengins would be to test and validate these models. However, the practical manufacturability and experimental validation of these designs remain to be investigated.

The implemented dynamic stress formulation provided consistent global stress trends, with the aggregated stresses generally showing considerably better agreement with COMSOL than individual local peaks. It can therefore be used as a structural constraint during topology optimization. However, local stresses remain sensitive to mesh resolution and geometric singularities, while failure mechanisms at material interfaces, bolt contacts and other 3D features are not represented.

7.3. Recommendations and future work

The most direct extension of the present framework is the implementation of a full three-dimensional domain. This would allow the boundary conditions and out-of-plane structural behaviour to be represented more realistically. Relevant manufacturing constraints can then be added, such as minimum feature size, material connectivity and overhang constraints. However, this extension would require an higher computational cost and the expansion of the dynamical system to account for additional rigid-body modes.

A finer design discretization would allow a more localized placement of the viscoelastic material, while higher-order finite elements could improve the representation of strain and stress fields. These improvements also increase the execution time, particularly because several frequency-dependent analyses are already required within each optimization iteration. Therefore, a careful balance between model accuracy and computational efficiency is required.

Further work should investigate the use of a maximum frequency constraint, to further optimize vibration isolation performance in the final designs. Where appropriate, enforcing geometric symmetry within the topology optimization can help to create more feasible designs. The material model could also be improved by including temperature-dependent properties, utilizing the Time-Temperature Superposition principle and the analytical shift factor correlation.

Further experimental work should focus on creating an improved experimental setup that captures horizontal base excitation, for example using a multi-axis shaking table. Repeated tests at different excitation amplitudes and payload masses should also be conducted to provide a more complete uncertainty assessment and help separate modeling errors from manufacturing variability.

Finally, the framework should be applied to more representative engineering materials and manufacturing processes, such as aluminium combined with molded or vulcanized elastomers. Using these materials would yield more robust numerical data to better validate the correlation between simulated and experimental results. This ultimately represents the logical next step toward developing an industrially relevant passive vibration isolator.

References

Analog Devices (2022). *ADXL345: 3-Axis, Digital Accelerometer*. Rev. G. Analog Devices, Inc. URL: https://www.analog.com/media/en/technical-documentation/data-sheets/ADXL345.pdf.

Bambu Lab (2026a). *PLA Basic Filament*. Bambu Lab EU Store. URL: https://eu.store.bambulab.com/products/pla-basic-filament?id=42911328010459.

— (2026b). *TPU 95A HF*. Bambu Lab EU Store. URL: https://eu.store.bambulab.com/products/tpu-95a-hf.

Beijen, M. A., R. Voorhoeve, M. F. Heertjes, and T. Oomen (2018). "Experimental estimation of transmissibility matrices for industrial multi-axis vibration isolation systems". In: *Mechanical Systems and Signal Processing* 107, pp. 469–483. DOI: 10.1016/j.ymssp.2018.01.013.

Bower, A. F. (2009). *Applied Mechanics of Solids*. 1st ed. CRC Press. DOI: 10.1201/9781439802489.

Budynas, R. G. and J. K. Nisbett (2015). *Shigley's Mechanical Engineering Design*. 10th ed. McGraw-Hill Education.

Casiano, M. J. (2016). *Extracting Damping Ratio from Dynamic Data and Numerical Solutions*. NASA Technical Memorandum NASA/TM-2016-218227. Huntsville, Alabama: NASA Marshall Space Flight Center. URL: https://ntrs.nasa.gov/citations/20170005173.

Chen, W. and X. Deng (2005). "Structural damping caused by micro-slip along frictional interfaces". In: *International Journal of Mechanical Sciences* 47.8, pp. 1191–1211. DOI: 10.1016/j.ijmecsci.2005.04.005.

COMSOL AB (2024a). "Linear Viscoelasticity". In: *Structural Mechanics Module User's Guide*. COMSOL Multiphysics, Version 6.3. COMSOL AB. URL: https://doc.comsol.com/6.3/doc/com.comsol.help.sme/sme_ug_theory.06.029.html.

— (2024b). *Structural Mechanics Module User's Guide: Frequency-Domain Studies*. 6.4. URL: https://doc.comsol.com/6.4/doc/com.comsol.help.sme/sme_ug_theory.06.053.html.

— (2025). *Eigenfrequency Studies*. COMSOL Multiphysics, Version 6.4. URL: https://doc.comsol.com/6.4/doc/com.comsol.help.sme/sme_ug_theory.06.054.html.

Davies, Francis (2015). *Electric Power in Sea & Space: Space Power Management and Distribution*. Presentation at the Deep Space, Deep Ocean Forum 2015. URL: https://ntrs.nasa.gov/citations/20150004609.

Delissen, A. (2023). *pyMOTO: Modular framework for topology optimization with semi-automatic derivatives*. Computer software. Version 1.0.1. Zenodo. DOI: 10.5281/zenodo.7708738.

Dennehy, C. and O. S. Alvarez-Salazar (2018). *Spacecraft micro-vibration: A survey of problems, experiences, potential solutions, and some lessons learned*. NASA Technical Memorandum NASA/TM-2018-220075. National Aeronautics and Space Administration. URL: https://ntrs.nasa.gov/citations/20180006315.

Doelman, N. J., G. Witvoet, D. de Bruijn, A. Bos, A. A. T. M. Delissen, D.-N. Nguyen, L. C. W. Scheers, H. van Brug, R. J. Voorhoeve, K. A. Broekens, C. W. Korevaar, and F. C. M. van Kempen (2026). "Design and in-orbit performance of a 1U 1 Gbit/s optical communication terminal". In: *IEEE Journal of Selected Topics in Quantum Electronics*. DOI: 10.1109/JSTQE.2026.3655556.

Du, J. and N. Olhoff (2007). "Topological design of freely vibrating continuum structures for maximum values of simple and multiple eigenfrequencies and frequency gaps". In: *Structural and Multidisciplinary Optimization* 34.2, pp. 91–110. DOI: 10.1007/s00158-007-0101-y.

Elkhoury, K., G.-L. Chen, E. N. Noshahri, J. Zuazola, N. Gupta, and S. Vijayavenkataraman (2025). "Viscoelastic to elastic transformation of soft polymer properties for accelerated materials selection based on tissue dynamics in tissue engineering applications". In: *Polymer Testing* 146, 108778. DOI: 10.1016/j.polymertesting.2025.108778.

Elmoghazy, Y. H., B. Safaei, M. Asmael, S. Sahmani, Q. Zeeshan, and Z. Qin (2024). "Computational Modelling and Analysis of Effect of Viscoelastic Materials on Damping and Vibrational Behaviors of Composite Structures—An Extensive Review". In: *Archives of Computational Methods in Engineering* 31.5, pp. 2611–2662. DOI: 10.1007/s11831-023-10057-4.

Ferry, J. D. (1980). *Viscoelastic Properties of Polymers*. 3rd ed. John Wiley & Sons.

Harris, Fredric J. (1978). “On the Use of Windows for Harmonic Analysis with the Discrete Fourier Transform”. In: *Proceedings of the IEEE* 66.1, pp. 51–83. DOI: 10.1109/PROC.1978.10837.

Jauregui, J. C., ed. (2019). *Nonlinear Structural Dynamics and Damping*. Vol. 69. Mechanisms and Machine Science. Springer International Publishing. DOI: 10.1007/978-3-030-13317-7.

Johal, R., J. Christensen, and D. Doud (2012). “ORBCOMM Generation 2 access to LEO on the Falcon 9 using SoftRide: A case history”. In: *Proceedings of the 26th Annual AIAA/USU Conference on Small Satellites*, pp. 1–12. URL: https://digitalcommons.usu.edu/smallsat/2012/all2012/44/.

Karnopp, D. C. (1995). “Active and Semi-Active Vibration Isolation”. In: *Journal of Mechanical Design* 117.B, pp. 177–185. DOI: 10.1115/1.2838660.

Kelley, C. T. (2018). “Numerical Methods for Nonlinear Equations”. In: *Acta Numerica* 27, pp. 207–287. DOI: 10.1017/S0962492917000113.

Kempen, F. C. M. van, J. de Vreugd, and W. E. Crowcombe (2023). “Device for mounting a load to a carrier, assembly, vehicle and methods”. U.S. Patent Application Publication US 2023/0133102 A1. United States Patent and Trademark Office. URL: https://patents.google.com/patent/US20230133102A1/en.

Kim, S.-Y., C. K. Mechefske, and I. Y. Kim (2013). “Optimal Damping Layout in a Shell Structure Using Topology Optimization”. In: *Journal of Sound and Vibration* 332.12, pp. 2873–2883. DOI: 10.1016/j.jsv.2013.01.029.

Kolk, M. van der, G. J. van der Veen, J. de Vreugd, and M. Langelaar (2017). “Multi-material topology optimization of viscoelastically damped structures using a parametric level set method”. In: *Journal of Vibration and Control* 23.15, pp. 2430–2443. DOI: 10.1177/1077546315617333.

Langelaar, M. (2016). “Topology optimization of 3D self-supporting structures for additive manufacturing”. In: *Additive Manufacturing* 12, pp. 60–70. DOI: 10.1016/j.addma.2016.06.010.

Liu, Q., D. Ruan, and X. Huang (2018). “Topology optimization of viscoelastic materials on damping and frequency of macrostructures”. In: *Computer Methods in Applied Mechanics and Engineering* 337, pp. 305–323. DOI: 10.1016/j.cma.2018.03.044.

Liu, Shutian, Quhao Li, Wenjiong Chen, Liyong Tong, and Gengdong Cheng (2015). “An identification method for enclosed voids restriction in manufacturability design for additive manufacturing structures”. In: *Frontiers of Mechanical Engineering* 10, pp. 126–137. DOI: 10.1007/s11465-015-0340-3.

Menard, K. P. and N. Menard (2020). *Dynamic Mechanical Analysis: A Practical Introduction*. 3rd ed. CRC Press.

Menzel, M., M. Davis, K. Parrish, J. Lawrence, A. Stewart, J. Cooper, S. Irish, G. Mosier, M. Levine, J. Pitman, G. Walsh, P. Maghami, S. Thomson, E. Wooldridge, R. Boucarut, L. Feinberg, G. Turner, P. Kalia, and C. Bowers (2023). “The design, verification, and performance of the James Webb Space Telescope”. In: *Publications of the Astronomical Society of the Pacific* 135.1047, 058002. DOI: 10.1088/1538-3873/acbb9f.

Moreira, R. A. S. (2014). “Structural dynamics and viscoelastic passive damping treatments”. In: *Modern Mechanical Engineering: Research, Development and Education*. Ed. by J. P. Davim. Springer, pp. 89–107. DOI: 10.1007/978-3-642-45176-8_5.

Müller, Swen and Paulo Massarani (2001). “Transfer-Function Measurement with Sweeps”. In: *Journal of the Audio Engineering Society* 49.6, pp. 443–471.

Niu, B., X. He, Y. Shan, and R. Yang (2018). “On objective functions of minimizing the vibration response of continuum structures subjected to external harmonic excitation”. In: *Structural and Multidisciplinary Optimization* 57.6, pp. 2291–2307. DOI: 10.1007/s00158-017-1859-1.

Papagiannopoulos, George A. and George D. Hatzigeorgiou (2011). “On the use of the half-power bandwidth method to estimate damping in building structures”. In: *Soil Dynamics and Earthquake Engineering* 31.7, pp. 1075–1079. DOI: 10.1016/j.soildyn.2011.02.007.

Petrulis, J. S. (2025). “Topology optimisation for passive viscoelastic vibration isolators using a modal design approach”. Master’s thesis. Delft University of Technology. URL: https://resolver.tudelft.nl/uuid:fc8a7e9b-b93c-478d-8395-25cb4fe179c2.

Rossing, L., R. B. N. Scharff, B. Chömpff, C. C. L. Wang, and E. L. Doubrovski (2020). “Bonding between silicones and thermoplastics using 3D printed mechanical interlocking”. In: *Materials & Design* 186, 108254. DOI: 10.1016/j.matdes.2019.108254.

Sardinha, Manuel, Luís Ferreira, Hermínio Diogo, Tânia R. P. Ramos, Luís Reis, and M. Fátima Vaz (2025). “Material extrusion of TPU: thermal characterization and effects of infill and extrusion temperature on voids, tensile strength and compressive properties”. In: *Rapid Prototyping Journal* 31.11, pp. 62–81. DOI: 10.1108/RPJ-06-2024-0241.

Shi, H. T., M. Abubakar, X. T. Bai, and Z. Luo (2024). “Vibration isolation methods in spacecraft: A review of current techniques”. In: *Advances in Space Research* 73.8, pp. 3993–4023. DOI: 10.1016/j.asr.2024.01.020.

Shu, Z., R. You, and Y. Zhou (2022). “Viscoelastic Materials for Structural Dampers: A Review”. In: *Construction and Building Materials* 342, 127955. DOI: 10.1016/j.conbuildmat.2022.127955.

Space Exploration Technologies Corp. (2022). *Rideshare Payload User’s Guide*. User guide. Space Exploration Technologies Corp. URL: https://experiorlabs.com/wp-content/uploads/2023/06/Rideshare_Payload_Users_Guide.pdf.

Struz, J., M. Trochta, L. Hruzik, D. Pistacek, S. Stawarz, W. Kucharczyk, and M. Rucki (2024). “Wear and Dynamic Mechanical Analysis (DMA) of Samples Produced via Fused Deposition Modelling (FDM) 3D Printing Method”. In: *Polymers* 16.21, 3018. DOI: 10.3390/polym16213018.

Svanberg, K. (1987). “The Method of Moving Asymptotes—A New Method for Structural Optimization”. In: *International Journal for Numerical Methods in Engineering* 24.2, pp. 359–373. DOI: 10.1002/nme.1620240207.

Tanaka, E. and T. M. G. J. van Eijden (2003). “Biomechanical behavior of the temporomandibular joint disc”. In: *Critical Reviews in Oral Biology & Medicine* 14.2, pp. 138–150. DOI: 10.1177/154411130301400207.

Tschoegl, N. W. (1989). *The Phenomenological Theory of Linear Viscoelastic Behavior: An Introduction*. Springer-Verlag. DOI: 10.1007/978-3-642-73602-5.

UltiMaker (2023). *Unlock true multi-material printing with UltiMaker Cura 5.3*. URL: https://ultimaker.com/learn/unlock-true-multi-material-printing-with-ultimaker-cura-5-3/.

Verbart, A., M. Langelaar, and F. van Keulen (2017). “A unified aggregation and relaxation approach for stress-constrained topology optimization”. In: *Structural and Multidisciplinary Optimization* 55.2, pp. 663–679. DOI: 10.1007/s00158-016-1524-0.

Wang, Qinglin, Gonghe Zhang, Xiaodong Zheng, Yinxu Ni, Fenghua Liu, Yang Liu, and Luoyu Roy Xu (2023). “Efficient characterization on the interlayer shear strengths of 3D printing polymers”. In: *Journal of Materials Research and Technology* 22, pp. 2768–2780. DOI: 10.1016/j.jmrt.2022.12.147.

Welch, Peter D. (1967). “The Use of Fast Fourier Transform for the Estimation of Power Spectra: A Method Based on Time Averaging Over Short, Modified Periodograms”. In: *IEEE Transactions on Audio and Electroacoustics* 15.2, pp. 70–73. DOI: 10.1109/TAU.1967.1161901.

Zhang, D., Y. Wu, X. Lu, and L. Zheng (2022). “Topology optimization of constrained layer damping plates with frequency- and temperature-dependent viscoelastic core via parametric level set method”. In: *Mechanics of Advanced Materials and Structures* 29.1, pp. 154–170. DOI: 10.1080/15376494.2021.1938302.

Zhang, G. and K. Khandelwal (2019). “Design of dissipative multimaterial viscoelastic-hyperelastic systems at finite strains via topology optimization”. In: *International Journal for Numerical Methods in Engineering* 119.11, pp. 1037–1068. DOI: 10.1002/nme.6083.

Zou, X. C., Z. Q. Li, X. S. Zhao, T. Sun, and K. P. Zhang (2014). “Study on the auto-leveling adjustment vibration isolation system for the ultra-precision machine tool”. In: *Proceedings of SPIE* 9281, 92812L. DOI: 10.1117/12.2069463.

A

Mathematical Derivations

A.1. Reduced stiffness matrix derivation

The structural behavior can be characterized energetically. The total internal strain energy of the system is described by the formula

$$\mathbf{E} = \frac{1}{2}\mathbf{u}^T\mathbf{K}^*\mathbf{u} \tag{A.1}$$

To avoid tracking every independent node in the high-dimensional system, we map the global deformation vector $\mathbf{u}$ onto the low-dimensional subspace spanned by $\mathbf{U}$, yielding the generalized coordinate vector $\mathbf{q}$:

$$\mathbf{u} = \mathbf{U}\mathbf{q} \tag{A.2}$$

Substituting this coordinate transformation back into the strain energy formula allows us to express the system's energy strictly in terms of the generalized coordinate vector $\mathbf{q}$

$$\mathbf{E} = \frac{1}{2}\mathbf{q}^T\left(\mathbf{U}^T\mathbf{K}^*\mathbf{U}\right)\mathbf{q} \tag{A.3}$$

Within this expression, the central matrix product can be grouped together to define a compact, reduced-order generalized stiffness matrix $\mathbf{K}_{\text{gen}}$:

$$\tilde{\mathbf{K}}^* = \mathbf{U}^T\mathbf{K}^*\mathbf{U} \in \mathbb{R}^{3\times 3} \tag{A.4}$$

Knowing that $\mathbf{F} = \mathbf{K}\mathbf{U}$, we can define the reduced stiffness matrix using only the computed output force and displacement state matrices:

$$\tilde{\mathbf{K}}^* = \mathbf{U}^T\mathbf{F} \tag{A.5}$$

A.2. Reduced payload mass matrix derivation

To adjust the inertia and have a coherent dynamical system, we need to represent the payload as a rigid body rather than as a point mass. The center of rotation is now defined at point O in Figure 2.7, differently from the center of mass of the payload. The translational velocity of point O can be described by the formula

$$\mathbf{v}_{\mathrm{O}} = \mathbf{v}_{\mathrm{G}} + \bar{\boldsymbol{\omega}} \times \mathbf{r}_{\mathrm{G/O}}, \tag{A.6}$$

knowing the distance $\mathbf{r}_{\mathrm{G/O}}$ from point G (center of mass of the payload) to point O, the rotational velocity $\bar{\omega}$ and translation velocity of point G. Equation A.6 can be applied inside the total kinetic energy created by the payload

$$T_{\mathrm{p}} = \frac{1}{2}\mathbf{v}_{\mathrm{O}}^T m_{\mathrm{G}}\mathbf{v}_{\mathrm{O}} + \frac{1}{2}I_{\mathrm{G}}\dot{q}_\theta^2. \tag{A.7}$$

Then, the derived kinetic energy of the system can be rearranged component-wise in matrix form:

$$T_{\mathrm{p}} = \frac{1}{2}\,\dot{\mathbf{q}}^{T}\mathbf{M}_{p}\dot{\mathbf{q}} = \frac{1}{2}\begin{bmatrix}\dot{q_x} & \dot{q_y} & \dot{q_\theta}\end{bmatrix}\begin{bmatrix} m_{\mathrm{G}} & 0 & -m_{\mathrm{G}}d \\ 0 & m_{\mathrm{G}} & 0 \\ -m_{\mathrm{G}}d & 0 & I_G + m_{\mathrm{G}}d^2 \end{bmatrix}\begin{bmatrix}\dot{q_x} \\ \dot{q_y} \\ \dot{q_\theta}\end{bmatrix}, \tag{A.8}$$

where the velocities are now described as first derivatives of $\mathbf{q}$ and the generalized mass matrix $\mathbf{M}_p \in \mathbb{R}^{3\times 3}$ contains off-diagonal coupling terms. Notably, the last diagonal component accounts for the shifted inertia of the payload commonly derived by the parallel axis theorem.

A.3. Eigenmodes sorting

The eigenvalue problem is solved for each mode $i \in \{x, y, \theta\}$ and the solver returns three eigenvectors $\boldsymbol{\phi}_{i,r}$, with $r \in \{1, 2, 3\}$, usually sorted by the eigenvalue magnitude. However, this numerical ordering does not uniquely identify the physical rigid-body direction of each mode and a proper mode identification is crucial to assemble the correct vector for later calculations. Also, the eigenvector order changes as the structural domain evolves during the optimization. The modes are therefore classified using their effective modal mass in the three generalized directions (COMSOL AB 2025).

First, each eigenvector is normalized with respect to the generalized mass matrix:

$$m_{i,r} = \Re\left\{\boldsymbol{\phi}_{i,r}^{H}\tilde{\mathbf{M}}_{i}\boldsymbol{\phi}_{i,r}\right\}, \qquad \overline{\boldsymbol{\phi}}_{i,r} = \frac{\boldsymbol{\phi}_{i,r}}{\sqrt{m_{i,r}}}. \tag{A.9}$$

Since the rotational coordinate has different units from the translational coordinates, it is scaled by a length equivalent to half of the payload height d:

$$\overline{\boldsymbol{\phi}}'_{i,r} = \underbrace{\begin{bmatrix}1 & 0 & 0\\ 0 & 1 & 0\\ 0 & 0 & d\end{bmatrix}}_{\mathbf{S}}\overline{\boldsymbol{\phi}}_{i,r}, \qquad \tilde{\mathbf{M}}'_{i} = \mathbf{S}^{-T}\tilde{\mathbf{M}}_{i}\mathbf{S}^{-1}. \tag{A.10}$$

For each generalized direction $j \in \{x, y, \theta\}$, the effective modal mass and its corresponding fraction μ are then evaluated as

$$m_{\mathrm{eff},j}^{(i,r)} = \left|\left(\overline{\boldsymbol{\phi}}'_{i,r}\right)^{H}\tilde{\mathbf{M}}'_{i}\mathbf{e}_{j}\right|^{2}, \qquad \mu_{j}^{(i,r)} = \frac{m_{\mathrm{eff},j}^{(i,r)}}{\left(\tilde{\mathbf{M}}'_{i}\right)_{jj}}. \tag{A.11}$$

A large value of $\mu_{j}^{(i,r)}$ indicates that eigenmode r contains a large fraction of the inertial motion associated with generalized direction j. The rotational mode is first identified from the largest rotational fraction $\mu_{\theta}^{(i,r)}$, after which the horizontal mode is selected. Finally, the remaining eigenmode is assigned to the y direction. At the end, we have a unique identification of the x-, y-, and θ-modes at every iteration, respectively in this order. It is important to note that uncertainties may arise when two or more eigenfrequencies have a similar value.

A.4. Rigid-body transformation to the sensor position

The generalized coordinates describe the motion of the payload reference point. To obtain the motion at the top right corner of the payload, consider in this case the point S located at

$$\mathbf{r}_{\mathrm{S/O}} = \begin{bmatrix} r_x \\ r_y \\ 0 \end{bmatrix} \tag{A.12}$$

relative to this reference point. After an in-plane rotation q_θ, its position is transformed through the rotation matrix

$$\mathbf{R}_z(q_\theta) = \begin{bmatrix} \cos q_\theta & -\sin q_\theta & 0 \\ \sin q_\theta & \cos q_\theta & 0 \\ 0 & 0 & 1 \end{bmatrix}. \tag{A.13}$$

The displacement produced by the rotation is therefore

$$\mathbf{q}_{\mathrm{rot}} = \left[\mathbf{R}_z(q_\theta) - \mathbf{I}\right] \mathbf{r}_{\mathrm{S/O}}. \tag{A.14}$$

Under the small rotation and linear regime assumptions, $\sin q_\theta \approx q_\theta$ and $\cos q_\theta \approx 1$ and the total displacement at the new point can be defined as

$$\mathbf{q}_{\mathrm{S}} = \mathbf{q} + \mathbf{q}_{\mathrm{rot}} \approx \begin{bmatrix} q_x - r_y q_\theta \\ q_y + r_x q_\theta \\ q_\theta \end{bmatrix}. \tag{A.15}$$

Adding the translations q_x and q_y of the reference point gives the motion at the sensor position,

$$\begin{bmatrix} q_{x,\mathrm{S}} \\ q_{y,\mathrm{S}} \\ q_{\theta,\mathrm{S}} \end{bmatrix} = \underbrace{\begin{bmatrix} 1 & 0 & -r_y \\ 0 & 1 & r_x \\ 0 & 0 & 1 \end{bmatrix}}_{\mathbf{R}_{\mathrm{S}}} \begin{bmatrix} q_x \\ q_y \\ q_\theta \end{bmatrix}. \tag{A.16}$$

A.5. Peak von Mises stress for complex harmonic stresses

In the frequency-domain formulation used in this work, the displacement, strain and stress fields are complex-valued phasors. Therefore, the stress vector obtained from the finite-element calculation is not directly the physical stress at every instant in time. For one element and one modal stress case, the complex stress vector is written as

$$\hat{\boldsymbol{\sigma}} = \begin{bmatrix} \hat{\sigma}_{xx} \\ \hat{\sigma}_{yy} \\ \hat{\sigma}_{zz} \\ \hat{\tau}_{xy} \end{bmatrix} = \boldsymbol{\sigma}_R + i\boldsymbol{\sigma}_I, \tag{A.17}$$

where $\boldsymbol{\sigma}_R$ and $\boldsymbol{\sigma}_I$ are respectively the real and imaginary parts of the stress phasor. The corresponding real physical stress during one harmonic cycle is

$$\boldsymbol{\sigma}(t) = \Re\left\{\hat{\boldsymbol{\sigma}} e^{i\omega t}\right\} = \boldsymbol{\sigma}_R \cos(\omega t) - \boldsymbol{\sigma}_I \sin(\omega t). \tag{A.18}$$

For a real instantaneous plane-strain stress state, including the non-zero out-of-plane stress σ_{zz}, the von Mises stress is

$$\sigma_{\mathrm{vm}}^2 = \sigma_{xx}^2 + \sigma_{yy}^2 + \sigma_{zz}^2 - \sigma_{xx}\sigma_{yy} - \sigma_{yy}\sigma_{zz} - \sigma_{zz}\sigma_{xx} + 3\tau_{xy}^2. \tag{A.19}$$

This expression can be written as a quadratic form,

$$\sigma_{\mathrm{vm}}^2 = \boldsymbol{\sigma}^T \mathbf{V} \boldsymbol{\sigma}, \tag{A.20}$$

with

$$\mathbf{V} = \begin{bmatrix} 1 & -\frac{1}{2} & -\frac{1}{2} & 0 \\ -\frac{1}{2} & 1 & -\frac{1}{2} & 0 \\ -\frac{1}{2} & -\frac{1}{2} & 1 & 0 \\ 0 & 0 & 0 & 3 \end{bmatrix}. \tag{A.21}$$

Substituting the real time-dependent stress into this quadratic form gives

$$\sigma_{\mathrm{vm}}^2(t) = \left(\boldsymbol{\sigma}_R \cos(\omega t) - \boldsymbol{\sigma}_I \sin(\omega t)\right)^T \mathbf{V} \left(\boldsymbol{\sigma}_R \cos(\omega t) - \boldsymbol{\sigma}_I \sin(\omega t)\right). \tag{A.22}$$

Defining

$$X = \boldsymbol{\sigma}_R^T \mathbf{V} \boldsymbol{\sigma}_R, \qquad Y = \boldsymbol{\sigma}_I^T \mathbf{V} \boldsymbol{\sigma}_I, \qquad Z = \boldsymbol{\sigma}_R^T \mathbf{V} \boldsymbol{\sigma}_I, \tag{A.23}$$

the time-dependent squared von Mises stress becomes

$$\sigma_{\mathrm{vm}}^2(t) = X \cos^2(\omega t) + Y \sin^2(\omega t) - 2Z \sin(\omega t) \cos(\omega t). \tag{A.24}$$

The quantities X and Y are the squared von Mises values associated with the real and imaginary stress patterns separately, while Z is the cross-term that accounts for their interaction. The maximum value over one harmonic cycle is found by rewriting the expression as

$$\sigma_{\mathrm{vm}}^2(t) = \begin{bmatrix} \cos(\omega t) & \sin(\omega t) \end{bmatrix} \begin{bmatrix} X & -Z \\ -Z & Y \end{bmatrix} \begin{bmatrix} \cos(\omega t) \\ \sin(\omega t) \end{bmatrix}. \tag{A.25}$$

Since $\cos^2(\omega t) + \sin^2(\omega t) = 1$, the maximum of this quadratic form is equal to the largest eigenvalue of the 2×2 matrix. The two eigenvalues are

$$\lambda_{\pm} = \frac{X + Y}{2} \pm \frac{1}{2} \sqrt{(X - Y)^2 + 4Z^2}. \tag{A.26}$$

Therefore, the peak squared von Mises stress over one harmonic cycle is

$$\sigma_{\mathrm{vm,peak}}^2 = \frac{1}{2} \left[X + Y + \sqrt{(X - Y)^2 + 4Z^2} \right], \tag{A.27}$$

and the peak von Mises stress used in the stress constraint is

$$\sigma_{\mathrm{vm,peak}} = \sqrt{\frac{1}{2} \left[X + Y + \sqrt{(X - Y)^2 + 4Z^2} \right]}. \tag{A.28}$$

This peak value over the cycles is independent of the arbitrary phase chosen for the frequency-domain solution. This result is therefore more appropriate for a stress constraint than taking only the real part of the complex stress field, which would correspond only to the instantaneous stress at one specific phase.

This derivation follows the derivation used for maximum cyclic stress evaluation in COMSOL Multiphysics (COMSOL AB 2024b).

A.6. Stress field comparison

Figure A.1 shows the local von Mises stress distribution near the region where the peak stress occurs in both the Python framework and COMSOL 2D model. This comparison helps us understand whether the two models identify the same stress concentration and general distribution.

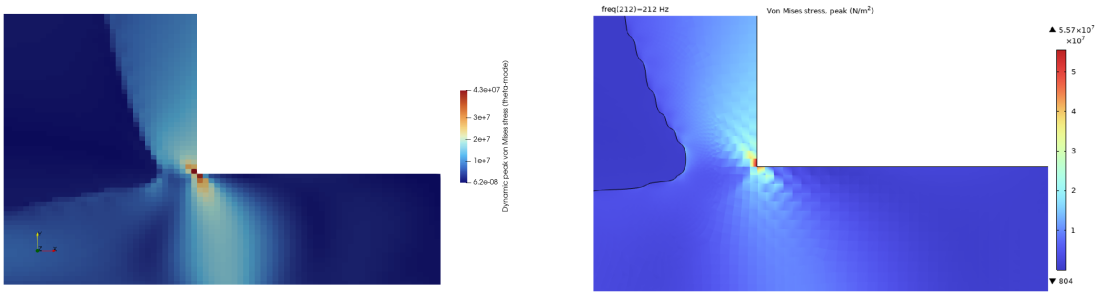


Figure A.1: Detail of FE elements where peak stresses are present, for both Python framework and COMSOL 2D.

A.7. Strain simulation example

A FEM simulation in frequency domain using COMSOL is conducted to show high shear local strain on the design case for y- mode damping (Section 5.2.2). In particular Figure A.2 shows the engineering shear strain amplitude at the first rotational mode, occurring at around 185 Hz, under a prescribed horizontal base acceleration of $5g$. We can see that local strains reach 4% in the narrow TPU region, substantially above the $0,1\%$ shear strain relative amplitude used to obtain the TPU DMA master curve. This indicates that strain amplitude dependence may become relevant locally under sufficiently high excitation.

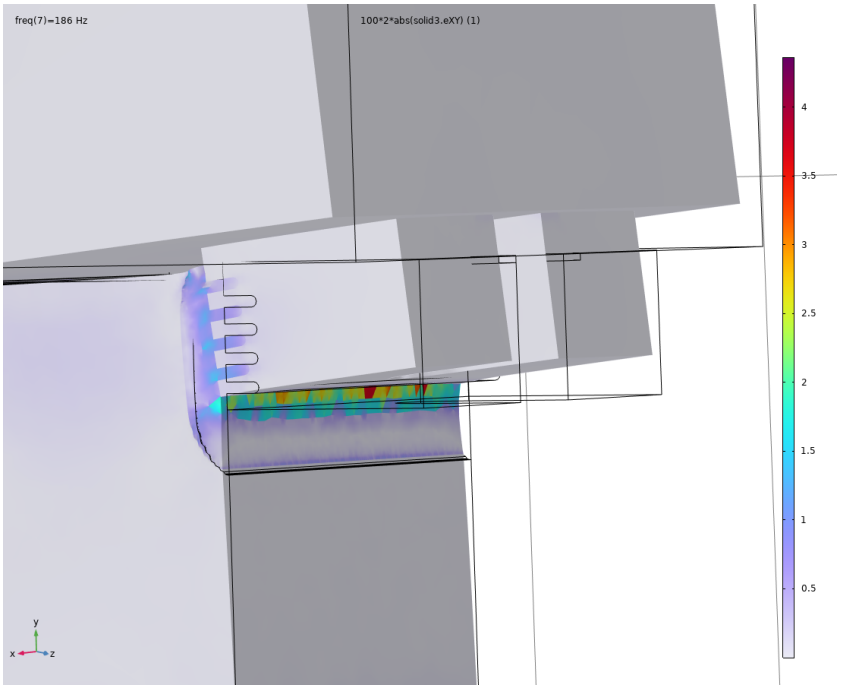


Figure A.2: Engineering shear strain amplitude in the y-mode damped isolator at the first rotational resonance.

B

Additional modal deformation of isolator designs

This appendix presents the modal deformation and shear strain energy distributions of the optimized designs obtained with the alternative pair of materials (aluminium and SCVBR®) discussed in Section 5.3.2.

B.1. x-mode damping (alternative materials)

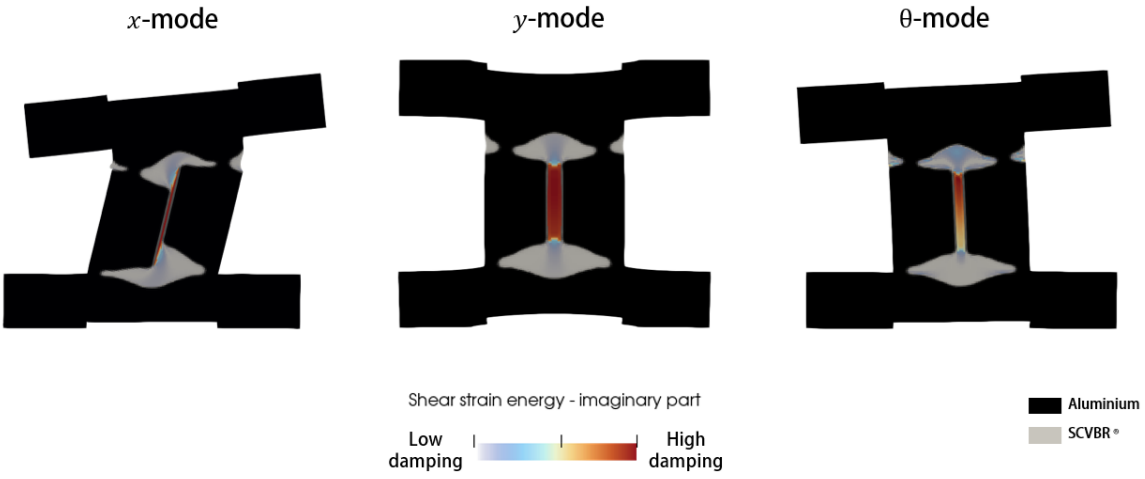


Figure B.1: Deformed shapes and shear strain energy distributions (imaginary part) for the x-mode damped isolator in the x-, y- and θ-modes, using aluminium and SCVBR® elastomer

B.2. y-mode damping (alternative materials)

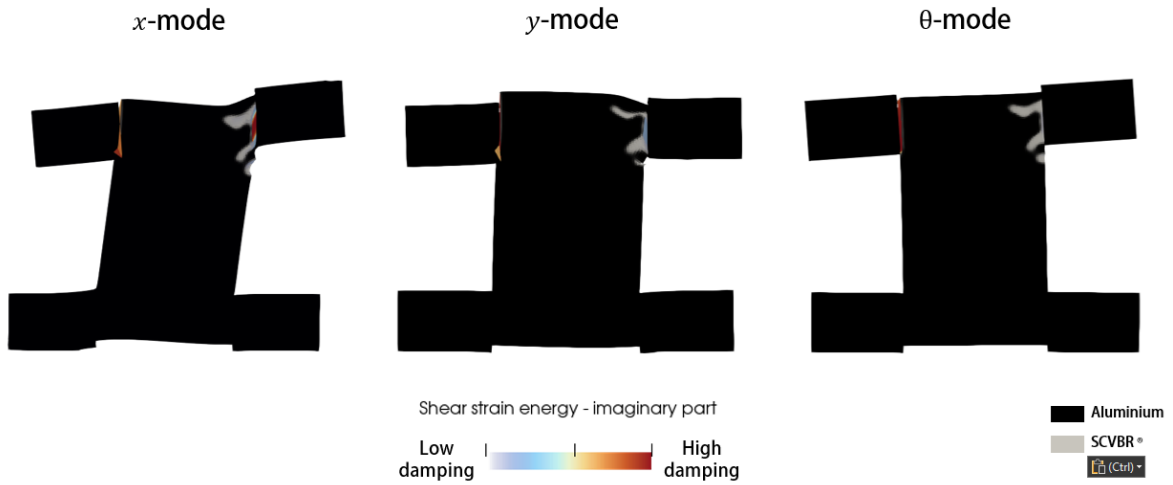


Figure B.2: Deformed shapes and shear strain energy distributions (imaginary part) for the y-mode damped isolator in the x-, y- and θ-modes, using aluminium and SCVBR® elastomer.

B.3. Multi-mode damping (alternative materials)

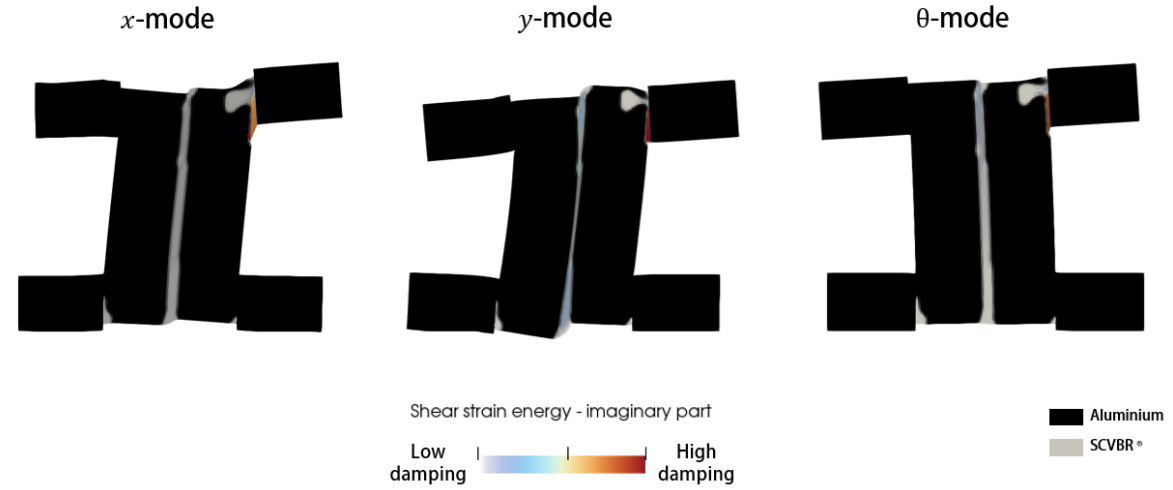


Figure B.3: Deformed shapes and shear strain energy distributions (imaginary part) for the multi-mode damped isolator in the x-, y- and θ-modes, using aluminium and SCVBR® elastomer.

C

Arduino setup

An alternative and cheaper experimental setup has also been assembled to extrapolate the transmissibility plots. The main electronic components used are:

- Raspberry Pi Pico H.
- Two ADXL345 tri-axial accelerometers. In the present setup, the sensors were operated in full-resolution mode with a $\pm 2\,g$ measurement range. The main sensor characteristics relevant to the vibration measurements are summarized in Table C.1 based on the datasheet (Analog Devices 2022).
- Quad 2-Input 74HC32 logic gate.
- Capacitor $100\ \mathrm{nF}$.

One accelerometer was mounted at the shaker base to measure the input acceleration, while the second was mounted on the payload to measure the output response. To mount the accelerometers, threaded inserts were added to the custom-made base and payload components. During acquisition, the Raspberry Pi Pico reads the two accelerometers simultaneously and transmits the measured acceleration components to the computer. The complete circuit can be seen here below in Figure C.1, while the laboratory setup is shown in Figure C.2.

Table C.1: ADXL345 specifications (Analog Devices 2022).

Parameter	**Value**
Measurement range	$\pm 2\,g$
Scale factor	3.9 mg/LSB
Output data rate	1600 Hz
Bandwidth	800 Hz
Noise density (x, y)	$290\,\mu g/\sqrt{\mathrm{Hz}}$

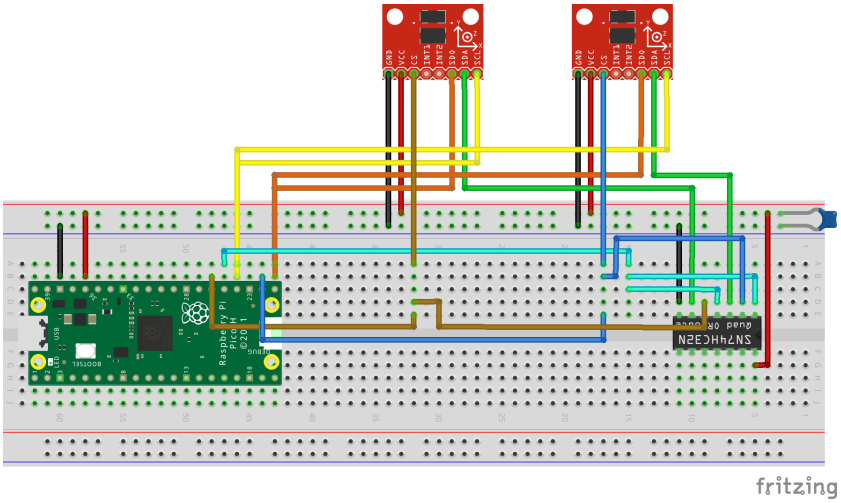


Figure C.1: Raspberry Pi Pico H and ADXL345 acquisition circuit using a breadboard.

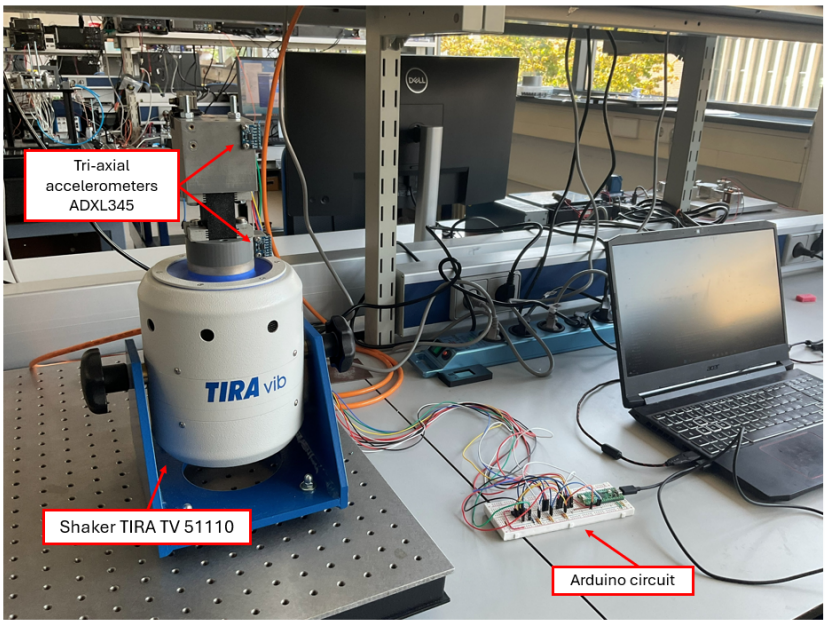


Figure C.2: Low-cost experimental setup using ADXL345 accelerometers.

The acquired signals are processed using the same frequency sweep identification procedure described in Section 4.3.1 for the NI cDAQ measurements. At the end, transmissibility and coherence are calculated in the same in-plane directions. In this case the experiment was performed only under vertical shaker excitation.

Figure C.3 compares T_{yy} and T_{xy} transmissibilities obtained with the ADXL345 setup against those measured using the B&K Type 4506 accelerometers for the TPU base case (introduced in Section 5.1). We can see that the inexpensive system reproduces the main trend and resonance of the direct transmissibility, although larger differences and higher noise are visible in T_{xy} and at high frequency near the bandwidth limit of the ADXL345 accelerometers. This Arduino implementation provides an additional comparison and demonstrates a simpler low-cost measurement alternative.

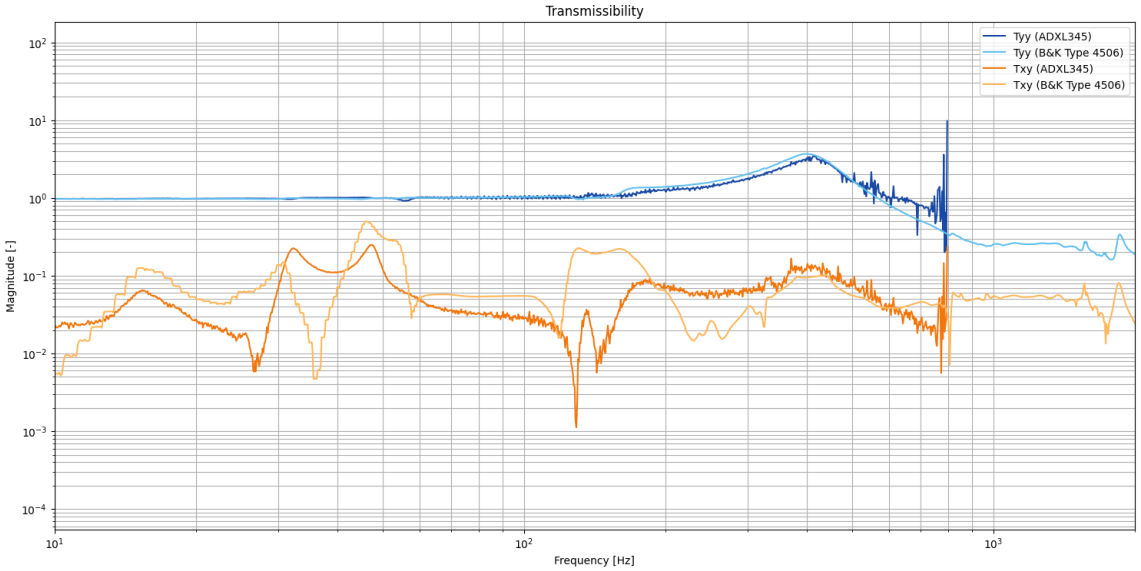


Figure C.3: T_{yy} and T_{xy} plots comparison using ADXL345 accelerometers versus B&K Type 4506 accelerometers.

The Arduino code used to acquire the two ADXL345 signals is provided in Listing C.1. The code initializes both accelerometers, samples their three acceleration components, assigns a timestamp and sequence number to each measurement frame, and transfers the data to the computer for post-processing.

Listing C.1: Firmware used for acquisition of the two ADXL345 accelerometers with the Raspberry Pi Pico H.

```
#include <SPI.h>


// USER SETTINGS

// ADXL345 ODR code:
const uint8_t BW_RATE_CODE = 0x0E; // 0x0E = 1600 Hz ODR, 800 Hz bandwidth

// Full-resolution, +/- 2 g
const uint8_t DATA_FORMAT_VALUE = 0x08;

// ODR and lower SPI clock
const uint32_t TARGET_ODR_HZ = 1600;
const uint32_t SPI_CLOCK_HZ = 5000000;


// PICO H PIN ASSIGNMENT
// Shared SPI bus
const uint8_t PIN_MISO = 16;   // GP16
const uint8_t PIN_SCK  = 18;   // GP18
const uint8_t PIN_MOSI = 19;   // GP19

// Separate chip select lines
const uint8_t CS1 = 17;        // Sensor 1
const uint8_t CS2 = 20;        // Sensor 2


// ADXL345 REGISTERS
const uint8_t REG_DEVID       = 0x00;
const uint8_t REG_BW_RATE     = 0x2C;
const uint8_t REG_POWER_CTL   = 0x2D;
const uint8_t REG_DATA_FORMAT = 0x31;
const uint8_t REG_DATAX0      = 0x32;


// TIMING
const uint32_t SAMPLE_PERIOD_US = 1000000UL / TARGET_ODR_HZ;
uint32_t lastSampleUs = 0;


// SPI SETTINGS (ADXL345 uses CPOL=1, CPHA=1)
SPISettings adxlSPI(SPI_CLOCK_HZ, MSBFIRST, SPI_MODE3);

```

```
// ROBUST BINARY FRAME NOTES:
// sync = 0xC3D2E1F0
// t_us = timestamp in microseconds
// seq = frame counter
// s1x..s2z = raw int16 sensor values
// checksum = sum of all bytes before checksum, module 65536
struct __attribute__((packed)) Frame {
  uint32_t sync;
  uint32_t t_us;
  uint16_t seq;
  int16_t s1x, s1y, s1z;
  int16_t s2x, s2y, s2z;
  uint16_t checksum;
};

Frame frame;
uint16_t seqCounter = 0;

// FUNCTIONS
void selectSensor(uint8_t csPin) {
  digitalWrite(csPin, LOW);
}

void deselectSensor(uint8_t csPin) {
  digitalWrite(csPin, HIGH);
}

void writeRegister(uint8_t csPin, uint8_t reg, uint8_t value) {
  uint8_t command = reg & 0x3F;

  SPI.beginTransaction(adxlSPI);
  selectSensor(csPin);
  SPI.transfer(command);
  SPI.transfer(value);
  deselectSensor(csPin);
  SPI.endTransaction();
}

void readRegisters(uint8_t csPin, uint8_t startReg, uint8_t* buffer, uint8_t count) {
  uint8_t command = 0x80 | (startReg & 0x3F);
  if (count > 1) {
    command |= 0x40;
  }

  SPI.beginTransaction(adxlSPI);
  selectSensor(csPin);
  SPI.transfer(command);

  for (uint8_t i = 0; i < count; i++) {
    buffer[i] = SPI.transfer(0x00);
  }

  deselectSensor(csPin);
  SPI.endTransaction();
}

int16_t combineBytes(uint8_t lowByte, uint8_t highByte) {
  return (int16_t)((highByte << 8) | lowByte);
}

bool initSensor(uint8_t csPin) {
  uint8_t devid = 0;
  readRegisters(csPin, REG_DEVID, &devid, 1);

  // Full resolution +/- 2 g, 4-wire SPI
  writeRegister(csPin, REG_DATA_FORMAT, DATA_FORMAT_VALUE);

  // Output data rate
  writeRegister(csPin, REG_BW_RATE, BW_RATE_CODE);

  // Measurement mode
  writeRegister(csPin, REG_POWER_CTL, 0x08);

  delay(2);
  return true;
}

void readXYZ(uint8_t csPin, int16_t &x, int16_t &y, int16_t &z) {
  uint8_t raw[6];
  readRegisters(csPin, REG_DATAX0, raw, 6);

  x = combineBytes(raw[0], raw[1]);
  y = combineBytes(raw[2], raw[3]);
  z = combineBytes(raw[4], raw[5]);
```

```
}

uint16_t computeChecksum(const uint8_t* data, size_t len) {
  uint32_t sum = 0;
  for (size_t i = 0; i < len; i++) {
    sum += data[i];
  }
  return (uint16_t)(sum & 0xFFFF);
}


// SETUP
void setup() {
  // Start USB CDC serial
  Serial.begin(115200);
  delay(2000);

  SPI.setRX(PIN_MISO);
  SPI.setSCK(PIN_SCK);
  SPI.setTX(PIN_MOSI);
  SPI.begin();

  pinMode(CS1, OUTPUT);
  pinMode(CS2, OUTPUT);

  deselectSensor(CS1);
  deselectSensor(CS2);

  bool ok1 = initSensor(CS1);
  bool ok2 = initSensor(CS2);


  // If init fails, halt
  if (!ok1 || !ok2) {
    Serial.print("Failed");
    while (1) {}
  }
}


// LOOP
void loop() {
  uint32_t nowUs = micros();

  if (nowUs - lastSampleUs < SAMPLE_PERIOD_US) {
    return;
  }
  lastSampleUs = nowUs;

  int16_t s1x, s1y, s1z;
  int16_t s2x, s2y, s2z;

  readXYZ(CS1, s1x, s1y, s1z);
  readXYZ(CS2, s2x, s2y, s2z);

  frame.sync = 0xC3D2E1F0;
  frame.t_us = nowUs;
  frame.seq  = seqCounter++;

  frame.s1x = s1x;
  frame.s1y = s1y;
  frame.s1z = s1z;

  frame.s2x = s2x;
  frame.s2y = s2y;
  frame.s2z = s2z;

  frame.checksum = computeChecksum(
    (uint8_t*)&frame,
    sizeof(frame) - sizeof(frame.checksum)
  );

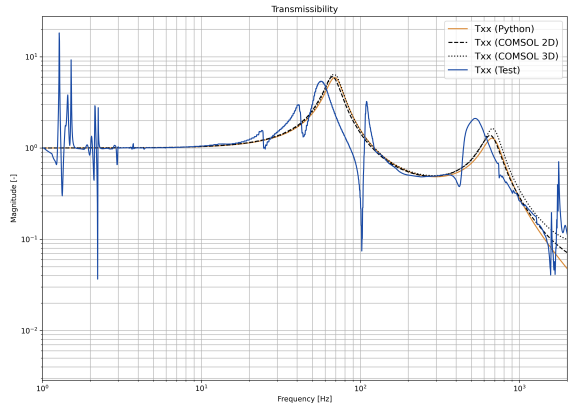
  Serial.write((uint8_t*)&frame, sizeof(frame));
}
```

D

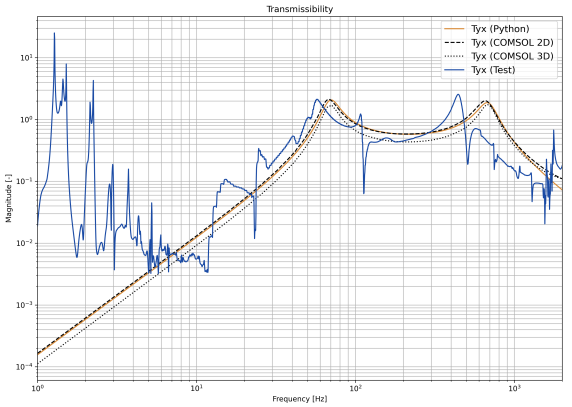
Additional plots

This appendix presents the total frequency response results used to analyze the dynamic behaviour of the tested isolator designs, from $1\ \mathrm{Hz}$ to $2000\ \mathrm{Hz}$. For each case, the direct and cross transmissibilities in the x and y directions are reported together with the corresponding phase and coherence. The transmissibility magnitude is compared between the Python framework, 2D and 3D COMSOL models and the experimental measurements. The phase is compared between the Python framework and the measurements, while coherence is reported only for the experimental data as an indicator of measurement quality and input-output correlation.

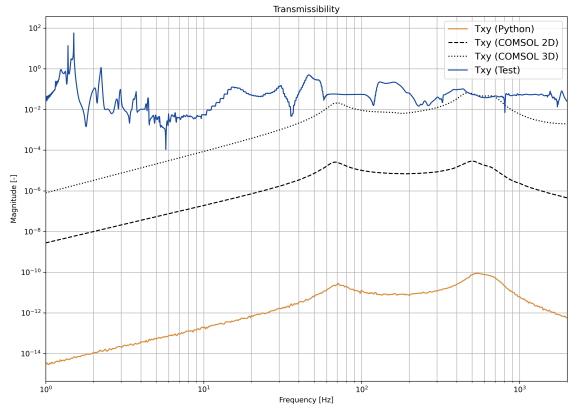
D.1. Base case



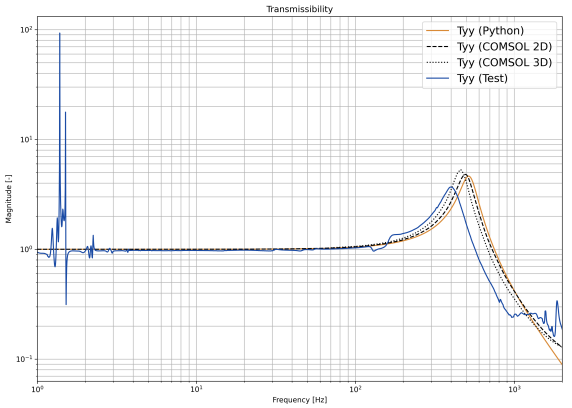
(a) Transmissibility magnitude T_{xx}



(b) Transmissibility magnitude T_{yx}

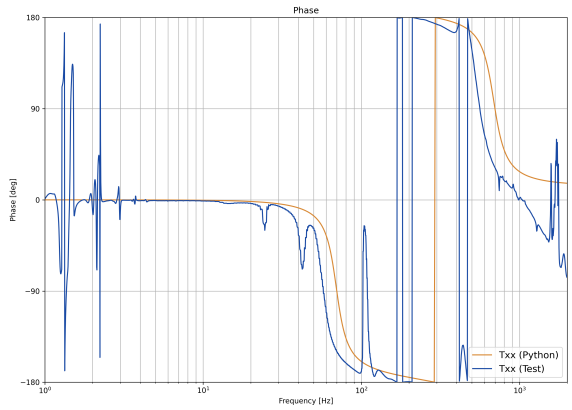


(c) Transmissibility magnitude T_{xy}

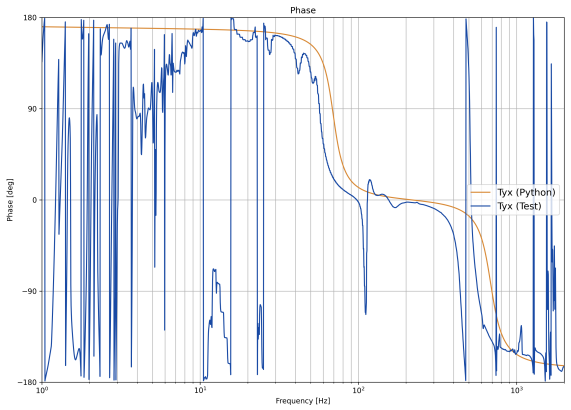


(d) Transmissibility magnitude T_{yy}

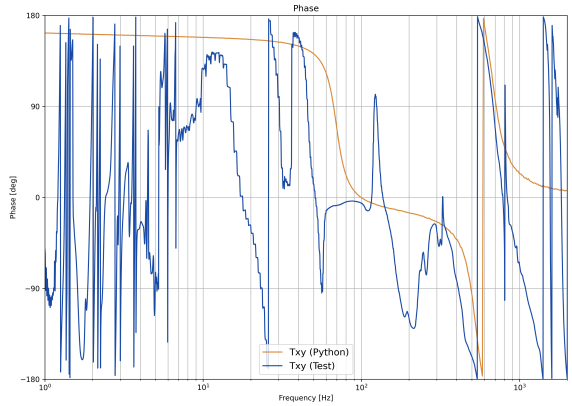
Figure D.1: Direct and cross transmissibility magnitudes for the base case, comparing the Python framework, the 2D and 3D COMSOL models, and the experimental measurements.



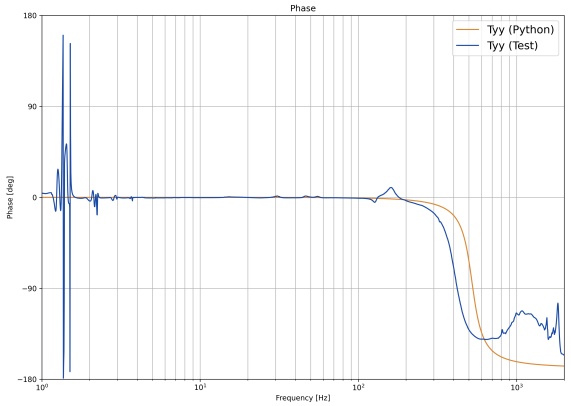
(a) Phase of T_{xx}



(b) Phase of T_{yx}

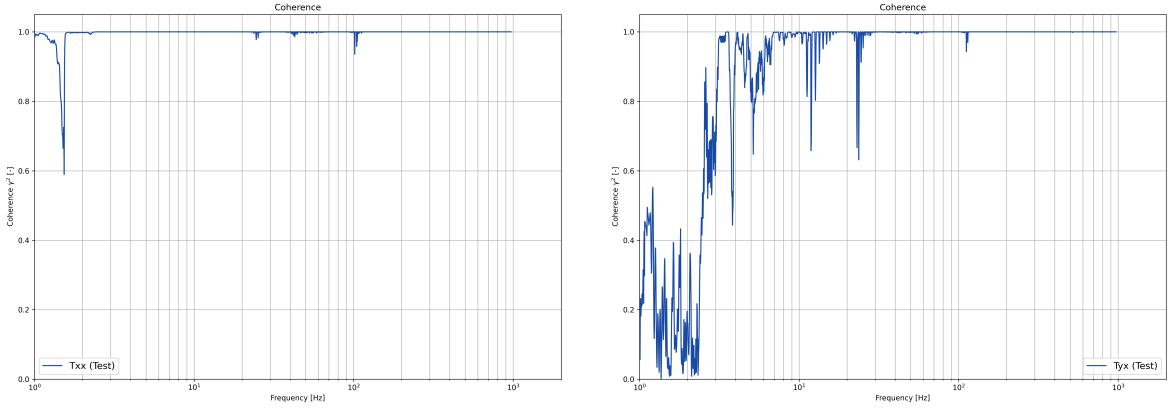


(c) Phase of T_{xy}



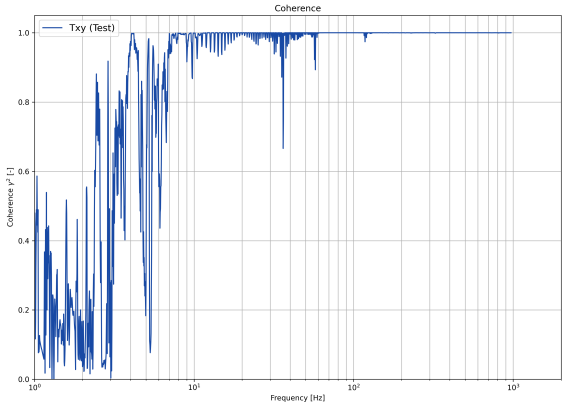
(d) Phase of T_{yy}

Figure D.2: Direct and cross transmissibility phases for the base case, comparing the Python framework with the experimental measurements.

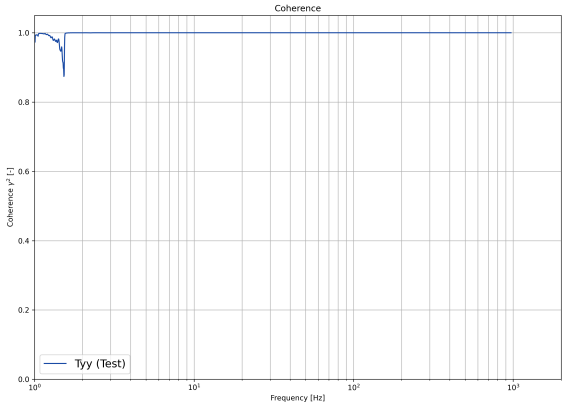


(a) Coherence associated with T_{xx}

(b) Coherence associated with T_{yx}



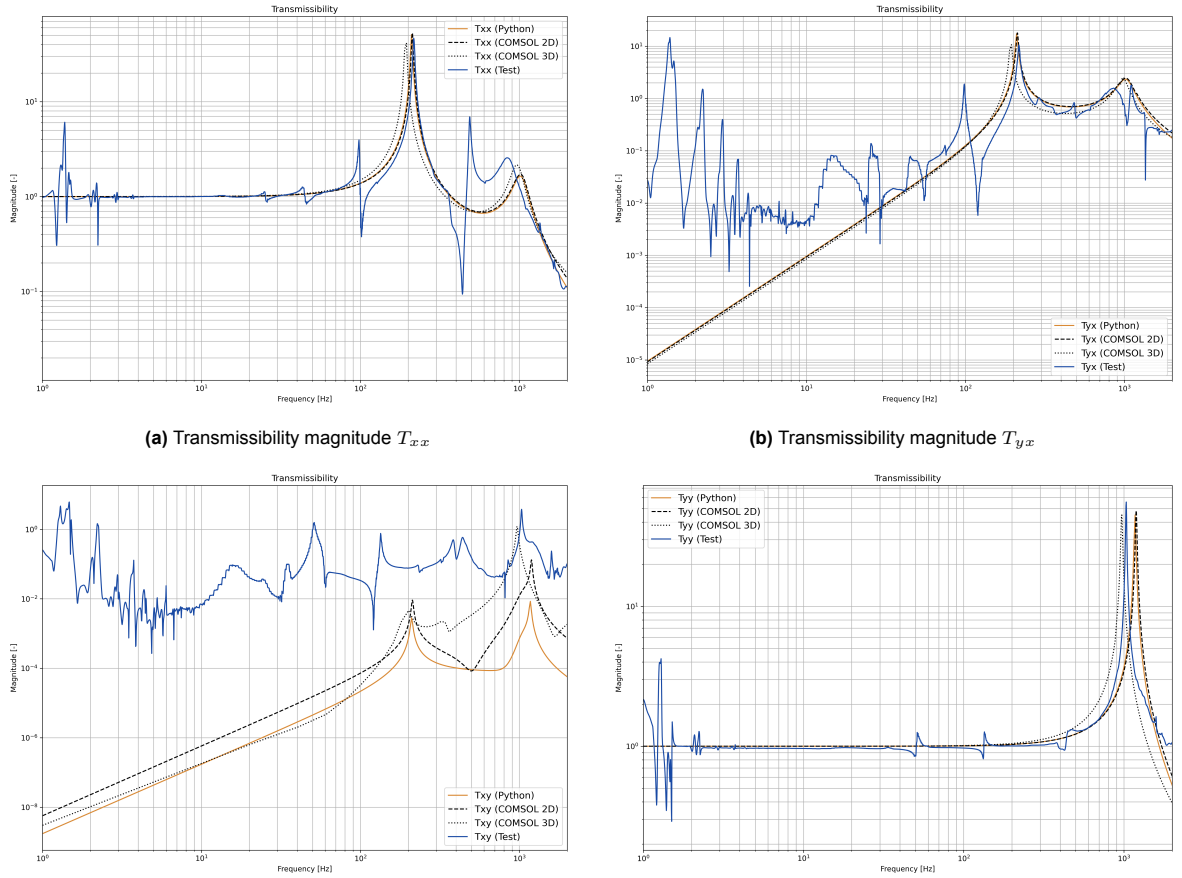
(c) Coherence associated with T_{xy}



(d) Coherence associated with T_{yy}

Figure D.3: Experimental coherence functions associated with the direct and cross transmissibility measurements for the base case.

D.2. x-mode damping



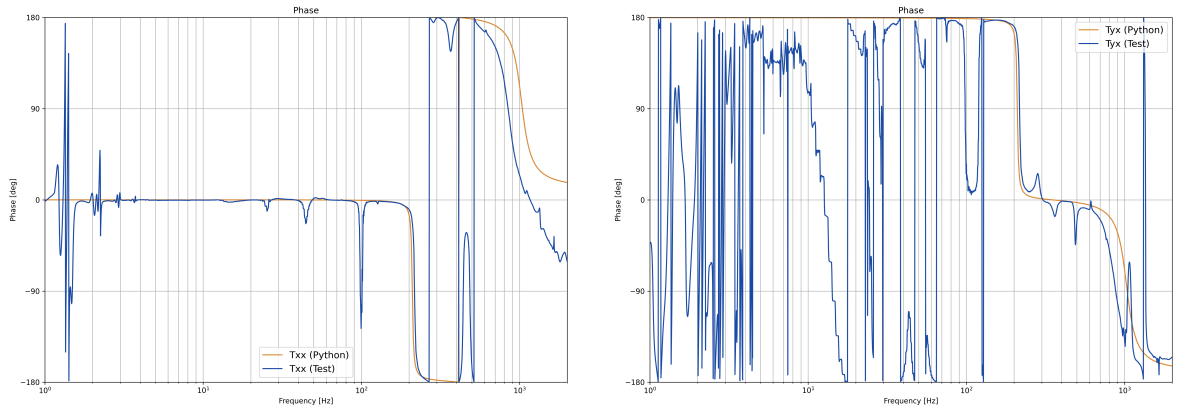
(a) Transmissibility magnitude T_{xx}

(b) Transmissibility magnitude T_{yx}

(c) Transmissibility magnitude T_{xy}

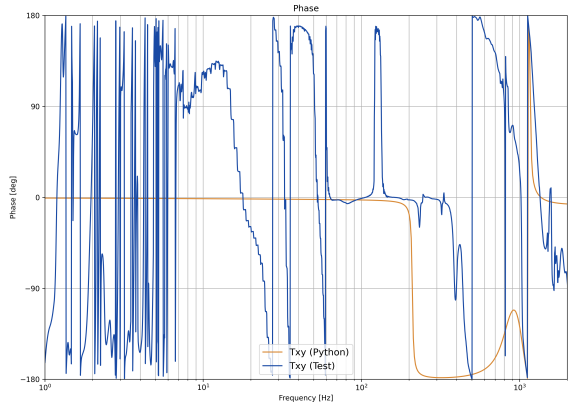
(d) Transmissibility magnitude T_{yy}

Figure D.4: Direct and cross transmissibility magnitudes for the x-mode damped isolator, comparing the Python framework, the 2D and 3D COMSOL models, and the experimental measurements.

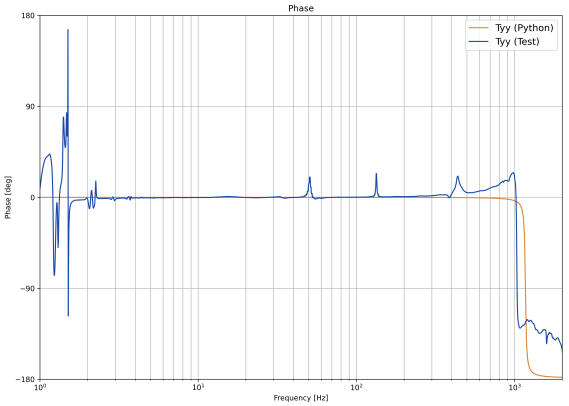


(a) Phase of T_{xx}

(b) Phase of T_{yx}

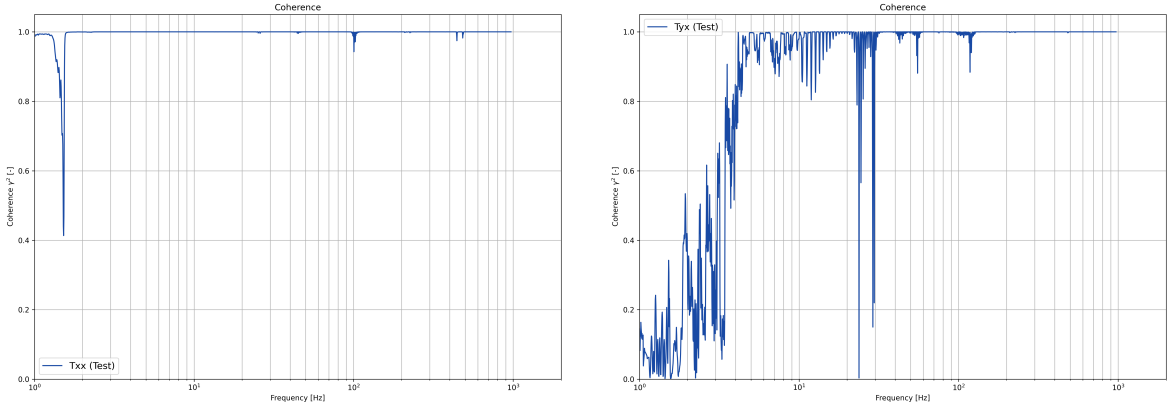


(c) Phase of T_{xy}



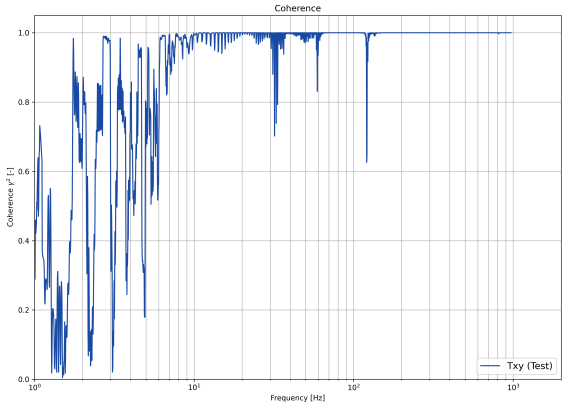
(d) Phase of T_{yy}

Figure D.5: Direct and cross transmissibility phases for x-mode damped isolator, comparing the Python framework with the experimental measurements.

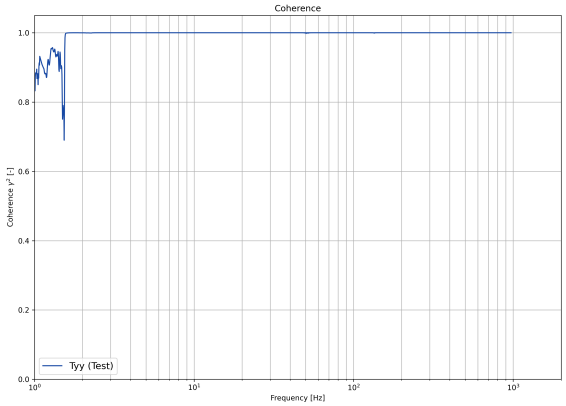


(a) Coherence associated with T_{xx}

(b) Coherence associated with T_{yx}



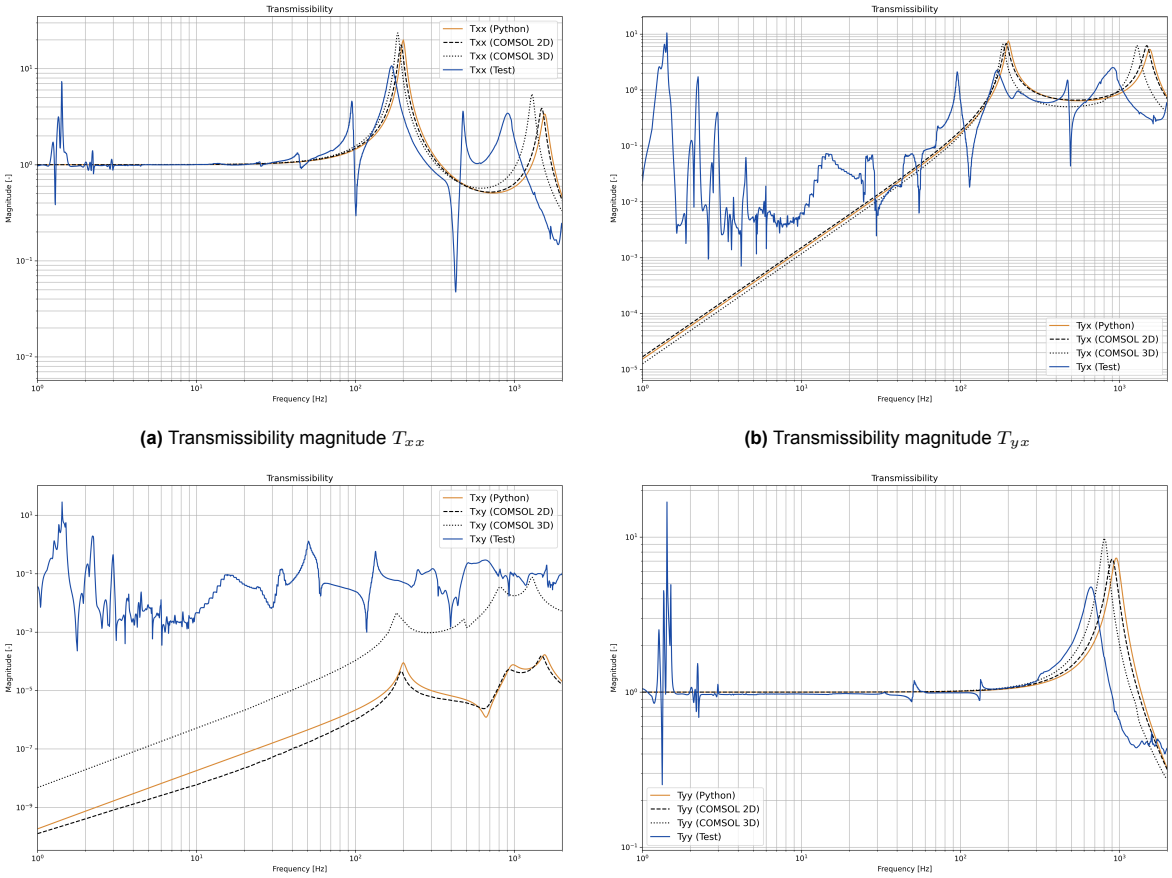
(c) Coherence associated with T_{xy}



(d) Coherence associated with T_{yy}

Figure D.6: Experimental coherence functions associated with the direct and cross transmissibility measurements for the x-mode damped isolator.

D.3. y-mode damping



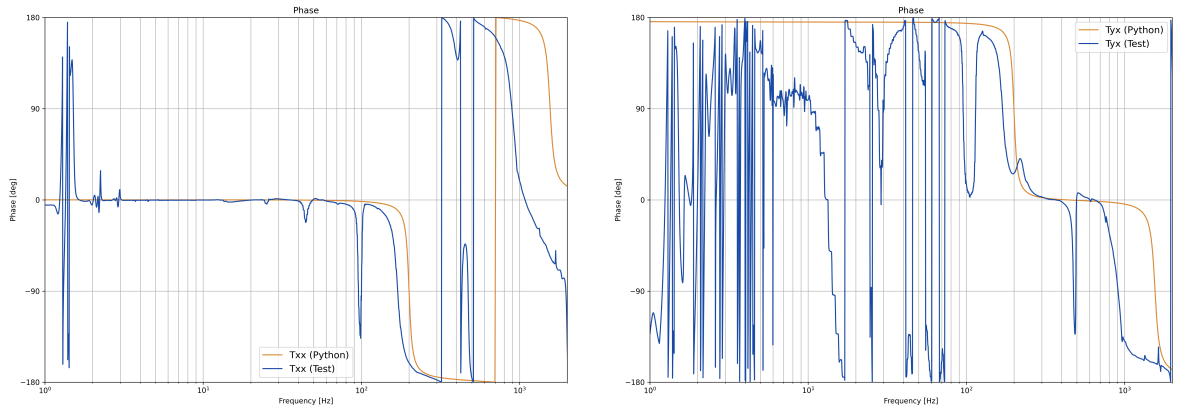
(a) Transmissibility magnitude T_{xx}

(b) Transmissibility magnitude T_{yx}

(c) Transmissibility magnitude T_{xy}

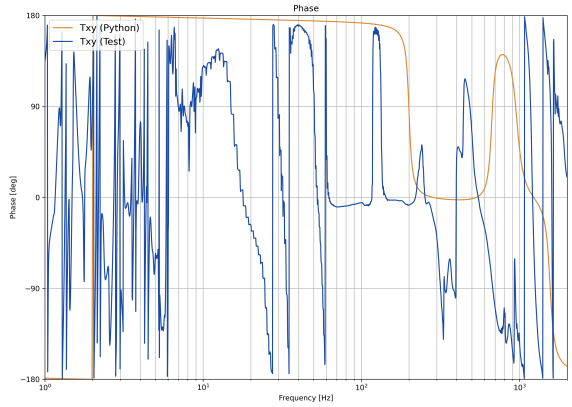
(d) Transmissibility magnitude T_{yy}

Figure D.7: Direct and cross transmissibility magnitudes for the y-mode damped isolator, comparing the Python framework, the 2D and 3D COMSOL models, and the experimental measurements.

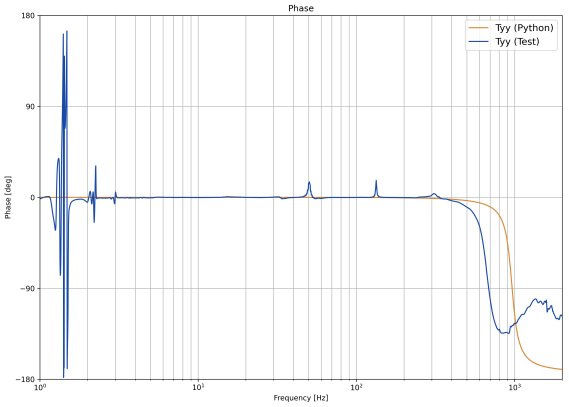


(a) Phase of T_{xx}

(b) Phase of T_{yx}

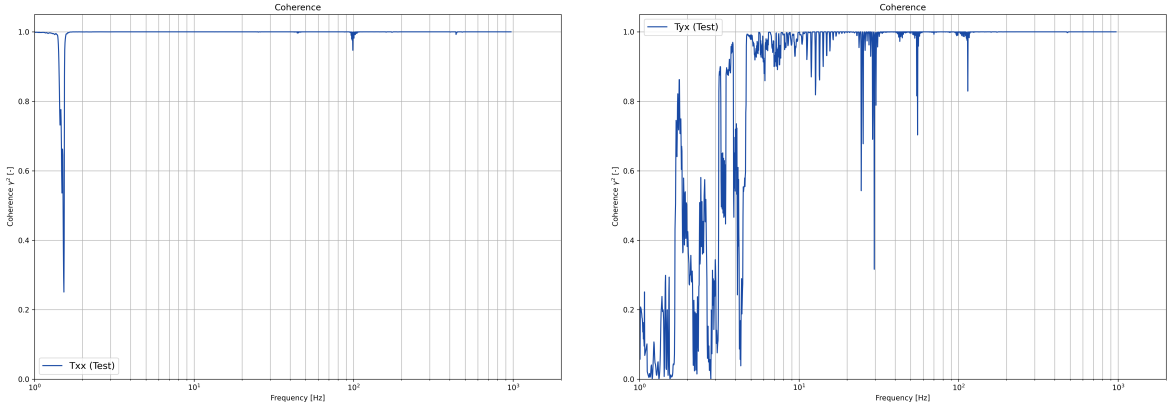


(c) Phase of T_{xy}



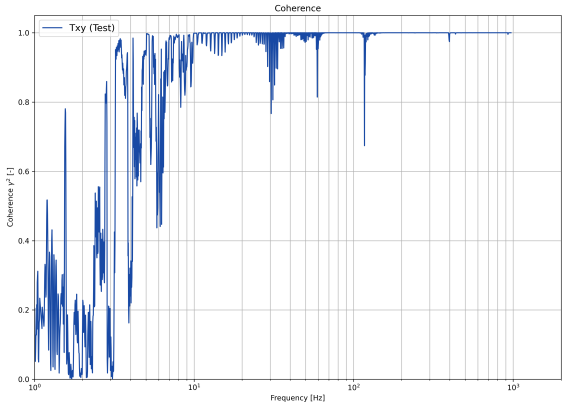
(d) Phase of T_{yy}

Figure D.8: Direct and cross transmissibility phases for y-mode damped isolator, comparing the Python framework with the experimental measurements.

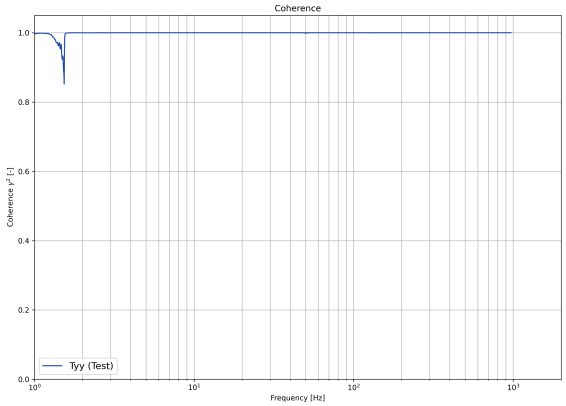


(a) Coherence associated with T_{xx}

(b) Coherence associated with T_{yx}



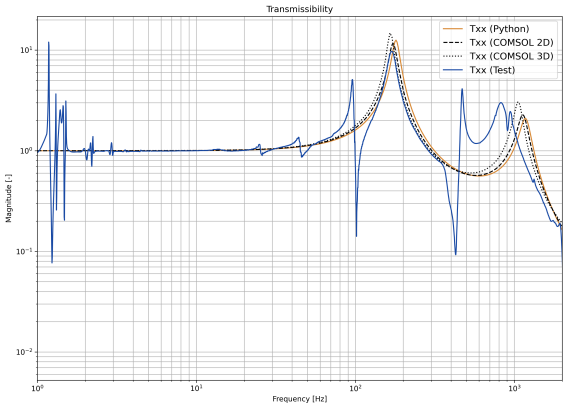
(c) Coherence associated with T_{xy}



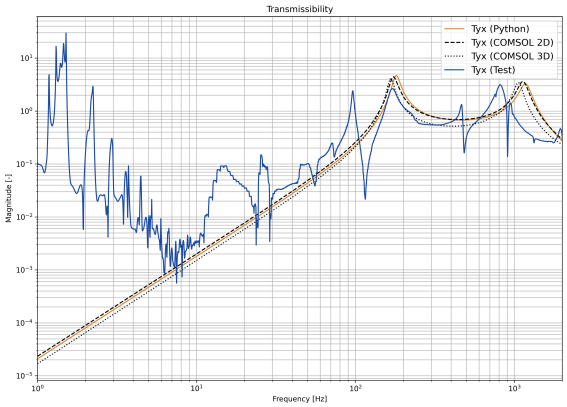
(d) Coherence associated with T_{yy}

Figure D.9: Experimental coherence functions associated with the direct and cross transmissibility measurements for the y-mode damped isolator.

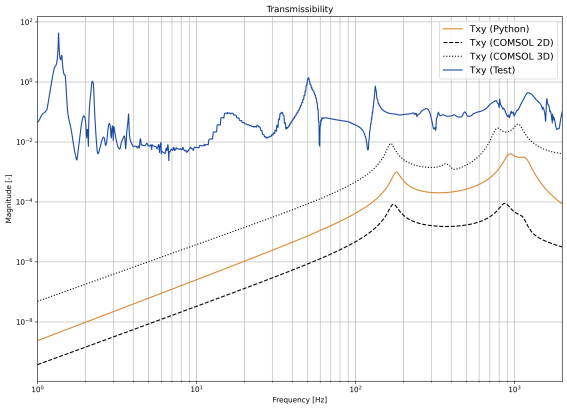
D.4. Multi-mode damping



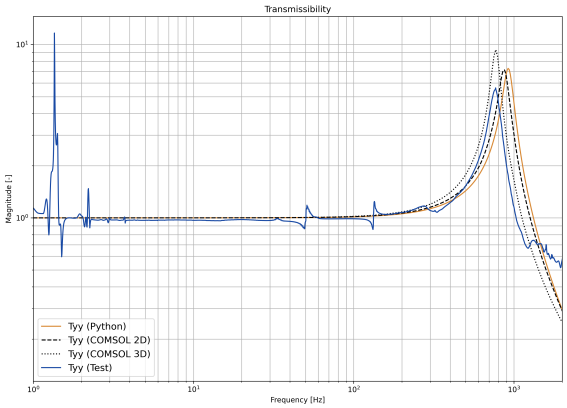
(a) Transmissibility magnitude T_{xx}



(b) Transmissibility magnitude T_{yx}

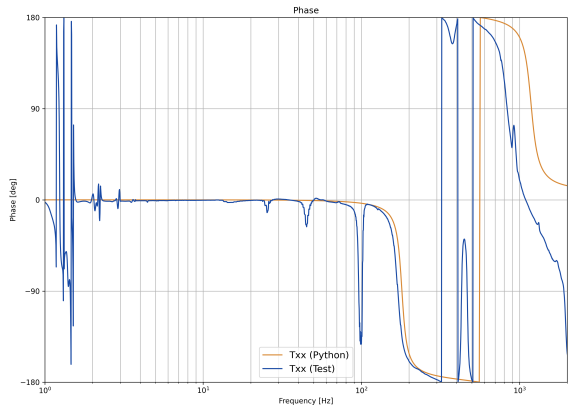


(c) Transmissibility magnitude T_{xy}

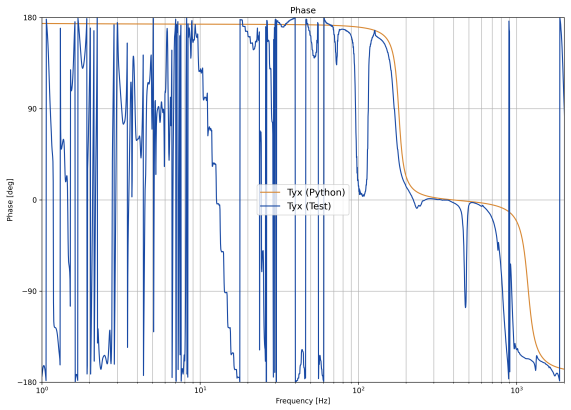


(d) Transmissibility magnitude T_{yy}

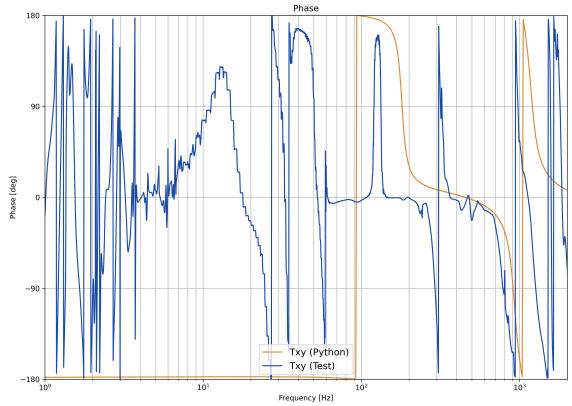
Figure D.10: Direct and cross transmissibility magnitudes for the multi-mode damped isolator, comparing the Python framework, the 2D and 3D COMSOL models, and the experimental measurements.



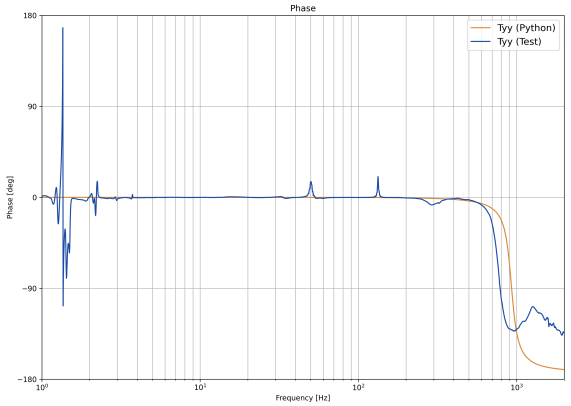
(a) Phase of T_{xx}



(b) Phase of T_{yx}

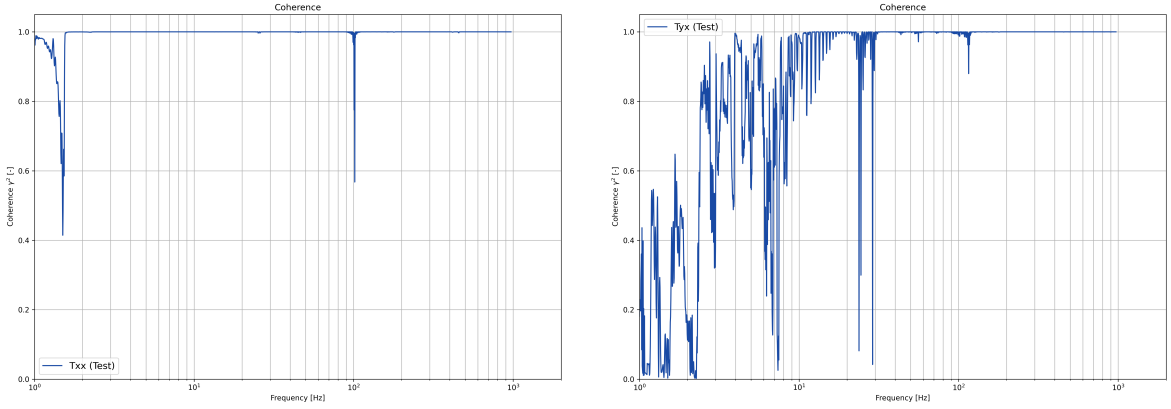


(c) Phase of T_{xy}



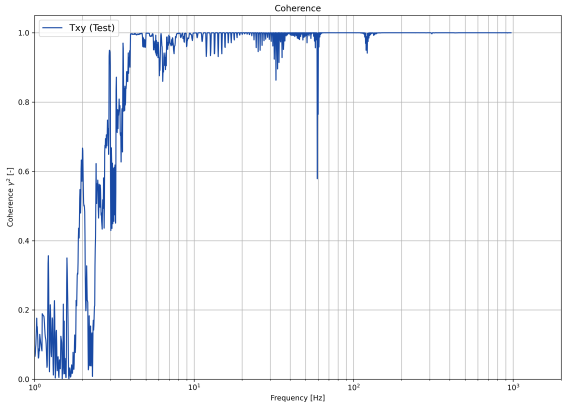
(d) Phase of T_{yy}

Figure D.11: Direct and cross transmissibility phases for multi-mode damped isolator, comparing the Python framework with the experimental measurements.

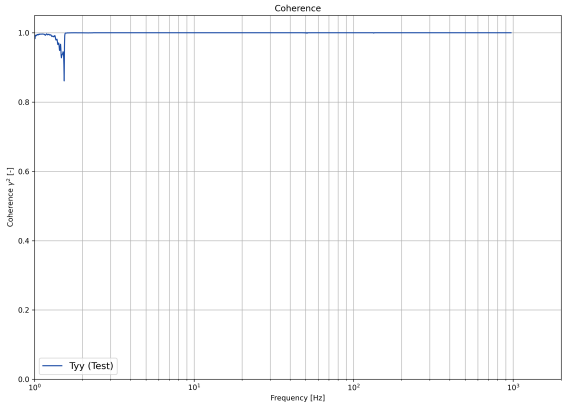


(a) Coherence associated with T_{xx}

(b) Coherence associated with T_{yx}



(c) Coherence associated with T_{xy}



(d) Coherence associated with T_{yy}

Figure D.12: Experimental coherence functions associated with the direct and cross transmissibility measurements for the multi-mode damped isolator.

E

Usage of AI

Generative AI (ChatGPT) was used as supporting tools during this thesis. It was utilized for troubleshooting and debugging Python code for the numerical framework and Python/C++ code used for the data-acquisition (both main and Arduino setups). AI was also used to assist with plotting scripts and figure preparation, and to revise written passages for grammar and clarity. All technical decisions, model formulations, code changes and references were reviewed and verified before inclusion in the thesis.